
Selective growth and characterization of GeSn nanostructures on patterned Si wafers

Von der Fakultät für MINT - Mathematik, Informatik, Physik,
Elektro- und Informationstechnik
der Brandenburgischen Technischen Universität Cottbus-Senftenberg
genehmigte Dissertation zur Erlangung des akademischen Grades einer

Doktorin der Naturwissenschaften

(Dr. rer. nat.)

vorgelegt von

Viktoria Diana Schlykow

geboren am 20.03.1988 in Leipzig

Vorsitzender: Prof. Dr. Götz Seibold

Gutachterin: Prof. Dr. Inga A. Fischer

Gutachter: Prof. Dr. Christian Wenger

Gutachter: Prof. Dr. Thomas Schroeder

Tag der mündlichen Prüfung: 11.06.2019

"Die Dinge sind nie so, wie sie sind.
Sie sind immer das, was man aus ihnen macht."
–Jean Anouilh

Acknowledgment

A lot of people accompanied me on my way to my doctoral thesis. Now is time to express my gratitude towards all of you.

First of all I like to thank the three referees Prof. Dr. Inga A. Fischer, Prof Dr. Christian Wenger and Prof. Dr. Thomas Schroeder.

Inga, thank you for being my first referee and my supervisor during my final stage of my thesis., our discussions about all the new challenges related to photodetection and the support during the measurements in Stuttgart.

Thank you to Christian, who agreed to be a referee of my PhD thesis on short notice. Thank you for your support at IHP.

I am grateful to you, Thomas, for offering to be my third referee and giving me the chance to pursue my PhD thesis at IHP. I am grateful for the time you spent teaching me, discussing with me and most importantly, sharing your scientific knowledge with me. Thank you for being my doctor "father". Furthermore, I had the luck to have two experienced supervisor at my side who supported me in my practical work and introduced me to a new technique like MBE growth: Dr. Noriyuki Taoka and Prof. Dr. Gang Niu. I like to thank you Nori for introducing me to a vast number of new topics. Thanks to your patience and your widespread knowledge, Nori, we managed to perform together numerous growth experiments and carefully evaluated the results.

I am also grateful to Gang Niu who shared his his knowledge about Ge growth at high temperatures with me. Thank you, Gang, for your scientific support. I like to thank Prof. Dr. Giovanni Capellini and Dr. Wolfgang Matthias Klesse for their support on GeSn research at the finishing line of my PhD.

Special thanks belong to Hans Thieme who helped me handling the MBE equipment. Hans, thank you for your support in all questions concerning the technical understanding of so many different tools, I felt very comfortable working in the MBE lab with you.

There are also a lot of people involved in the process of this thesis who fabricated my substrates, namely Dr. Oliver Skibitzki and Dr. Yuji Yamamoto and the clean room staff. I like to thank Beate Kuck, Dr. Michael Andreas Schubert and Hans Michael Krause, David Stolarek for TEM and SEM measurements as well as useful discussions.

I am thankful to Yvonne Heier who helped me with organizational issues and who always had an open ear for my concerns.

I am very thankful to my daily and very punctual coffee break group, consisting of Dr. Peter Zaumseil, Dr. Gunther Lippert, and Dr. Gerhard Fischer. You will have my never ending gratitude for respecting me as a scientist and the person I am.

I was surrounded by experts and I like to thank all group members for sharing their knowledge with me and supporting me and my work.

I am also grateful to my old and new friends who endured and motivated me during the time of performing and writing my thesis. Just to name some, thank you to Sandra, Paula, Johanna, Anne, Sebastian, Henriette, Honey, Ali, Jördis, Peggy and Thomas, Costanza, Fatima, Rene and Anne.

Last but not least I like to express my deep gratitude for the support of my family, especially my sister Veronika and my parents Ljudmila and Juri. Thank you for your never ending support, motivation, inspiration and unconditional love.

Abstract

Over the past seven decades Si microelectronics have developed rapidly. The success of the growing microelectronic industry is also caused by the expansion of materials in addition to Si, enabling the formation of high mobility transistor channels in nm-scaled devices as well as new functionalities such as lasing and detection.

Open challenges are the monolithic integration of group IV devices on Si photonics as well as overcoming the size mismatch between electronic parts in the nm range and photonic parts in the μm scale. In this thesis the future application of GeSn nanostructures on Si wafers as a photodetector is evaluated. The key element required for high performance optoelectronic devices is the formation of high-quality GeSn nanostructures, i.e. overcoming growth challenges such as the introduction of defects due to lattice and thermal mismatch between GeSn and Si substrates as well as suppression of Sn precipitation caused by the limited solid solubility of Sn in Ge.

To achieve high-quality nano-islands, the selective growth of GeSn nanostructures on Si(001) seeds via molecular beam epitaxy is investigated, exploiting the advantages of nanoheteroepitaxy, i.e. growth on nano-patterned substrates. The best compromise between the selective growth of GeSn on Si nano-pillars at significant higher growth temperature than the eutectic temperature of GeSn and the incorporation of Sn into the Ge lattice was achieved at 600° C. X-ray diffraction studies confirmed the substitutional incorporation of 1.4 at. % Sn into the nano-islands avoiding considerable Si interdiffusion from the substrate. Transmission electron microscopy images have shown that dislocations and stacking faults caused by plastic relaxation

of the GeSn nanostructures are located near the island/substrate interface and thus, dislocation-free GeSn nano-islands can be formed, due to gliding out of the threading arms triggered by the nanoheteroepitaxy approach. The high crystal quality of the GeSn nano-dots, enables the investigation of the bandgap by μ -photoluminescence analyses, demonstrating the shrinkage of the direct bandgap with increasing Sn content in the quasi-direct semiconductor.

All islands however feature a β -Sn droplet on their nano-facets. To suppress the out-diffusion of Sn and hence increase the Sn concentration of the GeSn alloy, the GeSn nano-dots were overgrown with a thin Ge cap layer. The Ge cap successfully hinders the formation of Sn segregates on top of the GeSn nano-dots. In fact, capping at 600 °C and 650 °C results in an enrichment of Sn at the surface, forming a GeSn *crust* with 8 ± 0.5 at.% Sn. This wetting layer both enhances the optoelectronic properties of the island *core* and exhibits a relatively strong photoluminescence emission attributed to direct radiative recombination.

Finally, a first demonstration of a GeSn nanostructure based photodetector was successful, due to the utilization of Al nano-antennas exhibiting an enhanced light coupling into the GeSn nanostructures at a wavelength of 700 nm. The responsible mechanism is the local plasmonic field enhancement of the incoming light. The manipulation of the resonance wavelength into the telecommunication regime, i.e. > 1550 nm, have to be investigated in future studies.

The findings of this thesis point out the possibility of the formation of high crystal quality GeSn nano-islands using the nanoheteroepitaxy approach. The bandgap of the GeSn dots can be tuned by varying the Sn concentration. Furthermore, promising results are obtained for utilization of GeSn nanostructures equipped with Al nano-antennas in future optoelectronic devices.

Zusammenfassung

In den letzten sieben Jahrzehnten hat sich die Si-basierte Mikroelektronik-Industrie enorm weiterentwickelt. Der Erfolg dieser wachsenden Industrie ist unter anderem darauf zurückzuführen, dass neben Si weitere Materialien verwendet werden, sodass beispielsweise Transistorkanäle mit hoher Ladungsträgermobilität in nm großen Bauteilen sowie neue Funktionalitäten wie Laseremission und Photodetektion realisiert werden können.

Offene Fragestellungen sind die monolithische Integration von Gruppe-IV-basierten Bauteilen auf Si-Photonischen Chips sowie die Dimensionsdiskrepanz zwischen elektronischen und photonischen Bauteilen. Im Rahmen dieser Doktorarbeit soll untersucht werden, ob GeSn-Nanostrukturen gewachsen auf Si Wafern für die Verwendung als Photodetektor geeignet sind. Der wesentliche Aspekt zur Realisierung von optoelektronischen Hochleistungsbauteilen ist das Wachstum von GeSn-Nanostrukturen mit hoher Kristallqualität, d.h. Wachstumsherausforderungen wie die Einbringung von Defekten aufgrund von Gitter- und thermischer Fehlanpassung zwischen den GeSn-Inseln und dem Si-Substrat sowie Sn-Segregation aufgrund der geringen Löslichkeit von Sn in Ge müssen überwunden werden.

Hierzu wird das selektive Wachstum von GeSn-Nanostrukturen mithilfe von Molekularstrahlepitaxie unter der Verwendung des Nanoheteroepitaxie Ansatzes, d.h. das Wachstum auf nano-strukturierten Substraten, untersucht. Der beste Kompromiss zwischen selektivem Wachstum von GeSn auf nanostrukturierten Si(001)-Wafern und dem Einbau von Sn in das Ge-Gitter wurde bei einer Wachstumstemperatur von 600° C erreicht, was bei weitem die eutektische Temperatur von GeSn überschreitet. Analysen mithilfe

von Röntgendiffraktometrie ergaben einen substitutionellen Einbau von 1.4 at.% Sn in die Nano-Inseln ohne erhebliche Si-Interdiffusion aus dem Si Substrat. Aufnahmen mithilfe von Transmissionselektronenmikroskopie zeigten, dass sich Versetzungen und Stapelfehler aufgrund der plastischen Relaxation der GeSn-Nanostrukturen an der Insel/Substrat-Grenzfläche befinden, da ein Herausgleiten der Versetzungsarmen durch den Ansatz der Nanoheteroepitaxie ermöglicht wird. Dadurch konnten versetzungsfreie GeSn-Nano-Inseln gewachsen werden. Die hohe Kristallqualität ermöglicht es, die Bandlücke mithilfe von Photolumineszenz Spektroskopie zu charakterisieren. Dabei konnte festgestellt werden, dass es zu einer Verringerung der direkten Bandlücke $\Gamma_C - \Gamma_V$ mit steigendem Sn-Gehalt im quasi-direkten Halbleiter kommt.

Allerdings weisen alle Inseln β -Sn-Tropfen auf ihren Nano-Fazetten auf. Um die Diffusion des überschüssigen Sn zu vermeiden und so den Sn-Gehalt in der GeSn-Legierung zu erhöhen, wurden die GeSn-Nano-Kugeln im Nachhinein mit einer dünnen Ge-Deckschicht überwachsen. Diese Ge-Deckschicht verhindert erfolgreich die Bildung von β -Sn-Segregaten auf den GeSn-Nano-Kugeln. Tatsächlich führt das Verschließen der Inseln bei 600 °C und 650 °C dazu, dass sich Sn an der Oberfläche anreichert und sich eine GeSn-Kruste mit 8 ± 0.5 at.% Sn bildet. Diese Benetzungsschicht verbessert die optoelektronischen Eigenschaften des *Inselkerns* und weist gleichzeitig eine relativ starke Photolumineszenz auf, die auf die Strahlungsemission der direkten Bandlücke zurückzuführen ist.

Schließlich war eine erste Demonstration eines Photodetektors basierend auf GeSn-Nanostrukturen durch die Verwendung von Al-Nano-Antennen erfolgreich, um eine verstärkte Lichteinkopplung in die GeSn Nanostrukturen bei einer Wellenlänge von 700 nm zu erreichen. Der zugrundeliegende Mechanismus ist die lokale plasmonische Feldverstärkung des einfallenden Lichtes. Die Manipulation der Resonanzwellenlänge in den Bereich der Telekommunikationswellenlänge, d.h. über 1550 nm, sollte in zukünftigen Studien untersucht werden.

Die Ergebnisse dieser Arbeit zeigen die Möglichkeit zum Wachstum von GeSn-Nano-Inseln mit hoher Kristallqualität unter Verwendung des Nano-

heteroepitaxie-Ansatzes auf. Die Bandlücke der GeSn-Inseln kann durch Variation der Sn-Konzentration manipuliert werden. Darüber hinaus, wurden vielversprechende Ergebnisse für die Nutzung von GeSn-Nanostrukturen mit Al-Nano-Antennen in zukünftigen optoelektronischen Bauelementen erzielt.

Contents

Acknowledgment	I
Abstract	III
Zusammenfassung	V
List of Abbreviation	XI
1 Introduction and Motivation	3
1.1 Trends in Silicon microelectronics	3
1.2 The impact of new materials	5
1.3 Aim and structure of thesis	14
2 Growth theory and experimental set up	17
2.1 Growth theory	17
2.1.1 Atomistic processes at the surface during growth	17
2.1.2 Growth modes	18
2.2 Defect formation	20
2.3 Nanoheteroepitaxy	23
2.3.1 Theory	23
2.3.2 Technical implementation of Nanoheteroepitaxy	27
2.3.3 Atomistic model of selective growth of Ge on Si	29
2.4 Growth techniques	31
2.5 Growth challenges SiGeSn	33
2.6 Wafer and sample preparation	36

3	Characterization techniques	41
3.1	Characterization of morphology	41
3.1.1	Scanning electron microscopy	41
3.1.2	Atomic force microscopy	42
3.2	Characterization of lattice	44
3.2.1	X-ray diffraction	44
3.2.2	Transmission electron microscopy	52
3.3	Optoelectronic characterization methods	55
3.3.1	Photoluminescence	55
3.3.2	Photodetection	62
4	Results and discussion	73
4.1	Selective growth of GeSn nanostructures	73
4.2	Incorporation of Sn	97
4.3	Optimization of GeSn NHE growth	101
4.4	Photodetection	123
5	Conclusion and Outlook	149
	Scientific visibility	153
	Bibliography	169

List of Abbreviation

ADF	Annular Dark-Field imaging
AFM	Atomic Force Microscopy
AOTF	Accoustic Optical Tunable Filter
BEOL	Back-End-Of-Line
BF	Bright Field
BSE	Backscattered Electrons
CCD	Charge Coupled Device
CMOS	Complementary Metal Oxide Semiconductor
CMP	Chemical Mechanical Polishing
CTE	Coefficient of Thermal Expansion
CVD	Chemical Vapor Deposition
DF	Dark Field
DFT	Density Functional Theory
DIW	De-Ionized Water
EDS	Energy Dispersive X-ray Spectroscopy
EDX	Energy Dispersive X-ray Spectroscopy
EELS	Electron Energy-Loss Spectrometry
EsB	Energy selective Backscattered
EXAFS	Extended X-ray Absorption Fine Structure
fcc	face-centered cubic
FEM	Finite Element Method
FEOL	Front-End-Of-Line
FET	Field-Effect Transistor

FIB	Focused Ion Beam
FWHM	Full Width at Half Maximum
Ge	Germanium
HAADF	High–Angle Annular Dark–Field imaging
HEMT	High Electron Mobility Transistors
HET	Hot–Electron Transistor
HRTEM	High–Resolution Electron Microscopy
LMRs	Leaky Mode Resonances
LSPs	Localized Surface Plasmons
MBE	Molecular Beam Epitaxy
MDs	Misfit Dislocations
MOSFET	Metal–Oxide–Semiconductor Field–Effect Transistor
NHE	Nanoheteroepitaxy
NWs	Nano–Wires
PL	Photoluminescence
RF	Radio Frequency
RHEED	Reflection High–Energy Electron diffraction
RSM	Reciprocal Space Map
SBH	Schottky Barrier Height
SE	Secondary Electrons
SEM	Scanning Electron Microscopy
SFs	Stacking Faults
Si	Silicon
SK	Stranski Krastanov

Sn	Tin
SPP-BWs	Surface Plasmon Polariton Bloch Waves
SRH	Shockley–Read–Hall
STEM	Scanning Transmission Electron Microscopy
TDs	Threading Dislocations
TE	Transverse Electric
TEM	Transmission Electron Microscopy
TEOS	Tetraethylorthosilicat
TM	Transverse Magnetic
UHV	Ultra High Vacuum
UV	Ultra Violet
XPS	X–Ray Photoelectron Spectroscopy
XRD	X–Ray Diffraction

1 | Introduction and Motivation

1.1 Trends in Silicon microelectronics

Microelectronics is the technology related to the design, development and construction of electronic systems utilizing extremely small elements. The investigated micro circuits contain different components such as transistors, capacitors, diodes, insulators and much more. The first solid transistor based on Germanium (Ge) was discovered and developed in the Bell Telephone Laboratory by William Shockley, John Bardeen and Walter Brattain in 1947. In 1963, Frank Wanlass proposed at Fairchild Semiconductor the idea of a Complementary Metal Oxide Semiconductor (CMOS) circuit consisting of a pair of p- and n-type Metal–Oxide–Semiconductor Field–Effect Transistor (MOS-FET) to construct a logic circuit with low power consumption and robust noise behavior. Soon Silicon (Si) was the transistor material of choice due to its stable native oxide SiO_2 . It was in 1971, when Intel developed the first microprocessor called “Intel 4004“ with 2300 transistors opening the path for a new industry.

Since then Si microelectronics developed into a huge business with a market size of 412 Billion US Dollar (2017) having a great impact on our society [1]. To give an example, in a German household young people between 12 and 19 years old are using a smartphone (99 %), a computer (98 %), a digital camera (85 %), MP3 player/iPOD (66 %), a TV with web access (52 %) and much more [2].

Already in 1965, Gordon Moore, co-founder of Intel and Fairchild Semicon-

ductors, predicted the development of the semiconductor industry and the Si technology called Moore's law. According to Moore's law, the number of transistors on a chip doubles every 1.5 to 2 years [3]. Fig. 1.1 illustrates the cycle of transistor scaling.

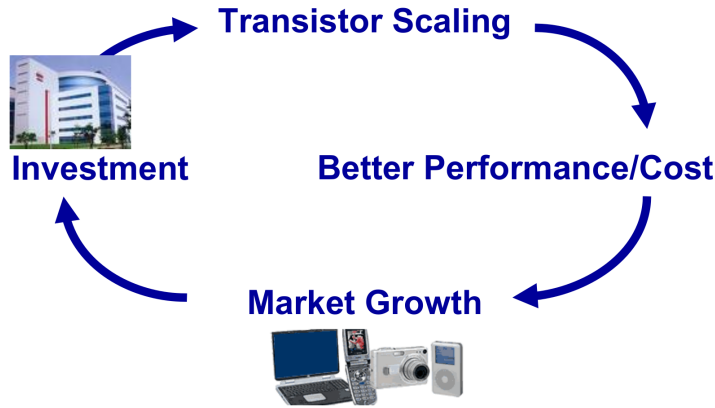


Figure 1.1: Cycle of transistor scaling and growth of semiconductor industry [4].

Transistor scaling results in a better performance-to-cost ratio, thus sales are increasing and the semiconductor market grows. Hence more money for further investments in the development of new technologies is available, which results in enhanced scaling and the cycle starts again [4]. New technologies like Ultra Violet (UV) lithography enables scaling of the gate length down to 15 nm and fin structures below 10 nm.

However, physical limits will be reached and further scaling will not be sufficient enough addressing all performance issues. As an example, scaling the gate dielectric used for a long time, SiO_2 , below 3 nm results in performance losses caused by leakage current due to quantum mechanic tunneling mechanism or by the breakdown of the ultra thin SiO_2 layer due to defects generated by high stress voltage during operation of MOSFETs [5]. Furthermore, today's industry requires not only an increase in performance but also an increase in functionality such as lasing or photodetection used for optoelectronics.

To maintain and expand Moore's law, the International Technology Roadmap for Semiconductors (ITRS) has been established by specialists in Europe,

Japan, Korea, Taiwan and USA, establishing two main approaches [6]:

- The “More Moore“ trend describes further device scaling with transistor technology boosters such as strained channel, high mobility materials, high k-materials, sufficient metal gate and new transistor architectures such as three dimensional structures for improved performance in CMOS technology.
- In the “More than Moore“ approach additional functionalities are studied such as lasing, detection or sensing. These new features can be used to develop “lab on chip“ systems e.g. analyzing blood samples in a portable device.

Due to intrinsic limitations of Si, the addition of new materials seems unavoidable to further increase the market volume of the microelectronic industry.

1.2 The impact of new materials

Various materials are promising candidates for the replacement of Si as an active material in the “More Moore“ or “More than Moore“ approach.

III–V materials exhibit high electron mobility enabling the development of high power and frequency devices such as High Electron Mobility Transistors (HEMT) following the “More Moore“ approach [7]. Moreover, III–V materials such as InGaAs or InP are direct bandgap semiconductors and thus, benefit from the high and efficient radiative recombination making them excellent candidates for realization of optoelectronic devices such as lasers (“More than Moore“) [8]. These materials have however the disadvantage of non-monolithic integration into the Si technology platform, i.e. III–V growth and processing is not integrated into the Si microelectronic fabrication: Additional process steps like wafer bonding have to be established to integrate III–V materials on Si chips requiring high process costs.

2D materials like graphene benefit from their unique intrinsic properties.

Due to high conductivity, graphene is well suited for a base material in a Hot–Electron Transistor (HET) for Tera-Hertz Radio Frequency (RF) applications [9]. Despite the promising properties, mass production of graphene based devices has not been established until now, due to the difficulties of large scale fabrication of graphene.

Group IV elements such as Ge and Sn are another interesting choice of material due to the potential of monolithical and CMOS compatible integration in Si technology.

Benefits of the SiGeSn system

Before considering the advantages of the SiGeSn material system in the More Moore as well as More than Moore trend, the most important properties of group IV alloy will be introduced.

SiGeSn lattice

Sn exists in two crystalline phases (1) semiconductor α -Sn (diamond structure) and (2) metal β -Sn (tetragonal structure). Below 13.2 °C, β -Sn undergoes a transition to α -Sn which means β -Sn is the stable phase at room temperature. The binary systems GeSn and SiSn are eutectic materials with an eutectic temperature T_{ec} of 231.1 °C [10] and 231.9 °C [11], respectively near the melting point of pure Sn (231.9 °C [12]). Furthermore, Sn has a very low equilibrium solubility in pure Ge and Si of about 1 at. % [10] and 0.1 at. % [11], respectively.

In (Si)GeSn alloys the Sn atoms are substitutionally incorporated into the diamond lattice of (Si)Ge. Calculations show that the introduction of atoms with larger covalent radii than Ge like Tin (Sn) results in compressive local strain, while incorporating smaller atoms like Si form tensile local strain. Hence, it is possible to compensate the local strain of Sn atoms by Si suppressing Sn segregation and forming high Sn content SiGeSn alloys. Shimura et al. [13] investigated the atom arrangement of group IV ternary alloys by Extended X–ray Absorption Fine Structure (EXAFS) measure-

ments. A sketch of the calculated atom arrangement is shown in Fig. 1.2.

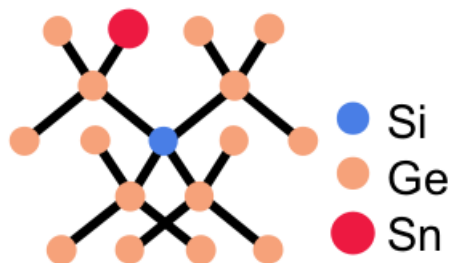


Figure 1.2: Sketch of atom arrangement in a $\text{Si}_y\text{Ge}_{1-y-z}\text{Sn}_z$ alloy. Ge atoms are indicated by orange, Si by blue and Sn by red circles [13].

The evaluation of the EXAFS studies revealed that a Si–Sn bond is unfavorable, probably due to the lower solubility of Sn in Si compared with Ge. Instead Sn atoms tend to be located at the second nearest neighbor position of a Si atom. To give an example for the strain compensation, the incorporation of 9 at.% Sn into Ge in a binary alloy causes a compressive in-plane strain of -1.35 %, while the formation of a ternary alloy with about 6 at.% Si and an increased Sn concentration of about 10 at.% exhibits a lower in-plane strain of about -1.28 %. However, to gain thermal stability up to a temperature of 600 °C without the formation of β -Sn segregates, requires a high Si to Sn ratio, i.e. the introduction of ≈ 33 at.% Si and ≈ 7 at.% Sn into the Ge lattice is necessary, which results in a total in-plane tensile strain of about 0.19 %.

Band diagram

Fig. 1.3 shows the calculated band gap of Si, Ge and α -Sn at 0 K. In case of Si and Ge the maximum of valence band and the minimum of the conduction band are not located at the same wave vector and thus, both are indirect bandgap semiconductors, whereas in case of α -Sn the extrema of the conduction and valence band are aligned at the Γ -point in k -space, typically for direct bandgap material. At the Γ -point Si exhibit a band gap of 3.3 eV and Ge of 0.89 eV, respectively, while α -Sn exhibit a zero band gap of ≈ -0.4 eV, i.e. the extrema of the conduction and valence band are overlapping at the Γ -point. Although Ge is an indirect band gap mate-

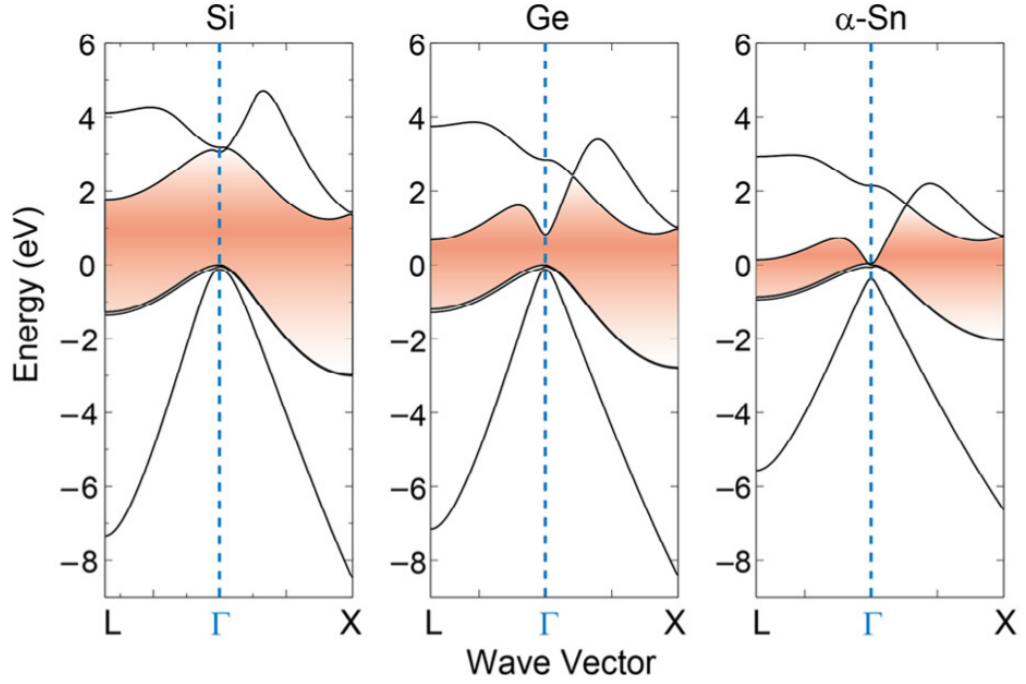


Figure 1.3: Calculated bandstructure of Si and Ge α -Sn at 0 K [14]. All three semiconductors exhibit a diamond lattice. Ge and Si are indirect bandgap materials, while α -Sn exhibit a direct bandgap.

rial, the difference in Γ - and L-valley is only 140 meV compared to Si with $\Delta E_X^\Gamma = 2.3$ eV. Overcoming the small offset between Γ - and L-band of Ge is possible by either applying strain decreasing the Γ valley or heavy n-doping increasing the probability of the radiative $\Gamma_C - \Gamma_V$ transition. Another interesting approach to manipulate the bandgap of Ge, is the incorporation of Sn into Ge (see Fig. 1.4). Dutt and co-workers [15] calculated the bandstructure of fully relaxed $\text{Ge}_{1-x}\text{Sn}_x$ alloys at room temperature using the virtual crystal approximation. By the incorporation of Sn both the Γ - and the L-valley are decreased. In fact, the shrinkage of the Γ -valley is larger compared to the L-valley and thus a cross over of Γ - and L-point is expected for the incorporation of ≈ 6.55 at.% Sn. Hence, direct bandgap group IV semiconductors can be achieved by band gap engineering incorporating Sn into Ge. However, the Sn content at the point of cross over of the Γ - and L-point varies a lot in literature. As an example Moontragoon et al. [14] uses

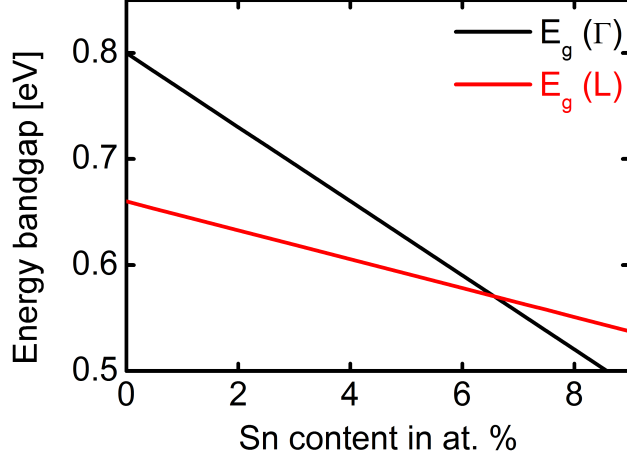


Figure 1.4: Relationship between energy bandgap and Sn content for GeSn alloys at 300 K [15].

an empirical pseudopotential theory and determines the crucial Sn content to be > 17 at.%. The deviation of the Sn concentration for the crossover of the Γ - and L-point (± 10 at.%) is caused by the different values of the so called bowing parameter b which describes the difference of the linear interpolation of the alloy bandstructure. The bandgap energy at the point i (i.e. either at the Γ - or L-point) of an $\text{Ge}_{1-x}\text{Sn}_x$ alloy can be calculated as follows [14]

$$E_i(x) = E_i^{\text{Ge}} \cdot (1 - x) + E_i^{\text{Sn}} \cdot x + b_i^{\text{GeSn}} \cdot x \cdot (1 - x). \quad (1.1)$$

Clearly, by varying b_i a different Sn content at the cross over of the Γ - and L-point is determined.

Even more complicated is the treatment of a ternary alloy $\text{Si}_x\text{Ge}_{1-x-y}\text{Sn}_y$ using Eq. 1.2 [16]

$$\begin{aligned} E_i(x, y) = & E_i^{\text{Ge}} \cdot (1 - x - y) + E_i^{\text{Si}} \cdot x + E_i^{\text{Sn}} \cdot y \\ & + b_i^{\text{SiGe}} \cdot x \cdot (1 - x - y) \\ & + b_i^{\text{GeSn}} \cdot y(1 - x - y) + b_i^{\text{SiSn}} \cdot xy . \end{aligned} \quad (1.2)$$

Similar to the binary alloy, E_i is the bandgap between the valence band and $i = \Gamma, L$ or X - valley of the conduction band. Besides the bowing parameter of GeSn, one has to determine b_i^{SiGe} and b_i^{SiSn} . Similarly, to the approach to determine the bandgap, one can derive the lattice constant a_{SiGeSn} of a ternary alloy $Si_xGe_{1-x-y}Sn_y$ using the corresponding bowing parameter assuming a quadratic expansion of the lattice [16]

$$a_{SiGeSn} = a_{Ge} \cdot (1 - x - y) + a_{Si} \cdot x + a_{Sn} \cdot y + b_{SiGe} \cdot x(1 - x) + b_{SnGe} \cdot y(1 - y). \quad (1.3)$$

One can determine the energy bandgap (Eq. 1.2) as well as the lattice constant (Eq. 1.3), taking into account the lattice parameter for Ge (0.56575 nm), Si (0.54307 nm) and α -Sn (0.64912 nm) as well as the bowing parameters $b_{SiGe} = -0.026$ and $b_{SnGe} = 0.166$, while the bowing for SiSn is assumed to be zero [17]. The results of the lattice parameters and the bandgap for various $Si_xGe_{1-x-y}Sn_y$ alloys are shown in Fig. 1.5. By incorpo-

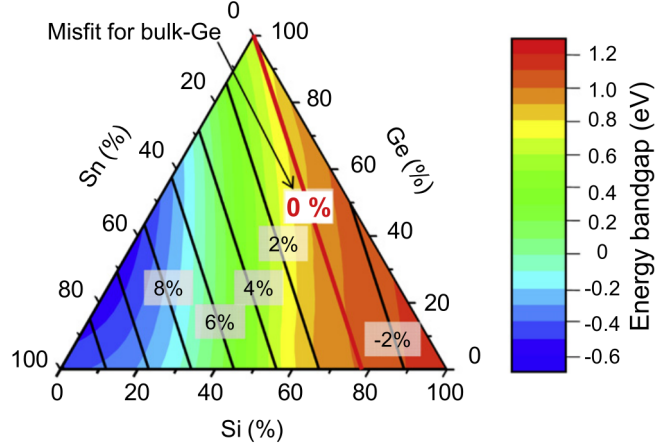


Figure 1.5: Energy bandgap of $Si_xGe_{1-x-y}Sn_y$ ternary alloys with various concentrations of Ge, Si and α -Sn from 0 to 100 at.%. The energy bandgap at the conduction band points Γ -, L - or X - point is plotted in colors. The solid black lines and the values in % represent the lattice match to bulk-Ge [16].

ration of Si one can tune the lattice parameter and gain Ge lattice matched $Si_xGe_{1-x-y}Sn_y$ alloys (red solid line in Fig. 1.5). Due to the lower lattice mismatch compared to the growth of GeSn on Si, an alloy with decreased

defect density can potentially be formed. However, the bandgap increases with increasing Si concentration. Thus, the incorporation of even more Sn is necessary to obtain a direct bandgap material indicated by the colors from dark blue to bright green. Concerning the application as a photodetector, the formation of $\text{Si}_{0.45}\text{Ge}_{0.20}\text{Sn}_{0.35}$ on Ge is addressing the spectral region for telecommunication of the U-band around 1780 nm exhibiting a lattice mismatch of about 4 % similar to the Ge/Si system. However, achieving the bandgap of interest, one has to overcome the low solubility of Sn in Ge (1 at.%) and Si (0.1 at.%).

Carrier mobility of GeSn alloys

The addition of Ge to Si was an immense development, increasing the carrier mobility. In fact, Ge possesses with $1800\text{-}2060 \text{ cm}^2 \text{ V}^{-1}\text{s}^{-1}$ the highest hole mobility compared to the most common semiconductors such as InP, GaAs and many more. Furthermore, the electron mobility of Ge is with $3900 \text{ cm}^2 \text{ V}^{-1}\text{s}^{-1}$ [18] about 2.5 times higher than the value of Si ($1450 \text{ cm}^2 \text{ V}^{-1}\text{s}^{-1}$ [19]). An incorporation of 8 at.% Sn into the Ge lattice further enhances the hole mobility to about $4500 \text{ cm}^2 \text{ V}^{-1}\text{s}^{-1}$ [20], which is beneficial for both electronic and optoelectronic devices. Linked to the bandgap shrinkage due to the incorporation of Sn the population of electrons at the Γ -point is increasing, leading to a reduction of the effective mass. In fact, by increasing the Sn content to > 10 at. %, a maximized electron population is achieved leading to a high directness (i.e. $\Delta E = E_L - E_\Gamma$ is increased) [21].

“More Moore“ approach

The utilization of SiGeSn nanostructures for Field-Effect Transistor (FET)s is an excellent example for the “More Moore“ trend. The enhancement of the carrier mobility can be realized by the incorporation of Sn into the (Si)Ge lattice and the introduction of biaxial strain leading to the reduction of the effective mass [22]. Thus, strained GeSn p-channel transistors can already surpass Ge-based MOSFETs [23], [24]. A further increase of mobility is gained by so called FinFET device architecture with well-controlled strain field. Calcu-

lations by Gupta *et al.* [25] propose GeSn as pMOS material enhancing the hole mobility of compressively strained GeSn which is achieved by both pseudomorphic growth on a SiGeSn buffer layer and formation of fins (patterning of the GeSn layers) and subsequent overgrowth with a GeSn stressor. This kind of device architecture leads to an enhanced operation speed, a reduced leakage current and enables an increase of components per area on chip following the “More Moore” approach.

“More than Moore” approach

Fig. 1.6 focuses on the “More than Moore” trend, where Si photonics is one of the attractive technologies combining electronic and photonic devices such as (i) lasers and (ii) photodetectors on a single chip.

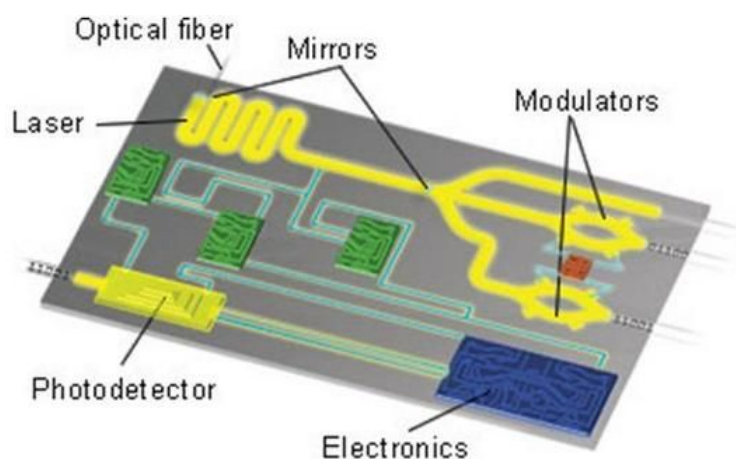


Figure 1.6: Sketch of a Si chip with integrated electronic and photonic parts [26].

- (i) The group of Grützmacher and Buca [27] demonstrated an optically pumped GeSn laser. By the incorporation of >7 at.% Sn into the Ge lattice, the energy of the Γ -valley decreases below the L-valley resulting in a direct bandgap material making group IV materials suitable for laser application.
- (ii) Aiming for wireless communication in the telecommunication band (1550–1750 nm), Si is not suitable due to its large indirect bandgap

of 1.2 eV (1030 nm). Also, Ge based photodetectors are limited to spectral region at the edge of the C-band around 1550 nm (0.8 eV). To access the spectral region to the L- and U-band around 1620 nm 0.77 eV and 1650 nm 0.75 eV, respectively, the incorporation of Sn into Ge is necessary.

Finally, a further advantage of SiGeSn related materials is the possible monolithic integration into leading Si technology minimizing production costs setting up multi-functional systems. Group IV alloys can be integrated in the so called “Front-End-Of-Line (FEOL)” as well as in the “Back-End-Of-Line (BEOL)”. Due to its properties, Sn related materials can be utilized in CMOS technology (as a stressor or active material) as well as in Si photonics (as photodetector or laser material) in FEOL processes. Additionally, Sn-related devices can be potentially integrated in the BEOL, due to low process temperature preserving the other device structures.

This thesis focuses on group IV semiconductors as an innovative material for optoelectronics, namely photodetectors, integrable into a CMOS compatible process flow. Another aim is to overcome the dimension mismatch between the photonic part, typically in the range of μm , and the electronic part, which has already been miniaturized down to the nm regime. To do so, nanostructures are utilized for the formation of a photodetector. Recently, Niu et al. [28] demonstrated the photodetection of Ge nano-dots covered with a single graphene layer. As aforementioned, the incorporation of Sn is required, to enable the photodetection in the telecommunication bands. In fact the incorporation of moderate Sn contents of 2 at.% Sn, leads to a 10-fold increase of absorption at the C-band and a 20-fold at the L-band can resulting in an enhanced photoresponsivity compared to pure Ge [29]. The realization of monolithically integrated Si photonic devices is the combination of a GeSn laser as proposed by Wirths et al. [27] with a GeSn photodetector matching the spectral range of the laser is enabling the fabrication of group IV based Si photonic chips.

1.3 Aim and structure of thesis

As aforementioned, GeSn alloys are a promising material system for the “More than Moore“ trend. (Si)GeSn layers are extensively studied by various groups [30], [31], [32]. However, these layers suffer from Sn segregation as well as defects formation during plastic relaxation degrading the crystal quality. In this thesis, the reduction or suppression of both defects and Sn segregation is investigated by growth of GeSn nano-dots on nano-patterned Si wafers using advanced growth strategies. The structural and optoelectronic properties of the GeSn nanostructures are characterized. Finally, the possible application of a photodetector based on GeSn nanostructures for future high performance devices is evaluated.

Important aspects for the formation of GeSn nanostructures on a pillar-patterned Si(001) substrate are:

- successful selective growth of GeSn nano-islands of high crystal quality targeting the growth challenges discussed above (extended defects and Sn segregation),
- tuning the bandgap by varying the Sn content and
- optimizing the optoelectronic properties of GeSn nano-dots.

The doctoral thesis is arranged in the following chapters.

Chapter 2: An insight into growth theory as well as the details of the nano-islands growth via Molecular Beam Epitaxy (MBE) is given.

Chapter 3: The characterization methods to analyze (a) composition, crystal morphology, crystal quality and (b) the optoelectronic properties of the GeSn nanostructures will be explained.

Chapter 4: In this chapter, the main results of the thesis are presented, starting with the realization of the selective growth of GeSn nanostructures at different growth conditions and a fully structural characterization of these nano-crystals. Furthermore, successful strategies to control the incorporation of Sn will be demonstrated. The tunability of the bandgap

by varying the Sn content as well as possible routes for the improvement of the optoelectronic properties will be presented. Finally, first results on the ability of the GeSn nano-arrays to operate as a photodetector will be demonstrated.

Chapter 5: In the end, the results about the condition for selective growth of high-quality GeSn nano-islands will be summarized and an outlook of potential improvements for both the growth and photodetection of the GeSn nanostructures is given and future application are proposed.

2 | Growth theory and experimental set up

2.1 Growth theory

2.1.1 Atomistic processes at the surface during growth

When the atoms arrive at the substrate surface different processes can occur illustrated in Fig. 2.1

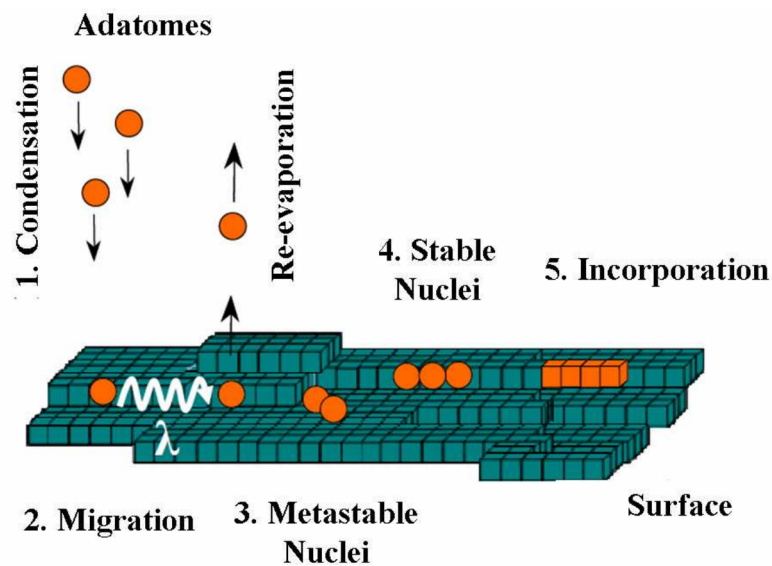


Figure 2.1: Schematic sketch of the nucleation during epitaxial growth on atomistic scale [33].

After the arrival of the adatoms at the substrate surface, condensation takes place. Hereafter, two processes are possible either (i) the re-evaporation of the adatoms or (ii) the formation of metastable nuclei. (i) occurs if the thermal energy is too high the adatoms desorb from the surface. (ii) occurs if kT is sufficiently high the adatoms migrate with a diffusion length λ on the surface jumping from one adsorption site to another. During migration the adatoms can combine to metastable nuclei continuing to diffuse on the surface. Once the nuclei reach a critical size and form a stable nuclei cluster, the adatoms are incorporated into the surface and will form a complete layer.

2.1.2 Growth modes

The epitaxial film growth is strongly influenced by the competition between the energetic gain of the formation of a crystal on the one hand and the cost of the formation of an interface and free surface of the deposited material on the other hand. Namely, the chemical potential $\mu(n)$ of n -deposited layers is an essential parameter which determines the growth mechanism and can be described as follows [33]

$$\mu(n) = \mu_\infty + [\varphi_a(n) - \varphi'_a(n) + \epsilon_d(n) + \epsilon_e(n)]. \quad (2.1)$$

Here, the chemical potential $\mu(n)$ depends on the bulk chemical potential μ_∞ , the desorption energy $\varphi_a(n)$ from the surface of the same material, the desorption energy $\varphi'_a(n)$ from a surface of a different material, the misfit dislocation energy per atom $\epsilon_d(n)$ and the homogeneous strain energy per atom $\epsilon_e(n)$. Clearly, the growth process is influenced by adhesive (attractive forces between different kinds of atoms) and cohesive forces (attractive forces between the same kind of atoms) as well as the (lattice and thermal) mismatch. Crucial for the determination of the growth mode is the thickness dependence of the chemical potential $\frac{d\mu}{dn}$, where three different growth modes can

be distinguished [33]

$$\frac{d\mu}{dn} < 0 \quad \text{when } \varphi'_a(n) < \varphi_a(n) \text{ at any misfit} \quad (2.2)$$

$$\frac{d\mu}{dn} > 0 \quad \text{when } \varphi'_a(n) > \varphi_a(n) \text{ at small misfit} \quad (2.3)$$

$$\frac{d\mu}{dn} \geq 0 \quad \text{when } \varphi'_a(n) > \varphi_a(n) \text{ at large misfit.} \quad (2.4)$$

Eq. 2.2 describes the case when the cohesive force of the adatoms is stronger than the surface adhesive force resulting in an island growth mode called *Volmer Weber* growth mode. In the case described by eq. 2.3, a layer-by-layer growth can be observed because the surface adhesive force is stronger than the adatom cohesive force, known as *Frank van der Merwe* growth mode. Equation 2.4 characterizes the third type of growth called *Stranski Krastanov (SK)* mode in which islands form on top of a wetting layer. From thermodynamic point of view, SK growth (see Fig. 2.2) is expected in case of the deposition of Ge, Sn or GeSn on Si.

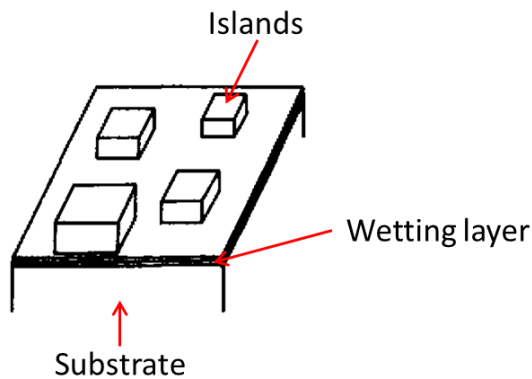


Figure 2.2: Schematic picture of the Stranski Krastanov mechanism corresponding to layer by layer growth followed by 3D islands [33].

The SK mode starts with an initial layer-by-layer growth. First, a strained wetting layer with one or few monolayers of the supplied atoms is formed (indicated by the black region in Fig. 2.2). During growth, the chemical

potential changes due to accumulated strain in the growing epi-layer. When a critical thickness h_c is reached the growth mode switches to island growth illustrated by cuboids. Here, either dislocated or coherent islands are formed depending on the misfit [34].

Note, that the aforementioned growth modes are assumed at thermodynamic equilibrium. Thus, growing far away from the equilibrium enables the change of the theoretically expected growth mode. That means, by careful control of the growth kinetics such as substrate temperature or evaporation flux, the deposition of a GeSn film on a Si substrate is possible.

2.2 Defect formation

Fig. 2.3 illustrates schematically the growth of Ge on Si, where the solid lines represent lattice planes. Due to the lattice mismatch, Ge shows only in the first monolayers a pseudomorphic growth on Si. Although there is only one pseudomorphic Ge layer shown in Fig. 2.3 (a), it was reported that several Ge pseudomorphic layers of 4 nm thickness can be formed on a Si(001) substrate [35]. In the pseudomorphic layer, the Ge layer has an in-plane compressive strain adapting to the Si substrate lattice. Additionally, an out-of-plane tensile strain is accumulated according to the Poisson ratio with respect to the in-plane deformation. After reaching the critical thickness h_c , the layer relaxes plastically forming Misfit Dislocations (MDs) marked by the red circle in Fig. 2.3 (b). Note, that the incorporation of larger atoms like Sn increases the strain and thus decreases h_c compared to pure Ge depending on the Sn content. Beyond h_c , first half loops nucleate at the surface and glide toward the Ge/Si interface. When the half loops reach the interface, MDs are formed at the interface with corresponding Threading Dislocations (TDs) within the layer (Fig. 2.3 (c)). Coupled to growth kinetics, these defects induce so called cross hatch patterns on the surface, resulting in strain relaxed but rough epi-layers.

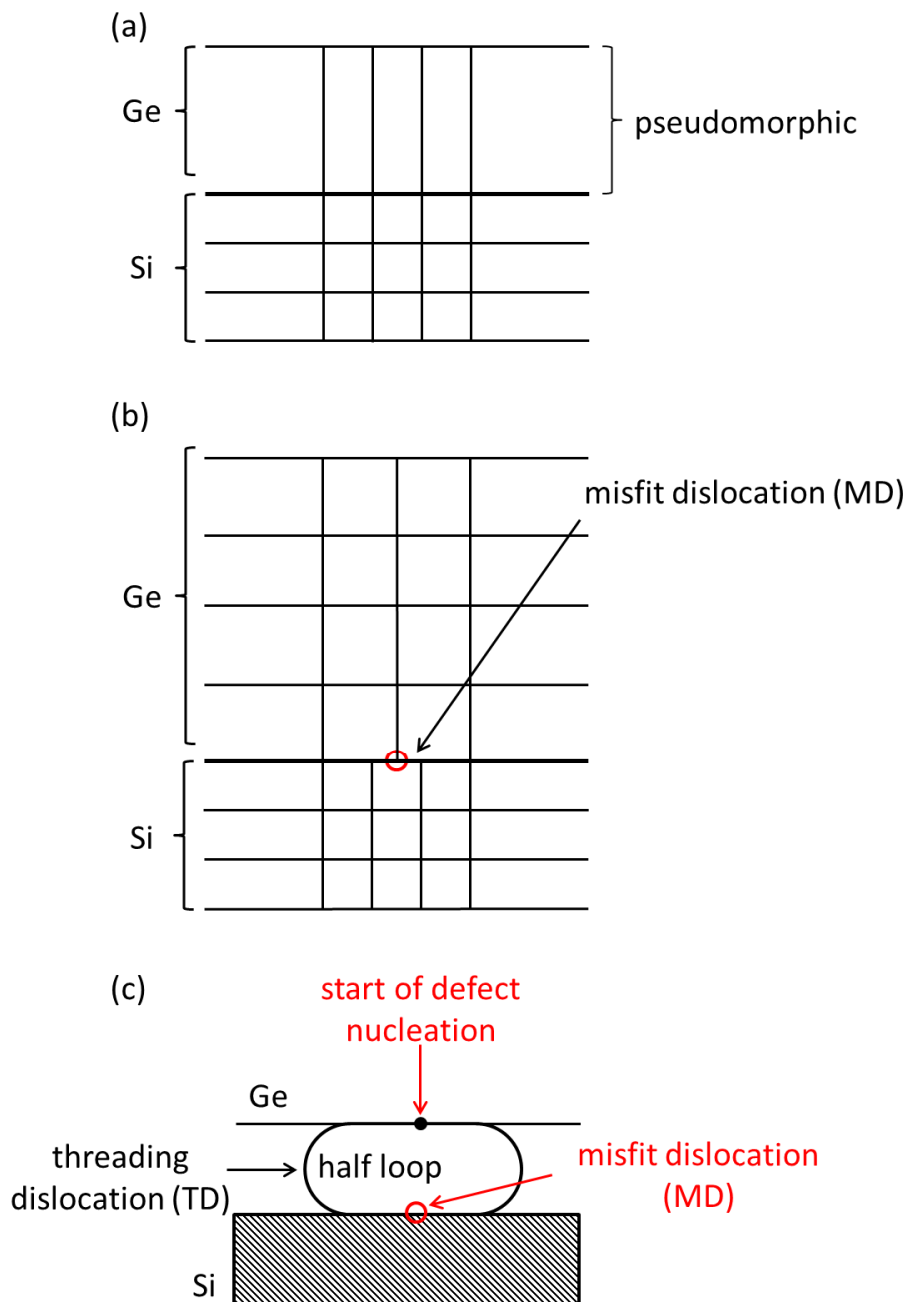


Figure 2.3: Schematic picture of (a) initial pseudomorphic growth of Ge/Si, (b) further growth of plastically relaxed Ge layer by introduction of threading dislocations (TD) and misfit dislocations (MD) as well as (c) detailed development of defect formation in planar systems [36].

Dislocation in the diamond lattice:

Dislocations are defined by the direction line \vec{l} and the Burger's vector \vec{b} , which can be determined by a Burger's circuit as shown in Fig. 2.4. Firstly

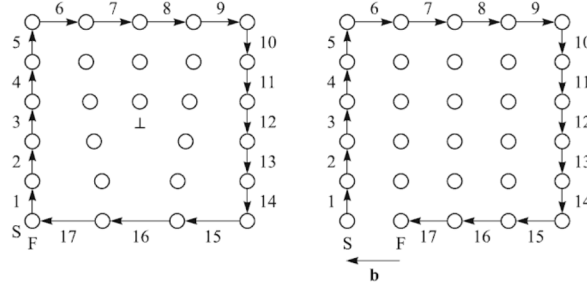


Figure 2.4: Schematic picture of the definition of the Burger's vector \vec{b} . First step is to form a closed circle (atom-to-atom) around the dislocation (left). Starting from point "S" and ending at "F". The second step is to draw the same atom chain in a perfect reference crystal (right). The missing vector between S and F is defined as Burger's vector \vec{b} [37].

a closed circle is formed from atom-to-atom enclosing the dislocations (Fig. 2.4 (left)). As a second step the same atom chain is formed in a perfect reference crystal (Fig. 2.4 (right)). The atom chain of the reference crystal will not close and hence, the vector which is needed to close the circle is called Burger's vector \vec{b} . Fig. 2.4 shows an edge dislocation where \vec{l} and \vec{b} are perpendicular to each other indicated by \perp , while in screw dislocations \vec{l} and \vec{b} are parallel [37].

Dislocations can move within the crystal along glide planes, which are in the diamond lattice the $\langle 111 \rangle$ planes. The shortest lattice vector which can be a Burger's vector is the half diagonal of a cube face $\frac{1}{2}\langle 110 \rangle$ [38]. Thus, the value of the Burger's vector in a diamond lattice is given by the lattice constant a as follows

$$|\vec{b}| = b = \frac{a}{2}\sqrt{2}. \quad (2.5)$$

As an example the Burger's vector of Si has a value of 0.384 nm according to Eq. 2.5.

Considering the Ge/Si system, pure edge (90°) dislocations are generated driven by plastic relaxation, due to the lattice mismatch of about 4.2 % [39].

In case of a smaller lattice mismatch ($< 4.2\%$) like in the SiGe/Si system with a low Ge concentration (e.g. 10%), 60° (angle between \vec{l} and \vec{b}) dislocations are mainly introduced at the SiGe/Si interface to relax the strain in the SiGe layer. The diamond structure has $\{111\}$ slip planes and $\langle 110 \rangle$ slip directions, which generate 60° dislocations in a layer [40]. In case of direct growth of GeSn on Si(001), 90° dislocations are promoted due to the large lattice mismatch ($> 4.2\%$). However, the $\text{Si}_{0.035}\text{Ge}_{0.915}\text{Sn}_{0.05}/\text{Ge}$ system shows 60° as well as 90° dislocations, while 60° dislocations are predominantly observed [41]. Additionally, the incorporation of Sn into Ge leads to a confinement of stacking faults trapping the dislocations at the GeSn/Ge interface, leading to high crystal quality of the grown GeSn layer [42].

2.3 Nanoheteroepitaxy

2.3.1 Theory

Beside plastic relaxation often observed in film growth, elastic relaxation mechanisms are pronounced in so called Nanoheteroepitaxy (NHE) reducing the defect density and thus, enabling the fabrication of future high performance devices. Fig. 2.5 shows a schematic picture (cross section view) of the mismatch stress relief mechanism occurring in NHE structures (left side) and in a layer formed by conventional planar heteroepitaxy (right side). In this example, the epilayer has a larger lattice constant than the substrate such as in case of Ge grown on Si. NHE growth (left side of Fig. 2.5) refers to the deposition of an epilayer (bright upper part) on a nano-patterned substrate (dark lower part) as suggested by Luryi and Suhir [43]. Ge deposited on the free-standing nano-pillar can elastically relax in three dimensions (indicated by arrows a, b and c). In contrast to NHE, in conventional planar heteroepitaxy (right side of Fig. 2.5) the elastic relaxation towards the horizontal direction is not possible due to the alignment of the lattice spacing of the planar layer with the one of the substrate. With increasing epilayer thick-

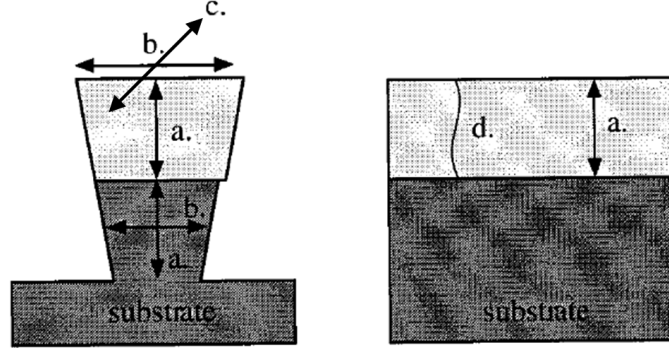


Figure 2.5: Schematic picture of the mismatch stress relief mechanisms occurring in nano-heteroepitaxial islands (left side) and in conventional planar heteroepitaxy (right side). The nanostructure can elastically relax in 3 directions indicated by arrows a., b. and c. [39].

ness, the strain energy is increasing and the out-of-plane lattice parameter is changed according to the Poisson's ratio, while the in-plane lattice spacing remains the same as the substrate. The epilayer is pseudomorphically growing on the substrate. When the epilayer thickness reaches a critical thickness h_c in case of planar heteroepitaxy, plastic relaxation occurs and dislocations are introduced in the deposited film reducing the strain energy. Threading arms of the introduced dislocations are likely to be found in the epilayer during planar growth as shown by the arrow "d" (right side of Fig. 2.5) [39]. In contrary to conventional planar heteroepitaxy, Luryi and Suhir [43] suggest an increase of h_c to infinite by patterning of the substrate. Consequently, in theory dislocation-free islands can be formed using the NHE approach due to three dimensional stress relief.

While the substrate proposed by Luryi and Suhir [43] is rigid and inflexible, Zubia and Hersee [39] extended their approach to the so called *substrate compliance* effect, i.e. part of the strain in the epilayer is shared by the substrate. Fig. 2.6 compares the strain energy accumulated during the growth of Ge on Si using different growth strategies. The strain energy depending on the epilayer thickness of Ge deposited on Si is compared with the energy to form a screw dislocation E_D taking into account the Young's modulus Y , the

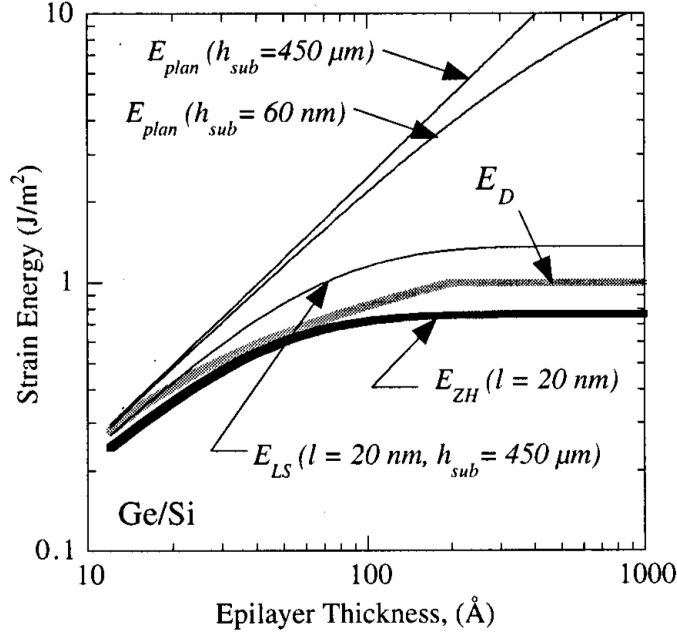


Figure 2.6: Strain energy plot depending on the epilayer thickness of Ge on Si comparing planar heteroepitaxial growth E_{plan} , NHE approach proposed by Luryi and Suhir E_{LS} and by Zubia and Hersee E_{ZH} . The energy to form a screw dislocation is indicated by E_D [39].

Poisson's ratio ν , the magnitude of the Burger's vector b , and the effective width of an isolated linear dislocation w_D as follows

$$E_D \approx \frac{Yb^2}{4\pi(1-\nu)w_D} \ln\left(\frac{R}{b}\right). \quad (2.6)$$

Here, R is the distance between the dislocation and the nearest free surface, i.e. in conventional heteroepitaxy R equals to the epilayer thickness. In standard planar growth, the strain energy E_{plan} is determined considering the stress ϵ and the Ge layer thickness h as follows

$$E_{plan} = \frac{Y}{1-\nu} \epsilon^2 h. \quad (2.7)$$

Fig. 2.6 shows for the case of planar growth that E_{plan} is higher than E_D already at an epilayer thickness of 20 Å, leading to the introduction of a

screw dislocation in the early growth stage. Decreasing the substrate layer thickness from 450 μm to 60 nm, results in a slightly decreased strain and a non-linear increase of the strain energy with increasing Ge thickness. When the substrate thickness is sufficient thin, meaning exhibits a similar height as the deposited layer, the *compliance* effect can be observed decreasing the strain in the epilayer.

The strain energy using the NHE approach can be determined by the strain in the epilayer ϵ_{epi0} and the effective height h_{epi}^{eff} , i.e. the effective extend of the stress zone in z direction

$$E_{epi} = \frac{Y_{epi}}{1 - \nu_{epi}} \epsilon_{epi0}^2 h_{epi}^{eff}. \quad (2.8)$$

with the epilayer thickness h_{epi} and the island radius of the nano-patterned substrate l

$$h_{epi}^{eff} = [1 - \text{sech}(k_{epi}l)]^2 \frac{1}{\pi} \left[1 - \exp\left(-\frac{\pi h_{epi}}{l}\right) \right] \quad (2.9)$$

and

$$k = \frac{Y_{epi}}{1 - \nu_{epi}} \frac{1 - \nu_{sub}}{Y_{sub}}. \quad (2.10)$$

In Fig. 2.6 the strain energy during the growth on nano-patterned Si substrates is compared with (E_{ZH}) and without (E_{LS}) the *substrate compliance* effect for a substrate island radius of 20 nm. The accumulated strain energy of both approaches is significantly smaller compared to planar growth. However, the growth of Ge on Si islands lacking the *compliance effect* results in defect-rich Ge islands because the strain energy E_{LS} exceeds E_D which is necessary to form a screw dislocation. Depositing on a Si substrate exhibiting partitioning of the strain with the Ge islands results in the formation of defect-free Ge because the strain energy E_{ZH} remains smaller than the energy E_D for the formation of a dislocation over the whole range of the investigated epilayer thickness.

The experimental proof of the *substrate compliance* effect has been given by Zaumseil et al. [44]. For that purpose, Ge was deposited on almost

strain-free nano-structured Si islands. After the Ge deposition, Si was tensile strained compensating the strain of the Ge islands and avoiding plastic relaxation.

In theory, infinitely thick Ge nano-islands can be grown without the introduction of defects if the Si substrate seed pad is sufficiently small (diameter ≤ 40 nm), due to the strain partitioning between the islands and the nano-patterned substrate as well as the 3D elastic relaxation mechanism [43]. Thus, NHE growth opens the way for nano-crystals with high quality and a coherent pseudomorphic interface without the introduction of neither MDs nor TDs. A similar approach is the growth of Nano-Wires (NWs) on planar substrates leading to high crystalline material due to mechanism of gliding out of TDs. However, the growth of NWs exhibits no coherent interface due to the lack of *substrate compliance* introducing MDs, which strongly limit the electron transport through the mismatched interfaces and hence, is degrading the performance of future devices.

Additionally in case of the deposition of Ge on Si, the NHE approach can decrease the interdiffusion of substrate atoms into the Ge islands. Georgiou et al. [45] calculated that the interdiffusion process is driven by surface – rather than bulk – diffusion. Consequently, by decreasing the island/substrate interface, it is possible to significantly decrease the volume ratio of Si interdiffusion to the total island provided that the islands exhibit a larger width than the substrate seeds.

2.3.2 Technical implementation of Nanoheteroepitaxy

Despite the promising theoretical prediction, one has to keep in mind the advanced technical realization of NHE growth.

Firstly, the patterning of nm-sized Si seeds are bound by the spatial limitation of the lithography system. Thus, theoretical demands for defect-free NHE growth can often not be matched in the experiment leading to the

introduction of defects in the nano-crystal. If the diameter of the nano-patterned Si seeds are too large disabling the *substrate compliance effect*, the lattice of the Si seeds do not bend because of the thin Ge top layer in the early growth stage of Ge/Si. Despite of the enhanced 3D elastic relaxation mechanism as proposed by Luryi and Suhir [43] and increase of the critical thickness h_c , the accumulated strain results in the introduction of MDs as well as TDs after reaching h_c . Fig. 2.7 some important features of defect formation in NHE Ge crystals grown on Si pillars are illustrated. Triggered by the increasing strain energy, the threading arms are moving to the edges of the Ge nano-islands. Due to the small volume of the Ge dot, the threading arms are gliding out of the nanostructure [46]. Hence, only the MDs at the Ge/Si interface can be observed, while the island crystal quality remains high because of the NHE approach pronouncing the mechanism of gliding out of the threading arms. This thesis focuses on the growth of GeSn on nano-

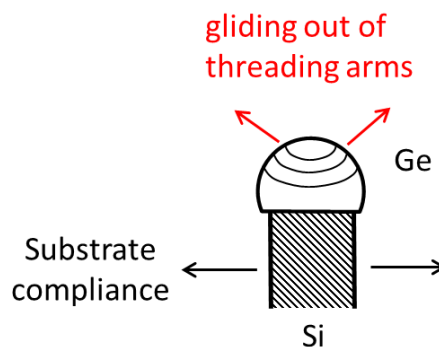


Figure 2.7: Schematic picture of defect formation observed in nano-heteroepitaxial islands.

patterned Si substrates. Due to the higher lattice mismatch of the GeSn/Si compared to Ge/Si, smaller Si seeds for high quality crystal growth of GeSn are required.

Secondly, selective growth on blanket nano-patterned Si wafer is not possible. The space between the Si pillars as well as the side walls have to be covered by SiO_2 . In previous studies, it was shown that the choice of the oxide matrix is crucial for the growth quality [47], [48], [44]. Thermal SiO_2

induces an in-plane compressive stress on the Si pillars and thus, is not suitable as spacer material for the selective growth of Ge/Si [49]. The opposite effect, inducing a tensile strain in the top part of the Si nano-pillars, was observed in case of a Chemical Vapor Deposition (CVD) grown SiO_2 mask using Tetraethylorthosilicat (TEOS) as precursor [48]. Tensile strained Si pillars can be beneficial for growth of Ge, in terms of reduced strain energy and thus decreased defect density.

2.3.3 Atomistic model of selective growth of Ge on Si

For the growth of $\text{GeSn}(\text{Si})$ nano-islands by NHE, Si nano-pillars are used which are embedded in a SiO_2 matrix. The $\text{GeSn}(\text{Si})$ nano-crystals must be formed by selective growth, i.e. $\text{GeSn}(\text{Si})$ is grown on the Si seeds without nucleating on the SiO_2 surface surrounding the Si nano-pillars. Fig. 2.8 illustrates a schematic diagram of different interactions between the adatoms as well as the surface clusters with the gas phase. Assuming an atomistic

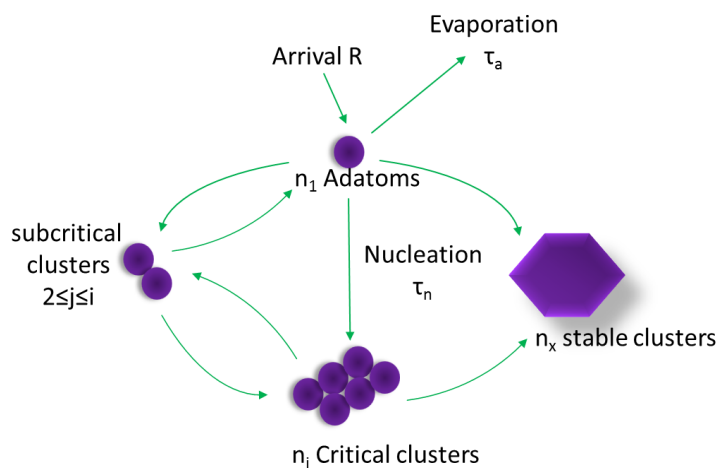


Figure 2.8: Schematic diagram of processes during nucleation and growth on substrate surfaces based on [50].

model, atoms arrive on a flat surface with an impingement rate of R . The density of these adatoms is given by n_i . Depending on the growth conditions, adatoms can either re-evaporate (characterized by an evaporation time τ_a) or

stay on the substrate surface (condensation). In the latter case, the adatoms either nucleate forming new clusters or are absorbed by existing stable clusters with the density n_x . However, newly formed clusters are unstable unless the adatoms' number in the clusters reaches a critical value of i . The nucleation of critical clusters (with the density n_i) is characterized by a time constant τ_n . All clusters with adatom numbers of j ($2 \leq j \leq i$) are subcritical clusters and thus are unstable.

The concentration of stable clusters is described by equation (2.11) [50]

$$\frac{n_x}{N_0} = C\eta(Z) \left(\frac{R}{N_0\nu} \right)^p \exp\left(\frac{E_n}{kT} \right). \quad (2.11)$$

Here, C (geometric constant) and $\eta(Z)$ (nucleation density, calculated for coverage Z) are constants, N_0 is the number of possible adsorption sites on substrates (e.g. $\text{SiO}_2 \approx 10^{15} \text{ cm}^{-2}$), ν is the characteristic surface vibration frequency ($\approx 10^{11}$ to 10^{13} s^{-1}), k is the Boltzmann's constant and T is the substrate temperature. The exponent p is related to the adatom number i in a critical cluster. The activation energy E_n is related to the binding energy E_i of the critical nucleus, diffusion energy E_{diff} as well as desorption energy E_{des} [50].

It is evident that n_x is a function of R and T . In order to quantitatively determine the value of n_x under certain R and T , one needs to identify p and E_n for each specific material system. Depending on the growth mode (2D or 3D) and condensation regime (extreme incomplete, initially incomplete and complete), p and E_n can be represented by different formulas. For the Ge/SiO₂ system, the growth mode is 3D considering the surface energies γ to be $\gamma_{Ge} + \gamma_{Ge/SiO_2} > \gamma_{SiO_2}$ where $\gamma_{Ge}(5\text{eV}/\text{nm}^2)$, $\gamma_{Ge/SiO_2}(10 \text{ eV}/\text{nm}^2)$ and $\gamma_{SiO_2}(4 \text{ eV}/\text{nm}^2)$ of the Ge surface, Ge/SiO₂ interface and SiO₂ surface, respectively [51]. According to a systematic study of Leonhardt et al. [52], at $T > 500 \text{ }^\circ\text{C}$, the condensation regime is treated as "extreme incomplete" resulting in

$$p = \frac{2i}{3} \text{ and } E_n = \frac{2}{3} [E_i + (i + 1) E_{des} - E_{diff}]. \quad (2.12)$$

Li et al. [53] performed a spectroscopy study and pointed out that for the Ge/SiO₂ system at $T > 500$ °C, $i = 3$, $E_{i=3} = 3.7$ eV, $E_{des} = 0.44$ eV and $E_{diff} = 0.24$ eV (thus $E_n = 3.48$ eV). It can be seen from the discussion above that Ge adatoms possess low desorption and surface diffusion activation barriers causing an extremely short characteristic surface diffusion length on SiO₂ which is much less than the distance between the nucleated islands. In fact the calculated diffusion length of Ge on SiO₂ surface (before desorption) is < 0.7 nm at $T > 500$ °C. Therefore, the stable clusters grow only due to direct impingement of the Ge atoms from the vapor phase on the clean Si surface [52]. Considering that the sublimation energy of Ge on Si surface $E_{sub}(4.25$ eV) is much higher than the $E_{des}(0.44$ eV) of Ge/SiO₂, one can certainly find a window to realize selective growth of Ge on SiO₂ on pre-patterned Si substrates. In this case, the Ge atoms nucleate only to the exposed Si area while desorbing from the SiO₂ surface [52].

In fact, Niu et al. [54] showed the selective growth of high quality Ge islands on nano-patterned Si(001) by exploiting the desorption mechanism of Ge on Si and SiO₂, respectively. However, little is known about the influence of Sn on the selective NHE growth on nano-patterned Si(001) substrates.

2.4 Growth techniques

There are various growth techniques to grow epitaxial layers like MBE, CVD, liquid–vapor phase epitaxy and much more. The advantage of a CVD reactor is the growth of homogeneous layers on large substrates for mass production. However, to grow via CVD one has to keep in mind various chemical reactions on the substrate surface, while MBE growth is a purely physical process achieving high purity and crystalline material systems. To study the fundamental principles of GeSn growth, the formation of GeSn nanostructures on nano-patterned Si(001) substrates was realized by MBE.

Molecular beam epitaxy

In MBE the materials of interests are typically evaporated from solid sources in Ultra High Vacuum (UHV) conditions in the pressure regime of $\leq 10^{-9}$ Torr or $1.33 \cdot 10^{-7}$ Pa. This low pressure is crucial for the arrival of the evaporated material at the substrate surface depending on the mean free path \bar{L} of the atoms. \bar{L} is drastically increased compared to ambient pressure considering the Boltzmann constant k_B , the temperature T , the pressure p and the molecular diameter d defined as follows [55]

$$\bar{L} = \frac{k_B \cdot T}{\sqrt{2} \cdot \pi \cdot p \cdot d^2} . \quad (2.13)$$

As an example, with the typical working pressure in a MBE system of about 10^{-10} to 10^{-11} Torr a free mean path of about 10^6 m can be reached whereas at ambient pressure the corresponding mean free path is only few nm in which the molecules collide with each other. Thus, the evaporated molecules can easily reach the substrate which is about 0.2 m away from the solid sources. Another reason for the UHV conditions is to avoid the incorporation of contaminants, which can lead to defect crystal growth of the desired material.

Fig. 2.9 shows a picture of the MBE laboratory with the MBE cluster (top) and in detailed the Si–Ge–Sn chamber (bottom) at IHP. The MBE laboratory provides three MBE chambers from DCA for oxide, III–V and Si/Ge/Sn materials as well as a CVD chamber from Riber for graphene growth (Fig. 2.9 (top)). Ge (solid source) was evaporated by an electron beam gun with high power and thus accessing a relatively high beam flux. (Fig. 2.9 (bottom)) Sn was evaporated by a Knudsen cell with a resistive heating source. Additionally, it is possible to generate e.g. a hydrogen plasma by radio frequency (RF) with a Dressler Cesar RF Power Generator injecting a plasma in the MBE chamber. Furthermore, the MBE system is equipped with a Reflection High–Energy Electron diffraction (RHEED) and is connected to an in-situ X–Ray Photoelectron Spectroscopy (XPS) chamber.

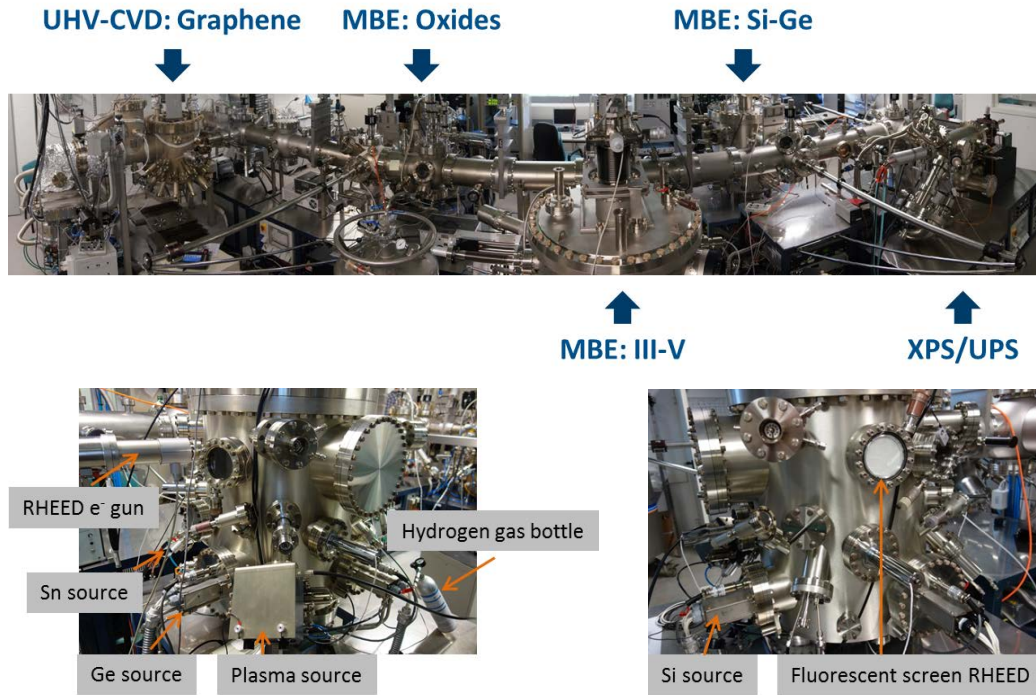


Figure 2.9: Pictures of the MBE cluster of four chambers (top) and detailed pictures of the Si-Ge MBE chamber with the description of the most important components (bottom).

2.5 Growth challenges SiGeSn

The heteroepitaxial growth of Sn-based alloys on Si or Ge deals like many material systems with the problem of thermal and lattice mismatch. Furthermore, the incorporation of Sn into bulk Si and Ge is challenging, due to the low solubility. Therefore, one has to tailor the growth parameters to achieve

- low defect density in crystalline structures and
- controlled chemical composition.

Details of the growth challenges and strategies to gain high crystalline (Si)GeSn with well controlled chemical composition will be discussed in the

following.

The lattice misfit in case of pure Ge on Si is 4.2 % [56]. The lattice mismatch between α -Sn and Ge or Si is even higher with a mismatch of about 15 and 19 %, respectively [10], [11]. In addition to the lattice mismatch, Si, Ge and Sn also exhibit a mismatch in the Coefficient of Thermal Expansion (CTE). Hereby, Si exhibits a CTE of about $2 \times 10^{-6} \text{ }^\circ\text{C}^{-1}$, Ge about $6 \times 10^{-6} \text{ }^\circ\text{C}^{-1}$ [57] and β -Sn about $22 \times 10^{-6} \text{ }^\circ\text{C}^{-1}$ at 25 °C [58]. As mentioned before, Sn has a very low solubility in pure Ge (1 at. % [10]) and Si (0.1 at. % [11]), respectively. Consequently, Sn segregation/precipitation can be observed in (Si)GeSn systems, especially at higher temperatures than eutectic temperature T_{ec} . Additionally, GeSn alloys possess a plastic relaxation mechanism caused by Sn precipitation. The diffusivity of Sn atoms in Ge is enhanced by two to three orders of magnitude along dislocations via vacancies compared to *bulk* diffusion [59], [60]. These Sn precipitates are expected to crystallize in the stable β -phase. In fact, Groiss et al. [61] investigated the behavior of these Sn segregates at $T > T_{ec}$. Hereby, β -Sn droplets were monitored on a $\text{Ge}_{0.9}\text{Sn}_{0.1}$ layer surface by Scanning Electron Microscopy (SEM) during thermal treatment. It was shown that the liquid Sn droplets move on the surface causing a phase separation of the GeSn layer and simultaneously re-depositing crystalline Ge (with a Sn content $< 1 \text{ at.}\%$) at the trailing edges. Interestingly, the trail of the recrystallized Ge exhibit low energy facets of pure Ge like $\{001\}$, $\{105\}$ and $\{113\}$. Additionally, small Sn *droplets* can be observed on $\{111\}$ facets within the trail.

Formation of SiGeSn alloys

One strategy to increase the Sn concentration and to prevent Sn segregation, is the formation of ternary alloys $\text{Si}_y\text{Sn}_x\text{Ge}_{1-x-y}$.

Fig. 2.10 shows a contour map of the Gibbs free energy (ΔG) for specific (Si)GeSn alloys, namely $\text{Si}_{4x}\text{Sn}_x\text{Ge}_{1-5x}$ where each Sn atom is assumed to replace four Si atoms, and $\text{Sn}_x\text{Ge}_{1-x}$, with various Sn contents at different temperatures. The white solid line indicates the instability boundary which

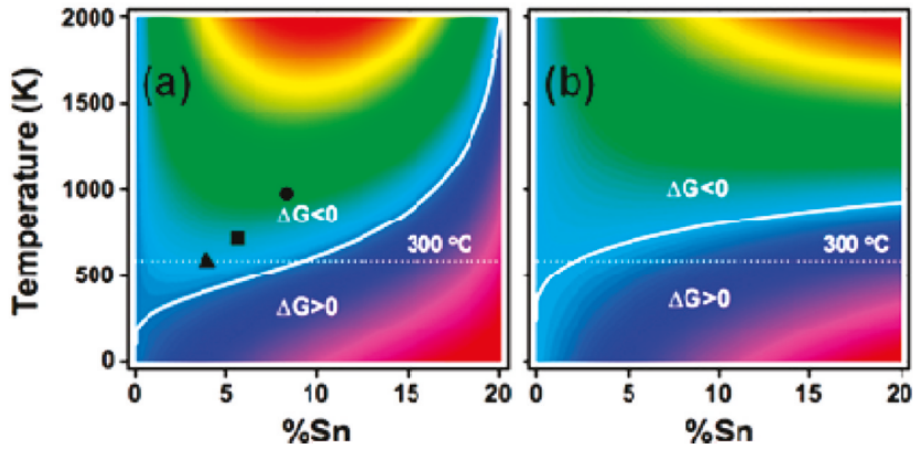


Figure 2.10: Contour plot of the Gibbs free energy for an alloy $\text{Si}_{4x}\text{Sn}_x\text{Ge}_{1-5x}$ (a) and $\text{Sn}_x\text{Ge}_{1-x}$ (b) in dependency of the Sn content and the temperature. The bold white line indicates the stability boundary $\Delta G = 0$. The solid black triangle, square and circle represent local minima of ΔG at 573, 673 and 973 K, respectively [62].

separates the stable condition with negative ΔG from the unstable one (positive ΔG .) The solid black triangle, square and circle represent the local minimum of ΔG at 573, 673 and 973 K, respectively. There are two main messages from these two diagrams.

- First of all, a higher content of Sn can be incorporated in the ternary alloy $\text{Si}_{4x}\text{Sn}_x\text{Ge}_{1-5x}$ than in the binary alloy $\text{Sn}_x\text{Ge}_{1-x}$. At 573 K (300 °C) the maximum Sn content in the stable condition in the binary system is about 2 at.%, whereas in the ternary system a Sn incorporation of 10 at.% is still stable.
- Secondly, with increasing temperature more Sn can be incorporate because of the contribution of the mixing entropy. The amount of stable Sn increases with increasing temperature. In case of the ternary system the local minimum of the Gibbs free energy is about 4 at.% to 5 at.% at 573 K and about 12 at.% at 673 K. In general by using a ternary instead of a binary system, results in a higher stability for the same Sn content and thus prevents Sn segregation [62].

Even though the incorporation of Si into GeSn enables the tunability of the

lattice parameter, the formation of the ternary alloy has the drawback of increasing the bandgap due to Si compensating partly the shrinkage effect of Sn.

Growth at non-thermodynamic equilibrium conditions

Another approach to overcome the low solubility and increase the incorporation of Sn into the Ge lattice in a binary alloy, is to grow far away from the thermodynamic equilibrium. Taoka et al. [63] demonstrated that a higher Ge deposition rate of about 13 nm/min (compared to < 3 nm/min) successfully decreases the migration of the Sn atoms. Thereby, it was possible to incorporate about 3 at.% Sn into the Ge layer at a growth temperature as high as 400 °C. Using a high Ge flux, GeSn layers with high crystallinity and good optoelectronic properties can be formed exceeding the thermodynamic solubility by carefully controlling the Sn atom migration at elevated temperatures.

Moreover, by subsequent overgrowth of GeSn by Ge, one can trap the Sn atoms inside the GeSn alloys preventing Sn segregation out of the deposited film/nanostructures.

It is quite important to comprehensively understand the relationship between growth temperature and flux on the one hand (experimental parameters) and strain, relaxation and Sn incorporation on the other hand (film properties).

2.6 Wafer and sample preparation

Substrate fabrication

The so called Si nano-tips (investigated by Niu et al. [54]) could not be used in this thesis, due to technological problems which hindered the removal of the oxide from the Si seeds. Thus, so-called Si nano-pillars were chosen for

the growth experiments. The main difference between these two substrates is the size of the Si seeds. The diameter of the nano-tips is about 50 nm to 90 nm, while the pillars used in the following experiments exhibit a diameter of 90–100 nm. The Si-pillars are fabricated by using photolithography with deep ultraviolet light and are embedded in a SiO₂ matrix formed by plasma-enhanced CVD using TEOS as a precursor. The process flow is described in [64] starting with a p- or n-type Si(001) test wafer.

1. 2.5 nm thick SiO₂ layer by wet oxidation
2. 21 nm thick Si₃N₄ layer by CVD
3. Photolithography two times exposure of gitter mask (second exposure is 90° rotated from first one to form dots array)
4. Formation of Si pillars with 100 nm depth and 130 nm diameter by reactive ion etching
5. Ash (remove photoresist)
6. Shrinking pillar diameter to ca. 100 nm by Godbey etch
7. Removal of Si₃N₄ hardmask on Si pillar by H₃PO₄ etch
8. Removal of native SiO₂ from sidewall and Si surface around the pillars by HF dip
9. Deposition of 400nm thick SiO₂ by CVD to cover whole structure by SiO₂
10. Chemical Mechanical Polishing (CMP) 10 nm above Si pillar
11. Open Si pillar surface (about 10–20 nm of Si pillar is opened) by HF dip

Two different Si test wafers have been used either with p- or n-doping. In case of the Boron doped p-type wafer, Si exhibits a specific resistivity of 5–22 Ω cm, whereas the Antimon (Sb) doped n-type Si shows a specific resistivity of 0.01–0.02 Ω cm.

Sample preparation

For the formation of GeSn nanostructures, nano-patterned Si wafers were used for deposition by MBE. To ensure high crystal quality of the deposited GeSn, it is necessary that the pillar substrate is free of impurities. To realize this, the following steps were used to prepare the Si nano-pillar substrate.

1. Cutting the wafer (2 x 2 cm)
2. Wet chemical cleaning
 - (a) H₂O:H₂SO₄ 1:4 for 30 s
 - (b) Rinsed in De-Ionized Water (DIW) for 60 s
 - (c) Etching surface oxide layer by a diluted HF solution with concentration of 0.5 % for 12 s
 - (d) Rinsed in DIW for 60 s
3. Loading of the samples into the MBE chamber
4. Prebake at 800 °C in the MBE chamber for 5 min
5. Ge, Sn or GeSn deposition using MBE method

The procedure of the wet chemical cleaning of the nano-patterned Si wafers was established by Niu (see [54]) adjusting the time of the HF dip long enough to remove the native SiO₂ from the Si pillar surface, but short enough to preserve the SiO₂ on the Si pillar side walls. After the substrate was cleaned wet chemically at ambient pressure, it was immediately transferred to the UHV systems. Hereafter, the Si pillar substrate was cleaned thermally in the MBE chamber under UHV conditions at a base pressure of 5×10^{-10} mbar. In Fig.2.11 a SEM image of a cleaned substrate surface as well as a schematic sketch is shown. After substrate cleaning the main part of the Si nano-pillars is still covered by SiO₂ which is crucial for the selective NHE growth. All GeSn samples were grown via MBE by co-evaporation of Ge and Sn at 1×10^{-8} mbar.

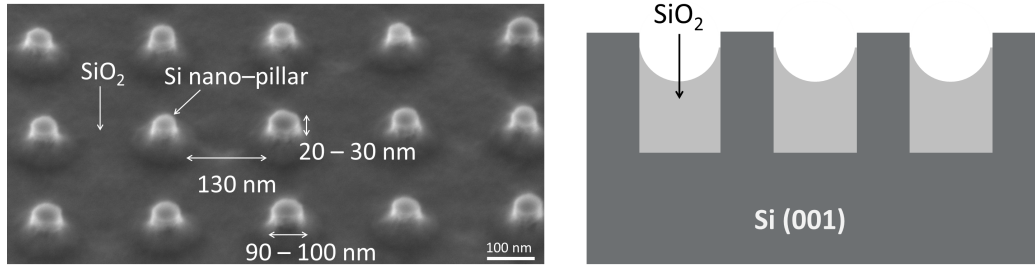


Figure 2.11: SEM image (left) of the Si nano-pillar substrate after the 5 min annealing at 800 °C observed at a tilting angle of 40°. The dimensions of the pillars and the spacing are noted in the image. Schematic sketch (right) of the cross section of the Si nano-pillar substrate.

For the first set of GeSn nanostructures, Ge and Sn were co-deposited for 5 or 20 min at a Ge rate of 7.0 ± 1.5 nm/min and a Sn cell temperature of 1050 °C aiming for 4 at.% Sn. The investigated substrate temperature varied between 500 °C and 750 °C. Ge reference samples were deposited under the same growth conditions. Furthermore, a second set of GeSn nanostructures was prepared by subsequent deposition of a Ge cap. After the 5 min co-evaporation of Ge and Sn, a 5 min overgrowth of pure Ge followed, while the substrate temperature was maintained for both processes. The other growth parameters like Ge deposition rate, Sn cell temperature and substrate temperature range were the same as for the first set of samples.

The growth conditions of all samples presented in this thesis are summarized in Tab. 2.1 with the corresponding characterization techniques discussed in this thesis.

Table 2.1: Overview of growth conditions (substrate temperature, Ge flux, Sn cell temperature, deposition time) of all samples and characterization techniques: SEM, AFM, XRD, TEM, EDX, I/V curves and photocurrent (PC).

sample ID	T [C]	dep. rate [nm/min]	Sn cell T [C]	dep. time [min]	Characterization
Ge01	600	5.4	-	20	SEM, PL
Ge02	750	5.4	-	20	SEM, PL
Ge03	650	5.4	-	20	SEM, PL
Ge25	850	0.8	-	140	SEM, EDX, TEM, I/V, PC
Ge30	850	0.8	-	80	SEM, EDX, TEM, I/V, PC
GeSn09	750	5.4	1050	20	SEM, XRD, TEM, EDX, PL
GeSn10	650	5.4	1050	20	SEM, XRD, TEM, EDX, PL
GeSn11	600	5.4	1050	20	SEM, XRD, TEM, EDX, PL
GeSn12	500	5.4	1050	20	SEM
GeSn14	600	5.4	1100	20	SEM, XRD
GeSn15	600	5.4	1050	5	SEM, AFM, EDX, PL, TEM, I/V, PC
GeSn15star	600	5.4	1050	5	SEM, TEM, I/V, PC
GeSn18	600	8.4	1050	5	SEM, XRD
GeSn39	600	5.4	1050	5 (GeSn) / 5 (Ge)	AFM, EDX, XRD, PL
GeSn43	650	5.4	1050	5 (GeSn) / 5 (Ge)	AFM, EDX, XRD, PL
GeSn44	750	5.4	1050	5 (GeSn) / 5 (Ge)	AFM, EDX, XRD, PL
GeSn46	600	5.4	1050	5	SEM, EDX, TEM, I/V, PC

3 | Characterization techniques

In this chapter the principles of the characterization techniques are described to analyze the morphology, lattice and the optoelectronic properties of the grown nanostructures.

3.1 Characterization of morphology

To judge the degree of selectivity of the GeSn nano-islands grown with MBE, the samples are analyzed using two different microscopy techniques. In addition to that, the nano-crystal morphology, such as the facet angle distribution, will be evaluated at a statistical level.

3.1.1 Scanning electron microscopy

In SEM highly accelerated electrons are utilized to generate high resolution microscopy images. When the electrons are hitting the sample surface they are either (i) elastically or (ii) inelastically scattered. In case (ii) the incoming electron is transferring energy to the sample which can cause the excitation of Secondary Electrons (SE), Auger-, Photoelectrons or X-ray radiation. For the acquisition of SEM images usually SE and Backscattered Electrons (BSE) are used. All SEM images of this thesis have been acquired

by a ZEISS Merlin Gemini II microscope. The electrons are accelerated from a tungsten filament with 1.5 kV.

Additionally, the microscope can analyze BSE with an Energy selective Backscattered (EsB) detector generating contrast images. Here, heavier atoms appear brighter than lighter atoms, which can be used e.g. to distinguish between Si, Ge or Sn. The contrast images are a first indication of the presence of β -Sn segregation out of the GeSn islands. However, to confirm the presence of Sn droplets or analyze the island morphology quantitatively further characterization has to be considered.

3.1.2 Atomic force microscopy

Atomic Force Microscopy (AFM) is a characterization technique to analyze the topography, surface potential, electrical and magnetic properties of the material of interest. There are mainly three different AFM measurement modes: *contact mode*, *non-contact mode* and *tapping mode* [65]. In this thesis, AFM measurements are acquired in *tapping mode*, also known as *intermittent contact mode*. Hence, only this mode will be explained further, while more information of the different AFM measurement types can be found e.g. in Ref. [65]. The work principle of an AFM is illustrated in Fig. 3.1. A flexible cantilever base equipped with a sharp tip is excited by a piezoelectric actuator with a constant sinusoidal driving force ω_{drive} slightly below the resonant frequency of the tip, ensuring a longer preservation of the tip. Due to the reduction of the tip bending and the non-contact mode, a sharp is maintained and a hence a high lateral resolution of the measurement is guaranteed. The tip atoms react with the sample surface atoms mainly caused by attractive tip-sample interactions, the so called Van der Waals forces. The change of the amplitude of the bended cantilever is detected by a laser light reflected on the backside of the cantilever and is collected by a position sensitive photodetector. Both the detection signal (preamplifier) converted into voltage and the reference signal of ω_{drive} (lock-in-amplifier) are used for the z-feedback controller maintaining a constant oscillation amplitude. In this

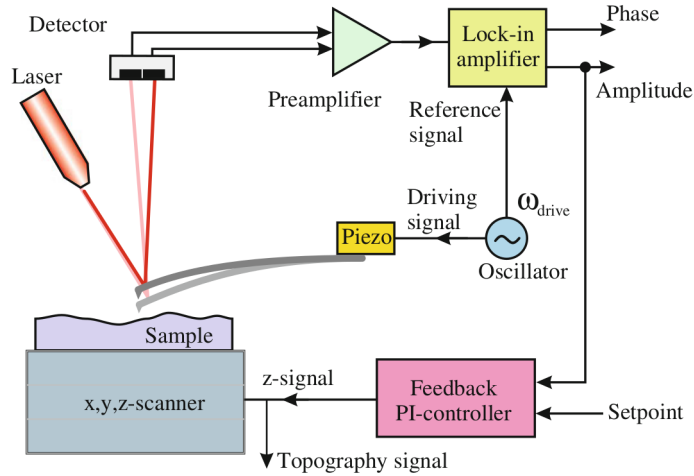


Figure 3.1: Illustration of an experimental AFM setup for an amplitude modulation detection [65].

way the topography of the sample surface can be obtained with a sub-nm resolution in z-direction and a lateral resolution strongly depending on the tip geometry. Additionally, the lock-in-amplifier detects phase and amplitude as free signal providing further insight to the tip-sample interactions such as composition and elastic properties of the sample, respectively.

In this thesis, the AFM measurements were carried out in tapping mode by a Bruker microscope (Dimension Icon) equipped with a super sharp Si TESP-SS probe with a 2 nm tip radius and a resonant frequency of 320 kHz [66]. In this way, high lateral resolution images of the GeSn nanostructures have been obtained, providing a source for comprehensive statistical analyses (island size, volume and much more) as well as the determination of the facet distribution of the nano-islands visualized in pole figures. To exclude artifacts generated by the tip, the shape of the Si tip modeled by Fourier transformation was verified and the acquired images were analyzed by the software Gwyddion with an intact tip shape.

3.2 Characterization of lattice

The chemical composition, the degree of strain as well as the crystal quality is characterized by two different techniques: one provides a local characterization of one GeSn nano-dots, while the other method gives average information about the lattice gained from many islands.

3.2.1 X-ray diffraction

Kinematical scattering theory

When a crystalline material of interest is exposed to monochromatic X-rays, the incoming waves are scattered at the electrons of the atoms causing scattered waves, which can interfere in a constructive or destructive way. The X-Ray Diffraction (XRD) pattern caused by the constructive interference of the scattered waves can be used for detailed analysis of the crystal's properties. The following discussion of the analysis of the scattering processes is based on *kinematical* diffraction theory and thus, multiple scattering events are neglected [67], [68]. A deeper insight to the corresponding *dynamical* scattering theory can be found in [67]. Figure 3.2 shows the schematic scattering of an unpolarized monochromatic beam on a very small crystal.

The unit vectors s_0 and s define the propagation direction of the initial and scattered X-ray beam with the wavelength λ . R_m describes the location of the unit cell and r_n the position of the n_{th} atom in the cubic unit cell with $N_i a_i$ ($i = 1, 2, 3$) edges along a_i crystal axes. The intensity of the scattered beam is observed at point P at a distance R from the crystal and is described by equation 3.1

$$I = I_e \cdot F^2 \cdot G^2. \quad (3.1)$$

The intensity I comprises (i) the pre-factor I_e describing the interaction of X-rays with a free electron, (ii) the structure factor F taking into account

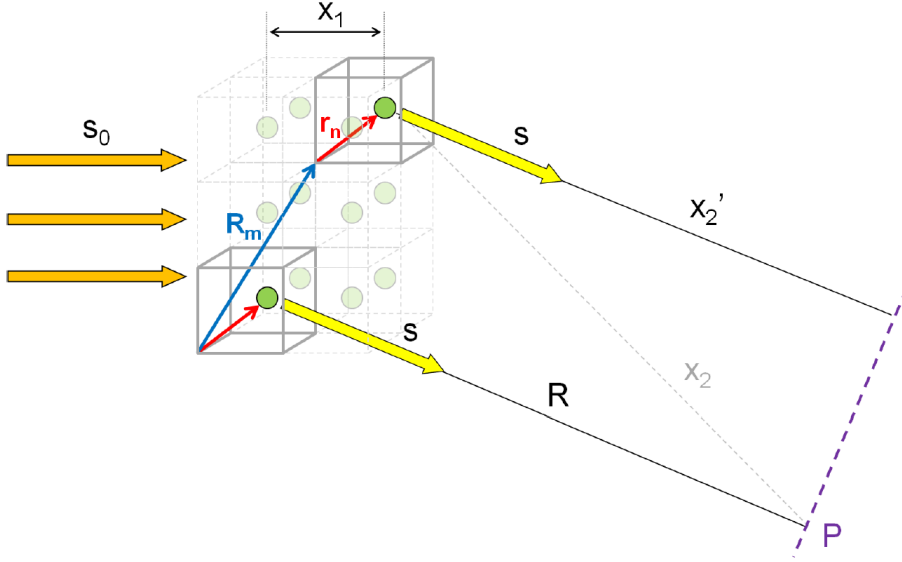


Figure 3.2: Schematic figure of the scattering of a parallel X-ray beam on a small crystal. R_m defines the position of m^{th} unit cell and r_n describes the position of n^{th} atom in a unit cell. Because of the small size of the crystal it can be assumed that the primary and the scattered beam are plane waves which leads to $(x_1 + x_2) \rightarrow (x_1 + x_2')$ [67].

the atomic arrangement of the crystal unit cell and (iii) the lattice factor G considering the size and periodicity of a crystal.

- (i) The pre-factor I_e consists basically of the THOMSON scattering at an angle θ and is defined in equation 3.2 by the intensity of the incident X-ray beam I_0 , the electron charge e , the electron mass m and the speed of light c

$$I_e = I_0 \cdot \frac{e^4}{m^2 c^4 R^2} \left(\frac{1 + \cos^2(2\theta)}{2} \right). \quad (3.2)$$

The factor $\left(\frac{1 + \cos^2(2\theta)}{2} \right)$ is called the polarization factor for an unpolarized primary beam and the constants $\frac{e^4}{m^2 c^4}$ give the scattered intensity of a single electron of about $8 \times 10^{-26} \text{cm}^2$. This value is quiet small but one has to consider that there are approximately 10^{20} electrons in 1 mg material.

- (ii) Taking in account all atoms n of the unit cell, the structure factor F describes their scattering strength and is defined as follows

$$F = \sum_n f_n e^{\frac{i2\pi}{\lambda}(s-s_0)r_n} . \quad (3.3)$$

The atomic form factor f_n determines the scattering intensity of the sum over all electrons of one atom. Therefore, F depends on the crystal systems of the investigated material.

- (iii) Finally considering the whole crystal, the lattice factor G is defined as follows

$$G = \frac{\sin \left[\left(\frac{\pi}{\lambda} \right) (s - s_0) \cdot N_1 a_1 \right]}{\sin \left[\left(\frac{\pi}{\lambda} \right) (s - s_0) \cdot a_1 \right]} \cdot \frac{\sin \left[\left(\frac{\pi}{\lambda} \right) (s - s_0) \cdot N_2 a_2 \right]}{\sin \left[\left(\frac{\pi}{\lambda} \right) (s - s_0) \cdot a_2 \right]} \cdot \frac{\sin \left[\left(\frac{\pi}{\lambda} \right) (s - s_0) \cdot N_3 a_3 \right]}{\sin \left[\left(\frac{\pi}{\lambda} \right) (s - s_0) \cdot a_3 \right]} . \quad (3.4)$$

The intensity depends strongly not only on the number of coherently scattering unit cells $N_i (I \propto G^2)$ but on certain geometric conditions, namely on the direction of the unit vectors s and s_0 with respect to the crystal orientation. For constructive interference, the three terms of the lattice factor in equation 3.4 have to be close to their maxima in order to observe a XRD signal. These conditions lead to the Laue equations

$$\frac{2\pi}{\lambda} \cdot \frac{\vec{s} - \vec{s}_0}{\lambda} \cdot a_1 = h \cdot 2\pi \quad (3.5)$$

$$\frac{2\pi}{\lambda} \cdot \frac{\vec{s} - \vec{s}_0}{\lambda} \cdot a_2 = k \cdot 2\pi \quad (3.6)$$

$$\frac{2\pi}{\lambda} \cdot \frac{\vec{s} - \vec{s}_0}{\lambda} \cdot a_3 = l \cdot 2\pi . \quad (3.7)$$

The integer numbers h, k, l are called Miller indices and a_n is the lattice constant. The condition for constructive interference is given by the Laue equations, i.e. that the incoming wave has to be scattered

elastically in such a way that the term $\frac{\vec{s}-\vec{s}_0}{\lambda} \cdot a_n$ is an integer multiple of the three Miller indices. Another common interpretation of the Laue equations is the Bragg equation 3.8 depending on λ of the incoming X-ray beam and the θ angle of the corresponding diffraction pattern

$$n\lambda = 2d_{hkl}\sin\theta. \quad (3.8)$$

Consequently, the Bragg angle θ depends on the net plane distance d_{hkl} of the investigated crystal system. Si, Ge and GeSn exhibit a diamond lattice which is assigned to the *face-centered cubic (fcc)* Bravais lattice. One can derive the lattice parameter a from the net plane distance d as defined in equation 3.9 for cubic systems

$$d_{hkl} = \frac{a}{\sqrt{h^2 + k^2 + l^2}}. \quad (3.9)$$

Since the diffraction pattern is limited to certain reflections considering the unit cell geometry, constructive interference in case of a diamond lattice can only be observed for odd hkl values. Additionally, F is different from zero (see eq. 3.3) if all hkl values are even and the sum is divisible by 4 e.g. the (400) reflection.

Mixed hkl values e.g. (123) can not be observed because F equals to zero at this condition.

With the theoretical background of kinematical scattering theory, one can choose the appropriate experimental configuration for a comprehensive characterization of the crystalline material of interest.

X-ray experimental set up

All XRD measurements were carried out using a laboratory-based diffractometer. The Rigaku SmartLab diffractometer is equipped with a 9 kW rotating Cu anode and the Cu K_{α_1} radiation with a wavelength of $\lambda = 0.154056 \text{ nm}$ is used. The samples were analyzed in two different measurement configurations.

The first configuration is the so called specular measurement mode shown in

Fig. 3.3. Hereby, the X-ray source and detector are moved simultaneously in $\theta - 2\theta$ mode while the sample is fixed horizontally (see Fig. 3.3 left). From the resulting XRD pattern, one can obtain interplanar spacing of the lattice planes which are parallel to the samples surface, i.e. the out-of-plane lattice parameter of the investigated material (see Fig. 3.3 right).

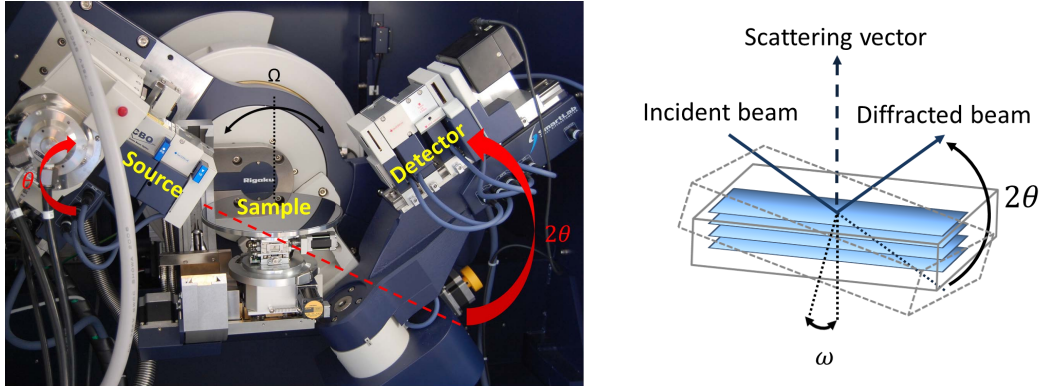


Figure 3.3: Rigaku SmartLab diffractometer in specular configuration during $\theta - 2\theta$ measurement (left). Sketch of a $\theta - 2\theta$ scan showing the measured lattice planes (right) [69].

To obtain the angular spread of the lattice planes in out-of-plane orientation, a 2θ reflection is measured, while rotating the sample around the ω angle. The out-of-plane deviation of the crystallite is called tilt and the diffraction pattern is known as rocking curve or ω scan.

The second configuration is the so called in-plane diffraction shown in Fig. 3.4. In this configuration the X-ray beam hits the sample in a grazing incident angle α_i typically between 0 to 0.6° . The samples is rotated by ϕ around its surface normal, while the detector is rotated by $2\theta_\chi$ (see Fig. 3.4 left). The resulting diffraction pattern gives the in-plane lattice parameter caused by scattering of the lattice planes which are perpendicular to the sample surface (see Fig. 3.4 right). By varying ϕ the variation of the in-plane orientation of the lattice planes of the deposited material, the so-called twist distribution, can be determined.

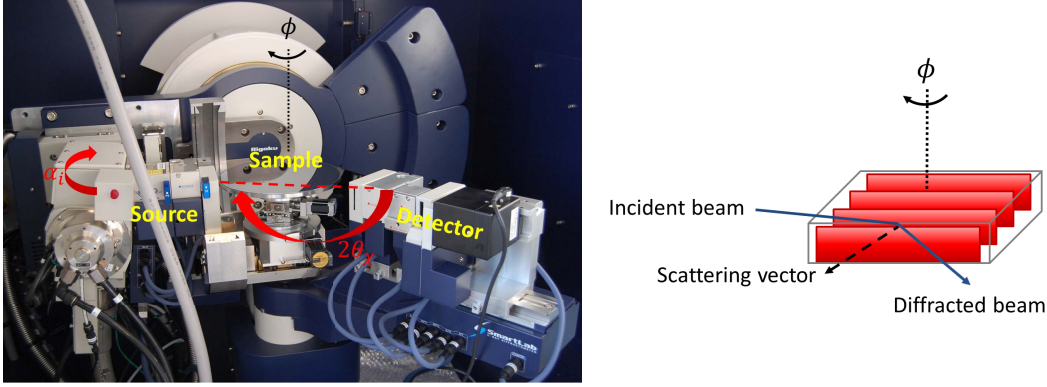


Figure 3.4: Rigaku SmartLab diffractometer in in-plane configuration during a $2\theta_\chi$ scan (left). Sketch of a $2\theta_\chi$ scan including the measured lattice planes (right) [69].

By changing α_i a depth sensitive measurement of the lattice parameter can be obtained taking into account the refractive index n for X-rays

$$n = 1 - \delta - i\beta . \quad (3.10)$$

The values of δ and β are defined by the atomic form factor f_n (see [67]) and range for δ from $\approx 10^{-5}$ to 10^{-6} and for β from $\approx 10^{-6}$ to 10^{-8} (strongly depending on the material), respectively. The penetration depth z_{tot} of smooth planar surfaces depends on the absorption coefficient μ according to [68], [67]

$$z_{tot} = \frac{1}{\sqrt{2} \cdot \frac{2\pi}{\lambda} \cdot \left[\sqrt{(\theta_c^2 - \alpha_i^2) + 4\beta^2} + \theta_c^2 - \alpha_i^2 \right]^{1/2}} \quad (3.11)$$

with $\beta = \frac{\lambda}{4\pi} \mu$.

The critical angle θ_c is determined by δ

$$\theta_c = \sqrt{2\delta} \quad (3.12)$$

Using Eq. 3.12 the critical angle of $\theta_c(Si) = 0.223^\circ$ and $\theta_c(Ge) = 0.31^\circ$ can be calculated. Fig. 3.5 shows the dependence of the penetration depth for Cu K_{α_1} radiation into Si or Ge on the incident angle α_i .

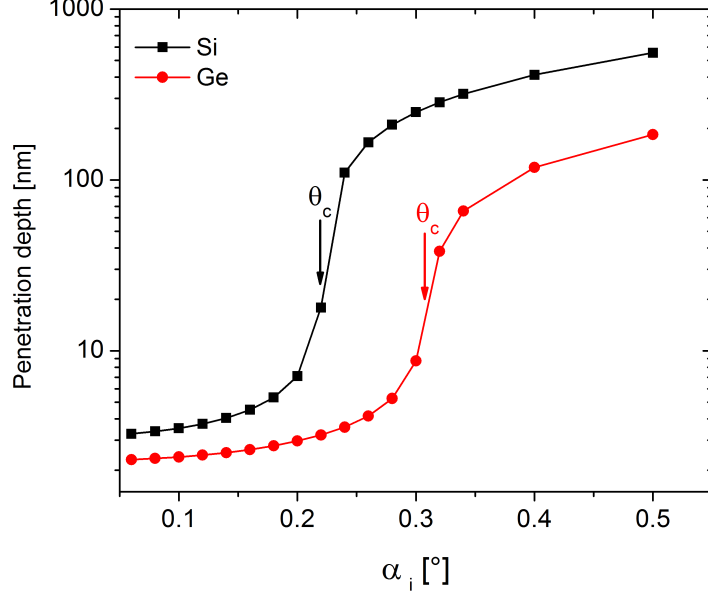


Figure 3.5: Penetration depth of Cu K_{α_1} radiation into a smooth planar Si (black graph) and Ge (red graph) crystal as a function of the incident angles α_i . Here, the critical angles of $\theta_c(Si) = 0.223^\circ$ and $\theta_c(Ge) = 0.31^\circ$ are indicated with black and red arrows, respectively.

In case of a smooth Si or Ge film, the Cu K_{α_1} radiation is propagating as an evanescent wave parallel to the film surface at $\alpha_i < \theta_c$. Hence, the penetration depth of the X-ray beam is very shallow, i.e. in the range of 2-3 nm. It is clearly visible that the Cu K_{α_1} radiation penetrates much deeper into Si than into Ge due to the smaller absorption coefficient μ of Si ($\approx 140 \text{ cm}^{-1}$) compared to Ge ($\approx 372 \text{ cm}^{-1}$) [68]. Beyond θ_c the penetration depth increases dramatically and is at $\alpha_i \gg \theta_c$ dominated by the geometry of the X-ray path.

Finally to determine the exact composition of $Ge_{1-x}Sn_x$, Vegard's law is applied assuming a linear increase of the lattice parameter by the incorporation of Sn. Hereby, the lattice parameter of Ge $a_{Ge} = 5.658 \text{ \AA}$ and α -Sn $a_{Sn} = 6.491 \text{ \AA}$ are taken into account [70]

$$a_{GeSn} = a_{Ge} \cdot (1 - x_{Sn}) + a_{Sn} \cdot x_{Sn}. \quad (3.13)$$

Using Vegard's law (Eq. 3.13) is widely accepted for the determination of Sn contents < 10 at. %, while there are indications for a non-linear increase of the lattice parameter by the incorporation of higher Sn concentrations [71].

The composition of a binary $Si_{1-x}Ge_x$ alloy is calculated using a non-linear function [72]

$$a_{SiGe} = a_{Si} \left(1 + 0.0367x + 0.00501x^2 \right). \quad (3.14)$$

Besides the chemical composition, it is possible to assess the nano-island dimension L (height or diameter) by analyzing the Full Width at Half Maximum (FWHM) $\beta_{is.}$ of the diffraction signal at 2θ according to the Scherrer equation

$$L = \frac{K_S \lambda}{\beta_{is.} \cos(\theta)}. \quad (3.15)$$

K_S is the Scherrer constant and depends on the shape of the crystallites. The value of K_S differs between 1.0 and 1.4, whether the crystals exhibit a cubic or tetrahedral shape.

In this thesis, XRD measurements were used to determine the actual composition of GeSn nanostructures on patterned Si(001) substrates. Furthermore, the strain distribution of the deposited material and the degree of Si interdiffusion into the nano-dots were investigated. Nano-islands exhibit no smooth surface and thus, the propagation of an evanescent wave occurs only in small parts of the nano-dots. Therefore, the penetration depth depends on the geometry of the nanostructures and can be roughly estimated according to the film case at $\alpha_i > \theta_c$, i.e. at small α_i the diffraction pattern is caused by the GeSn nano-dots, while at larger α_i the lattice parameter of the Si nano-pillar substrate can be measured as well. It is also important to keep in mind the limits of XRD characterization. In case of a ternary alloy $Si_{1-x-y}Ge_xSn_y$, it is not possible to determine the chemical composition due to the compensation of the incorporation of Sn by smaller Si atoms. Consequently, it is important to compare the XRD results with other characterization techniques like Energy Dispersive X-ray Spectroscopy (EDX) to obtain a comprehensive understanding of the material system.

3.2.2 Transmission electron microscopy

In contrast to SEM characterization, in Transmission Electron Microscopy (TEM) electrons are detected after penetration *through* the sample (specimen). Thus, the sample preparation includes the fabrication of thin lamellas (typically ≈ 100 nm thickness) using a Focused Ion Beam (FIB) system or mechanical grinding and polishing followed by an argon (Ar) ion milling process. Fig. 3.6 shows a schematic set up of a TEM with a variety of detectors. To achieve a lateral resolution in the sub-nm region electrons are

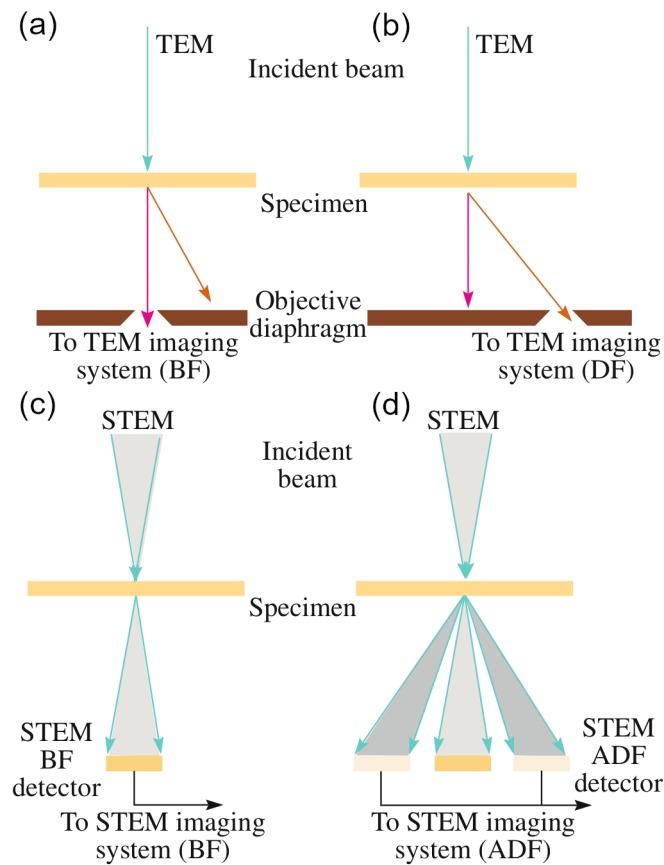


Figure 3.6: Scheme of different detection modes in TEM selecting (a) unscattered electrons or (b) scattered electrons to gain bright field (BF) and dark field (DF) images, respectively. In STEM mode (c) bright field (BF) detectors (analyzing unscattered electrons) and (d) annular dark field (ADF) detectors (detecting scattered electrons) are used [73].

accelerated by 80 keV to 300 keV and focused by condenser lenses. When the electron beam hits the specimen the electrons either (i) go through the sample without any interaction (transmitted beam), (ii) are scattered elastically (diffracted electrons) or (iii) are scattered inelastically. (ii) the diffracted electrons can be used for electron diffraction pattern to analyze the lattice structure. (iii) the emission of characteristic X-rays can be analyzed by so called Energy Dispersive X-ray Spectroscopy (EDS) or EDX, to investigate the chemical composition of the specimen. (ii) the elastically and (iii) inelastically scattered electron beams penetrating through the sample, pass the objective lenses, and are visualized in a imaging system by a photo-active film, a phosphor screen or a Charge Coupled Device (CCD) camera. (ii) the constructive and destructive interference of the transmitted beam with the phase of the diffracted electrons is used in High-Resolution Electron Microscopy (HRTEM) to record a phase-contrast image of the atoms considering the transmitted (un-diffracted) electrons or scattered electrons forming Bright Field (BF) or Dark Field (DF) images, respectively. (ii) elastic and (iii) inelastically scattered electrons are analyzed in Scanning Transmission Electron Microscopy (STEM) mode by a narrow focused electron beam ($\approx 1 - 10 \text{ \AA}$) monitoring the specimen in a raster like manner. Similar to BF images can be obtained by selecting the un-scattered electrons. The so called Annular Dark-Field imaging (ADF) detector collects low-angle diffracted or inelastically scattered electrons. Nowadays, High-Angle Annular Dark-Field imaging (HAADF) detectors are used, collecting the inelastic scattered electrons at an acceptance angle greater than 50 mrad ($\approx 3^\circ$). Furthermore, the mapping of the sample by STEM is coupled with the detection of X-rays, achieving a point-by-point mapping of the chemical composition of the specimen. Additionally, the energy losses of the electrons can be used in Electron Energy-Loss Spectrometry (EELS) to further analyze the lattice and elemental distribution.

In this thesis all TEM analyses were carried out by a FEI Tecnai Osiris TEM operating at 200 kV. The cross section images are recorded in HRTEM mode, while HAADF and BF images visualize the existence of TDs and MDs which are maybe difficult to identify in a HRTEM image. The TEM at IHP is

equipped with an EDX detector, allowing to map the chemical composition within the nano-island. Note, that point defects can not be observed in cross section images, i.e. to identify 0 dimensional defects plane view images have to be recorded. However, this measurement configuration has the disadvantage of cross contamination such as iron (Fe) during thinning of the specimen, falsifying the EDX analyses of the sample. Another challenge is the quantification of defects due to the bending of the thin lamellas during preparation causing dark contrasts in the HRTEM without the presence of defects. During the preparation of the GeSn lamella the temperatures of the process steps were kept < 200 °C, preventing Sn segregation. In summary, TEM is a very good choice to locally analyze the lattice properties as well as chemical distribution across the nano-dots. Again, important is the combination of different characterization techniques e.g. TEM together with XRD to gain a comprehensive understanding of the nano-dots. While by TEM the properties of single islands can be analyzed, with XRD one can investigate many islands giving the average lattice configuration and Sn content.

3.3 Optoelectronic characterization methods

This section describes the characterization techniques to evaluate the optical properties of the different GeSn alloys. The change of the bandgap and its temperature dependent behavior is monitored using photoluminescence spectroscopy by excitation of electron–hole pairs with an energy larger than the bandgap. Finally, Ge and GeSn nano–islands are contacted and the generation of a photocurrent is analyzed.

3.3.1 Photoluminescence

Theoretical background

Optical transition

In thermal equilibrium the rates of generation G_0 and recombination R in a semiconductor are equal, considering the carrier concentration n_0 and p_0 as follows

$$G_0 = Bn_0p_0 . \quad (3.16)$$

The parameter B [cm^3/s] is a material constant depending on the composition, defects, temperature and doping. Exposing a semiconductor to light generates additional electron–hole–pairs at a rate R_{ex} and consequently, G_0 and R are not longer equal. Due to the external injection mechanism the carrier concentrations are $n = n_0 + \Delta n$ and $p = p_0 + \Delta p$, respectively, considering that the excess electron and holes $\Delta n = \Delta p$ recombine in pairs the recombination R rate can be defined as follows

$$R = G_0 + R_{ex} = Bnp . \quad (3.17)$$

Taking into account G_0 in Eq. 3.16, R_{ex} is defined as follows

$$R_{ex} = R - G_0 = Bnp - Bn_0p_0 = B[(n_0 + \Delta n)(p_0 + \Delta p) - n_0p_0] . \quad (3.18)$$

In case of small neutral excitation, $\Delta n = \Delta p \ll n_0, p_0$ and hence $R_{ex} \approx Bn^2$. Fig. 3.7 depicts different pathways of recombination in a semiconductor. The

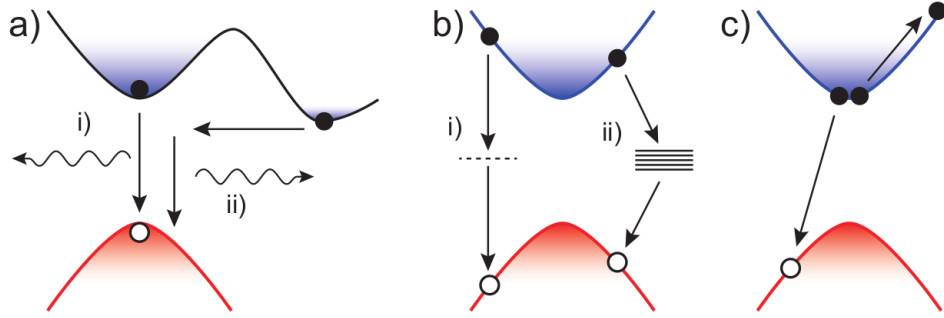


Figure 3.7: Optical transition of a) radiative transition in i) direct and ii) indirect semiconductors as well as b) non-radiative recombination across i) trap and ii) surface states. c) Auger recombination by emission of an electron [21].

most efficient radiative recombination is the decay of the electron from the conduction into the valence band at the Γ -point in a direct transition (see Fig. 3.7 ai), which is desired for light emission devices such as lasers. Because of the conservation of momentum, the optical transition between the valence and conduction band only happens at the same point of the Brillouin zone. Therefore for the energy conservation, indirect transitions (see Fig. 3.7 aii) involve the presence of a quasi-particle (phonon) and are calculated at second order perturbation theory being proportional to the reciprocal of square energy of the photon and for this reason less efficient. Moreover, where a phonon assisted radiative recombination of electron-hole pairs is observed, also the probability of an optical transition is reduced.

Furthermore, non-radiative recombination paths exists, e.g. in presence of defects causing discrete energy levels within the band gap (see Fig. 3.7 bi). Electrons are trapped in vacancies or defect states and can recombine in a non-radiative manner with holes at this forbidden energy levels, which is called Shockley-Read-Hall (SRH) recombination. The rate of recombination in a SRH process R_{SRH} is defined as follows considering the intrinsic carrier

concentration n_i

$$R_{SRH} = \frac{np - n_i^2}{\tau_p(n + n_1) + \tau_n(p + p_1)} . \quad (3.19)$$

The parameter n_1 (p_1) is comparable to an electron (hole) concentration that would be located in the conduction (valence) band, if the trap energy is equal to the Fermi energy [74]. The lifetime of electrons τ_n is assumed when the centers are completely empty, while the lifetime of holes τ_p is valid when all centers are occupied by electrons. In case of a high level of injection $n = p \gg n_i, n_1, p_1$ and hence a linear relation is assumed between the carrier concentration and recombination rate as follows

$$R_{SRH} \approx \frac{n}{\tau_n + \tau_p} = An . \quad (3.20)$$

Similar to these defect states, continuum energy levels arise from additional surface states within the band gap due to dangling bonds or surface reconstruction breaking the bulk crystal periodicity (see Fig. 3.7 bii). These surface states can be suppressed by formation of a proper surface passivation, i.e. terminating the surface by hydrogen Ding et al. [75].

Finally, Fig. 3.7 c illustrates a three particle process, in which the energy from the electron–hole recombination is transferred to an electron from the conduction band. The phonon assisted relaxation of this electron back to the conduction band edge is again a non-radiative process. This so called AUGER recombination is dominant in heavily doped semiconductors. The recombination rate through a AUGER recombination is defined as follows

$$R_{Auger} = C_n n (np - n_0^2) + C_p p (np - n_0^2) . \quad (3.21)$$

In case of a high level of external injection $\Delta n = \Delta p \gg n_0$ the recombination rate can be assumed as

$$R_{Auger} = (C_n + C_p) n^3 = C n^3 . \quad (3.22)$$

The recombination $R(\Delta n)$ of all processes including radiative and non-radiative one, depends on the amount of excess carrier Δn as well as the carrier lifetime τ and can be summarized considering the approximations mentioned above as follows

$$R(\Delta n) = A\Delta n + B\Delta n^2 + C\Delta n^3 = \frac{\Delta n}{\tau}. \quad (3.23)$$

It is obvious that non-radiative recombination A , the spontaneous radiative recombination B and non-radiative AUGER recombination C are competing processes and thus, the material system has to be optimized to increase B for enhanced light emission.

Direct transition

The spectral intensity of the emitted light is proportional to the recombination rate for the spontaneous emission, that in quantum mechanics is based on the Fermi golden rule [76]. The Fermi golden rule

$$P_{i \rightarrow f} = \frac{2\pi}{\hbar} \cdot |\langle f|H|i \rangle|^2 \delta(E_f - E_i - \hbar\omega) \quad (3.24)$$

calculates the number of transitions per unit of time between an initial state i and a final state f at an energy distance $\hbar\omega$ and with an interaction hamiltonian H . In the case that will be under investigation, initial and final states are respectively in conduction and valence band at Γ point. The theoretical assumptions are given by

- (i) the conservation of the energy between the initial and final state ($\delta(E_f - E_i - \hbar\omega)$),
- (ii) the conservation of momentum (explained in the vertical transition between the valence and conduction band),
- (iii) the assumption that the initial state needs to be occupied, while the final state needs to be vacant and
- (iv) the sum of all the possible k of the first Brillouin zone.

Taking into account assumption (iii) we can conclude that the recombination rate is proportional to $\exp^{-\frac{E-E_g}{kT}}$ according to assumption (iii) and to the joint density of states from assumption (iv). Considering a direct transition, the energy of an electron in the conduction band $E_c(k)$ is defined as follows [77]

$$E_c(k) = E_g + \frac{\hbar^2 k^2}{2m_c} . \quad (3.25)$$

The energy of an electron depends on the bandgap E_g at the Γ point, the mass of the electron in the conduction band m_c , the wave vector k and the reduced Planck constant \hbar . The energy of a hole in the valence band depends on the mass m_v

$$E_v(k) = -\frac{\hbar^2 k^2}{2m_v} . \quad (3.26)$$

The energy of an emitted photon is given by the difference between the energy of the electron and the energy of the hole as follows

$$\hbar\omega = E_c(k) - E_v(k) = E_g + \frac{\hbar^2 k^2}{2m_r^*} . \quad (3.27)$$

The reduced effective mass m_r^* is defined as follows

$$\frac{1}{m_r^*} = \frac{1}{m_c} + \frac{1}{m_v} . \quad (3.28)$$

The joint density of states for parabolic bands $J(E)$ depends on m_r^* , the energy of the emitted photon $\hbar\omega$ as follows

$$J(E) = \frac{(2m_r^*)^{\frac{3}{2}}}{2\pi^2 \hbar^3} \sqrt{\hbar\omega - E_g} . \quad (3.29)$$

The distribution of the carriers $F(E)$ is determined by the Boltzmann distribution

$$F(E) = \exp\left(-\frac{E}{k_B T}\right) \quad (3.30)$$

Hence, the Photoluminescence (PL) intensity for a direct band-to-band transition is proportional to the product the joint density of states and the Boltzmann distribution of the carriers defined in Eq. 3.29 and Eq. 3.30, respec-

tively,

$$I(\hbar\omega) \propto \sqrt{\hbar\omega - E_g} \cdot \exp^{-\frac{E-E_g}{k_B T}}. \quad (3.31)$$

A typical PL peak shape is shown in Fig. 3.8. The low energy border PL

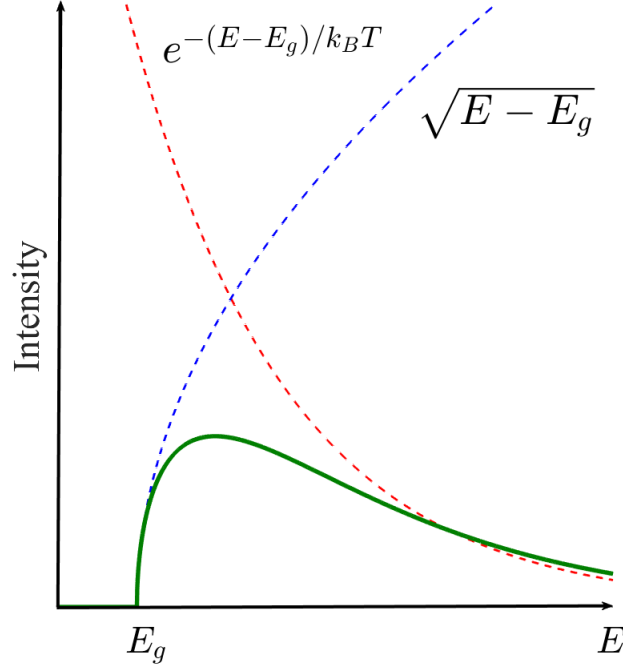


Figure 3.8: PL peak shape defined by a sharp rise at the low energy border according to $\sqrt{E - E_g}$ and slowly decreasing tail considering the Boltzmann distribution $\exp^{-\frac{E-E_g}{k_B T}}$ [78].

peak is characterized by a sharp rise due to the factor $\sqrt{\hbar\omega - E_g}$ considering the energy of the emitted photons $E = \hbar\omega$ and the direct bandgap energy E_g . The tail towards higher energy depends on the Boltzmann distribution $\exp^{-\frac{E-E_g}{k_B T}}$ describing the occupation of density of states. Here, the thermal energy $k_B T$ is important defined by the Boltzmann constant k and the temperature of the excited carrier at the Γ point T . Note, that the bandgap energy E_g depends also on the lattice temperature as follows [79]

$$E_g = E_0 - \frac{\alpha T^2}{T + \beta}. \quad (3.32)$$

The bandgap E_g depends on the bandgap energy at 0 K E_0 , and on the ma-

terial constants α and β . The Varshni relation [79] predicts a red shift of E_g with increasing T due to temperature dependent electron–lattice interactions.

Experimental set up

The experimental set up for the PL measurements is shown in Fig. 3.9. The laser beam (532 nm) was focused on the sample with a 50x objective

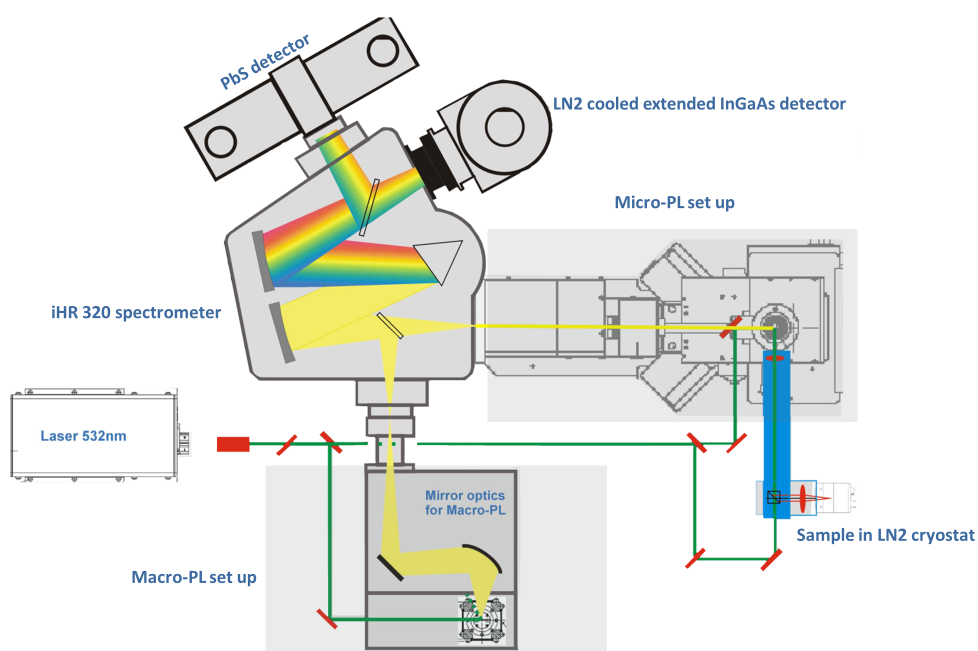


Figure 3.9: Sketch of the PL set up using a green laser (532 nm) for excitation. In this thesis only μ -PL measurements were acquired.

with a aperture of 0.65 exhibiting a spot size of $< 1 \mu\text{m}$. The PL was measured in backscattering geometry, where the beam was dispersed by a iHR 320 Horiba Jobin-Yvon spectrometer. The emitted photons were analyzed by either (a) extended InGaAs detector array or (b) single channel PbS detector with the wavelength λ cut off at (a) 2000 nm and (b) 3500 nm, respectively. The collected PL emission of the sample is scaled to 2 mm by an entrance slit in front of the grating monochromator with gratings of 300 and 600 lines/mm, respectively. It is also possible to selectively filter the signal

after the monochromator to suppress strong laser light, which hides the luminescence of the sample. Moreover, the sample can be cooled with liquid nitrogen (LN2) down to 80 K and heated up to 570 K in nitrogen atmosphere with a Linkam temperature control system. The position of the laser light on the sample surface can be monitored with a microscope, which is important to control the sample shift during temperature depend PL measurements. The heating of the sample during PL characterization is crucial, since GeSn alloys are thermally instable leading to phase separation and the formation of pure Ge and β -Sn segregates. Thus, the power density PD of the laser hitting the sample surface has to be considered carefully. The laser power reaching the sample surface P_m is measured after a 50x objective with a Thorlabs laser power meter. The power density of a circular shaped laser spot of about $1 \mu m$ can be determined as follows

$$PD = \frac{P_m}{\pi \left(\frac{d}{2}\right)^2} \cdot (1 - R) . \quad (3.33)$$

One has to take into account the reflectance R of the semiconductor at a certain wavelength. Fig. 3.10 depicts the laser power P_m measured after the objective as a function of the nominal power of the laser. To give an example for Ge in air with a reflectance of about 0.5 at 532 nm (green laser light) [80], a $1 \mu m$ broad laser spot has a power density of about $0.3 MW/cm^2$ using a 50x objective with a nominal laser power of 100 mW.

To avoid the introduction of artifacts, the PL signal of the sample is corrected by the responsivity of the spectrometer. To gain the response function of the spectrometer, a calibration with a black-body lamp was recorded using the same set up parameters as for the PL measurements of the sample including entrance slit, filter, objective and grating.

3.3.2 Photodetection

After the selective MBE growth of high quality GeSn crystals using the approach NHE, the demonstration of the tunability of the bandgap by varying

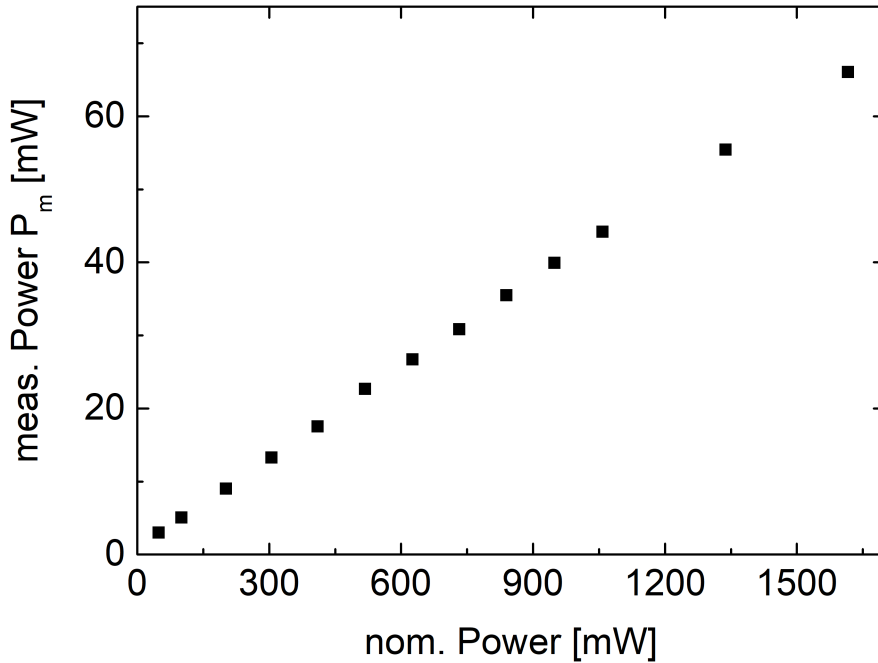


Figure 3.10: Measured laser power P_m as a function of nominal laser power for green laser (532 nm) using a 50x objective.

the Sn content, the final step is the fabrication of a device to demonstrate the utilization of GeSn nano-islands in a future photodetector. This requires contacting with the nano-islands using a contact metal.

The following sections introduce the importance of the choice of semiconductor-metal contact, which strongly influences the measurements of the photocurrent presented later in the results part in section 4.4. Another challenge is to couple the incoming light into the small nanostructures. Structures smaller than half of the incoming wavelength λ exhibit almost no absorption and thus strategies for field amplification such as Localized Surface Plasmons (LSPs) and propagating modes are exploited.

Metal contacts

The fabrication of metal contacts is another key step in production of high performance electronics and optoelectronic devices. Hence, important aspects of a metal–semiconductor junction are discussed, before considering the principles of a photodetector. In Fig. 3.11 the energy band diagrams of a n-doped semiconductor with a smaller electron affinity compared to the work function of the metal are shown before contact and in contact considering an ideal case without surface states and other anomalies. Hereby, the work func-

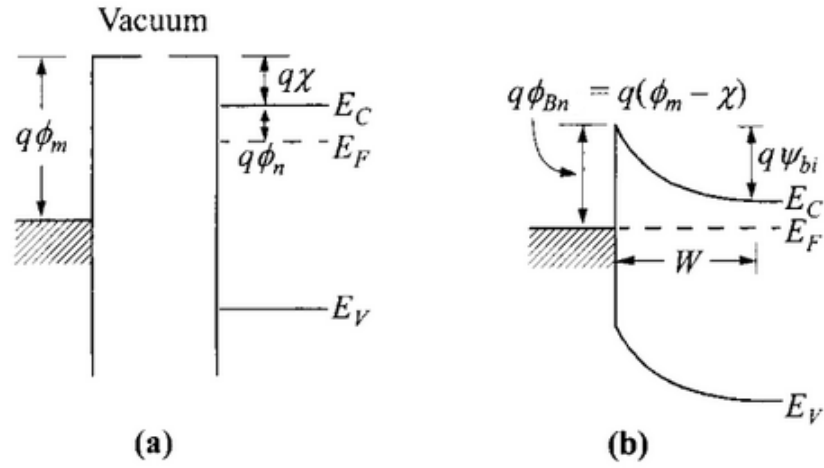


Figure 3.11: Schematic picture of the energy band diagrams of a metal (left) and a n-doped semiconductor (right) (a) before contact and (b) in contact at thermodynamic equilibrium with the built in potential $q\Psi_{bi}$ and the depletion width W . The work function of the metal is larger than the one of the semiconductor [76].

tion (the difference between the vacuum level E_{vac} and the Fermi level E_f) is a key parameter for the properties of a metal-semiconductor contact [76]. The metal work function $q\Phi_m$ is characterized by the electric charge q and the electrostatic potential Φ_m (see fig. 3.11 (a)), while we define the semiconductor work function $q(\chi + \Phi_n)$ as the sum of the electron affinity $q\chi$ (measured from the conduction band E_c to E_{vac}) and $q\Phi_n$ (the energy difference between E_c and E_f). If $q\Phi_m$ of the metal and $q(\chi + \Phi_n)$ of the semiconductor are equal, an ohmic contact can be achieved. However, metal-semiconductor

contacts often show different work functions. In thermal equilibrium the E_f of both the semiconductor and the metal have to align (see fig. 3.11 (b)). Here, the so called Schottky barrier with the height $q\Phi_{Bn}$ is formed, due to the difference between the work function of the metal $q\Phi_m$ and the electron affinity of the semiconductor $q\chi$. In case of a p-type semiconductor the barrier height $q\Phi_{Bnp}$ depends on the bandgap E_g as follows

$$q\Phi_{Bp} = E_g - q(\Phi_m - \chi) . \quad (3.34)$$

Thus, for the sum of the barrier heights on n-type and p-type substrate we obtain

$$q(\Phi_{Bn} + \Phi_{Bp}) = E_g . \quad (3.35)$$

Additionally in thermodynamic equilibrium (without external bias), a region in the semiconductor is formed close to the metal junction, in which the mobile carriers are depleted. This region is called depletion region and exhibits a built in potential $q\Psi_{bi}$ (difference of the Fermi energy between metal and semiconductor), which is important for the operation of photodetector and will be discussed further in the following section *Plasmonic Photodetector*.

An example for tuning the properties of the metal–semiconductor contact is alloying such in case of the GeSn system. As shown in eq. 3.35, the Schottky Barrier Height (SBH) depends in first approximation on the bandgap. By incorporation of Sn into Ge, bandgap narrowing can be observed and thus, a decrease of the SBH is expected. In fact, the SBH of holes can be reduced from about 0.15 to 0.05 eV by an increase of the Sn content from 2 to 10 % in case of NiGeSn-GeSn contacts [81].

Plasmonic Photodetector

The physical principle of a photodetector is called photoelectric effect, i.e. converting optical energy into electrical signals. When the E_{phot} of the absorbed photon is equal to or greater than the bandgap energy, an electron from the valence band is excited to the conduction band leaving a hole in

the valence band behind. The so called inner photoelectric effect, which is responsible for the generation of electron-hole-pairs is used in the photodetector scheme presented in this thesis.

A p-i-n semiconductor can be used as photodetector in reverse bias condition. The p-doped region consists of acceptor dopant atoms (e.g. Boron in Si), which can accept an electron in the valence band. Thus, a hole in the Si valence band is generated as well as a negative charged acceptor atom bound to the crystal lattice. Analogously, the n-doped semiconductor (e.g. Phosphorous doped Si) consists of donor atoms which can transfer an electron from the valence band to a Si atom creating a negatively charged mobile carrier. The positively charged donor atoms in the n-region as well as the negatively charged acceptor atoms in the p-region are immobile. Combining a p-doped semiconductor with a n-doped one, leads to a diffusion of the electrons from the n-region to the p-region, due to the charge carrier gradient, while the holes from the p-region diffuse to the n-region. The charged acceptor and donor atoms are bound to crystal forming a depletion zone causing an electric field which induces a drift current in the opposite direction to the diffusion of the free carrier. After reaching the thermodynamic equilibrium a diffusion voltage or built-in voltage Ψ_{bi} within the depletion zone can be determined as follows

$$\Psi_{bi} = \Psi_t \ln \frac{N_A N_D}{n_i^2} \quad (3.36)$$

$$\text{with } \Psi_t = \frac{kT}{q} . \quad (3.37)$$

The built-in voltage Ψ_{bi} depends on the thermal voltage Ψ_t , the concentration of charged acceptor N_A and donor N_D atoms as well as the intrinsic carrier density n_i (excitation of valence band electrons by thermal energy to the conduction band followed by relaxation). The thermal voltage depends on the Boltzmann constant k , the temperature T and the electron charge q . The width w of the depletion zone is important for the photon absorption, because the majority of the generated electron-hole-pairs are separated in this region to the n- and p-side, due to the internal electric field. The drift of the separated carriers causes a photocurrent. The width w depends on

the external bias U_{PN} , the dielectric constant of the vacuum ϵ_0 and the permittivity of the investigated material ϵ_r as follows

$$w = \sqrt{\frac{2\epsilon_0\epsilon_r}{q} \left(\frac{1}{N_A} + \frac{1}{N_D} \right) (\Psi_{bi} - U_{PN})} . \quad (3.38)$$

Decreasing the doping of the semiconductor increases the width of the depletion zone w . Additionally, applying a negative bias at the p-region side, i.e. inducing reverse bias conditions, leads also to an increased depletion width. To further increase w of the depletion zone, an additional layer of undoped semiconductor can be introduced between p- and n-region increasing the probability of photon absorption and forming a p-i-n photodetector [82].

As mentioned above the utilization of nanostructures in subwavelength-sized photodetectors strongly benefits from a field enhancement by plasmons excited in metallic nanostructures. The oscillating mode of electrons at a metal-dielectric interface is known as surface plasmons, the collective oscillation of electrons in a metallic nanostructure are known as LSPs. Such kind of plasmonic excitations can enhance the local electro-magnetic field and, as a consequence, photon absorption, by two to five orders of magnitude, enabling the utilization of nanostructures in a photodetector. Here, we will briefly discuss the effects that can be expected to play a role in subwavelength-size semiconductor structures combined with metallic nanostructures: (i) Leaky Mode Resonances (LMRs) in the nanometer-sized semiconductor structures and (ii) LSPs in metallic nanostructures adjacent to the semiconductor for the field enhancement of the incoming wave.

(i) LMRs of a subwavelength, high refractive index semiconductor nanostructures are discrete modes with propagating electromagnetic fields outside the nano-islands, due to their small size the resonant modes become leaky and enable an efficient interaction with the surrounding. The derivation of leaky modes in a spherical 0D nano-particle with radius r is carried out by solving the Maxwell's equation for the relevant boundary conditions with the following resulting equations, whose discrete solutions correspond to the

resonances that can be excited [83]:

$$\text{TM modes: } n \frac{\psi_m(nkr)}{\psi'_m(nkr)} = \frac{\xi_m(kr)}{\xi'_m(kr)} \quad (3.39)$$

$$\text{TE modes: } \frac{\psi_m(nkr)}{\psi'_m(nkr)} = n \frac{\xi_m(kr)}{\xi'_m(kr)} \quad (3.40)$$

The LMRs depend on the refractive index n of the material, the wave vector k in free space ($k = 2\pi/\lambda$), the radius r , m th order Ricatti–Bessel functions $\psi_m()$ and $\xi_m()$, which are related to the spherical Bessel functions $j_m()$ and spherical Hankel function $h_m()$. Transverse Electric (TE) (Transverse Magnetic (TM)) polarization is defined for the 0D particle case as no electric (magnetic) field in radial direction.

From the specific solutions of the Maxwell's equations follows that the nanostructures can support a limited number of TE and TM LMRs, i.e. the nanostructures exhibit only at specific wavelength λ a resonance for excitation of LMRs. These number is increasing with increasing radius r of the nano-particle. A detailed insight of the theory of LMRs can be found in reference [83] and [84].

(ii) To excite LSPs, free electron charges on metallic nanoparticles/nano-antennas have to respond to external electromagnetic fields and oscillate at resonance wavelengths. LSPs strongly depend on the optical properties of metallic nanoparticles, which are described by a complex dielectric constant $\epsilon(\omega)$ at a frequency ω and the complex refractive index $m = \sqrt{\epsilon}$ depending on the real part of the refractive index n and the absorption coefficient k as follows

$$\epsilon(\omega) = \epsilon_r(\omega) + i\epsilon_i(\omega) \quad (3.41)$$

and

$$m = n + ik . \quad (3.42)$$

The response of the free electrons in metals can be described by the Drude model taking into account the polarization response from the core electrons (background permittivity) ϵ_b , the plasma frequency ω_p and the Drude relax-

ation rate γ

$$\epsilon(\omega) = \epsilon_b - \frac{\omega_p^2}{\omega^2 + \gamma^2} + i \frac{\omega_p^2}{\omega^2 + \gamma^2} . \quad (3.43)$$

The Drude relaxation rate is responsible for scattering/ohmic losses and scales with the imaginary part of the dielectric function. The plasma frequency ω_p scales directly with ϵ_i and is proportional to the carrier concentration n

$$\omega_p = \sqrt{\frac{ne^2}{\epsilon_0 m}} . \quad (3.44)$$

A plasmonic material exhibits a negative real component of the dielectric constant and a small positive imaginary component of the dielectric constant. A small ϵ_i can be achieved by small γ or decrease of the carrier concentration n .

An exciting approach is the photodetection enhanced by surface plasmons based on a nano-pillar array. Fig. 3.3.2 illustrated the evaporation of gold top contact on InGaAs nano-pillars [85]. In Fig. 3.3.2 (a) self-aligned nanoholes (NH) are realized by metalization of an pillar array under a tiled angle, because of the shadowing effect of the nano-pillars. The periodicity of the subwavelength nanoholes depicted in Fig. 3.3.2 (b) causes a field enhancement by LSPs. The increased absorption in the pillar is illustrated in Fig. 3.3.2 (c) according to full wave finite difference time domain simulations using the software Lumerical. The incoming light is confined into the small nano-pillar due to the gold nano-antenna.

We adapted this approach to our Ge(Sn)-dot array based photodetectors. The results are discussed in section 4.4. To gain the most effective coupling of the incoming light into the nanostructures, both the leaky modes and the near field enhancement by the nano-antennas have to be matched. Therefore, sophisticated simulations are required to find the optimized conditions between the LMRs of the nano-particles and the geometry of the nano-hole antennas. This kind of simulations go beyond the scope of this thesis. Thus, the chosen configurations were experimentally probed for the field enhancement of the GeSn or Ge nano-islands during photo current measurements.

Experimental set up

For coupling the light into the Ge or GeSn nanostructures by LSPs, the samples were contacted at the IHT (Institut für Halbleitertechnik) in Stuttgart and characterized in collaboration with the group of Prof. J. Schulze and Dr. habil. I. A. Fischer. In Fig. 3.13 a sketch of metalized Ge nanostructures is illustrated.

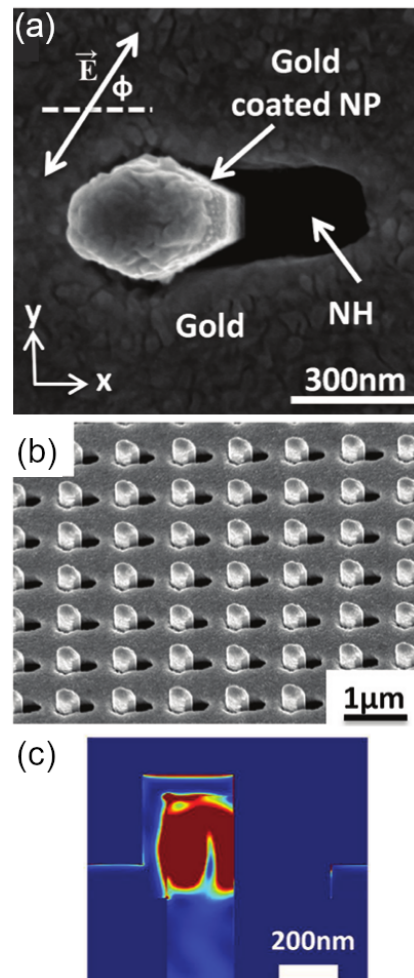


Figure 3.12: SEM images of (a) one nano-pillar (NP) covered with gold (Au) with a self-aligned nanohole (NH) and (b) nanopillar array covered by gold with 1 μm pitch. Spatial power absorption in the InGaAs nano-pillar in the x-z plane simulated by full wave finite difference time domain.

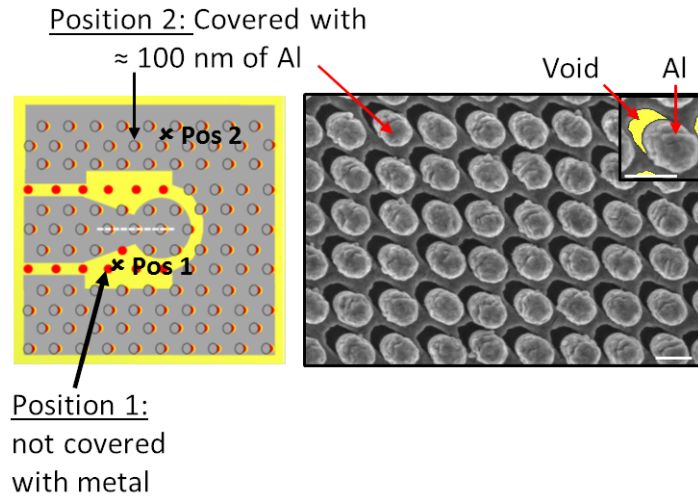


Figure 3.13: left: Top view sketch of sample exhibiting areas with (Pos 2) and without (Pos 1) Al. Right: SEM images of position 2 of Ge nanostructures (200 nm diameter) covered with 100 nm Al. The SEM inset depicts the voids (yellow) between the nanostructures caused by the shadowing effect of the nano-islands. The scale bar of the SEM images is 200 nm.

To form a top contact, the samples were partly covered with photo resist. After optical lithography, Aluminum (Al) was evaporated by an electron beam under an inclined angle of about 30° . The structuring of the Al contact pads was realized by a lift-off process, where the photo resist was removed by acetone.

From Fig. 3.13 (left) it is visible that areas with (position 2) and without (position 1) Al are formed, due to the lift-off process. Furthermore, due to the off-angle deposition of Al, voids are formed depending on the shadowing effect of the islands (see Fig. 3.13 (right)). A magnification of one metalized nanostructure in the inset of Fig. 3.13 (right) depicts these voids (colored yellow), which can act as nano-antennas coupling the incoming electromagnetic wave into the Ge or GeSn nano-islands. To evaporate the top contact at an off-normal angle avoids cost-intensive lithography processes equipping every single nanostructures with a nano-antenna.

Also the backside contact consists of Al, which was used due to its stable oxide, being robust to external influences (see Fig. 3.14). Moreover, Al is a CMOS compatible material, i.e. the fabrication of Al contacts can be in-

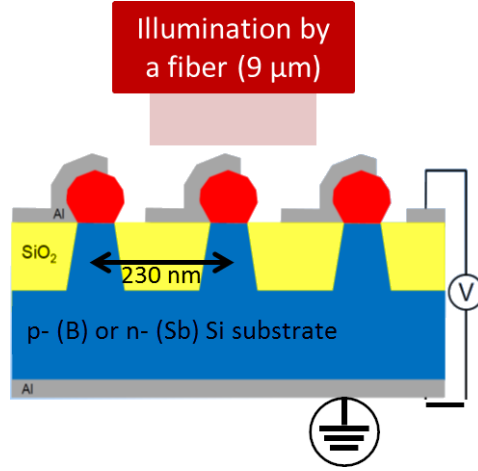


Figure 3.14: Cross section sketch of photocurrent set up, where the samples deposited on either p- or n-doped Si nano-pillars are illuminated by an optical fiber. The nanostructures (red circles) are partly covered with Al, which is used as nanoantenna and backside contact.

egrated in the well established CMOS technology resulting in high volume and low cost device production.

In the photocurrent measurement set up an optical light fiber illuminates the sample in the wavelength region between 650 and 1200 nm (see Fig. 3.14). The step size of changing the wavelength of the illumination was 5 nm and the optical responsivity $R_{opt.}$ was measured according to

$$R_{opt.} = \frac{I(U)_{\lambda,on} - I(U)_{\lambda,off}}{\Phi_{lambda}} . \quad (3.45)$$

A current voltage characteristic is recorded with $(I(U)_{\lambda,on})$ and without $(I(U)_{\lambda,off})$ illumination at 0 V. The optical power output of the fiber Φ_{lambda} has to be considered, therefore the optical power is calibrated with a reference detector (in visible regime Si) with a known optical responsivity. Typically a power of 200 μW is set and the power adjustment to reach 200 μW by the Acoustic Optical Tunable Filter (AOTF) is recorded. Simultaneously, 10 % of the initial power is recorded by an Artifex OPM150 (Optical Power Monitor). During the responsivity measurements 10 % of the initial fiber power is monitored to compensate possible power fluctuations of the fiber.

4 | Results and discussion

4.1 Selective growth of GeSn nanostructures

As aforementioned to exploit the NHE approach, it is necessary to grow GeSn on nano-patterned Si substrates. The substrate used in this thesis comprises Si(001) nano-pillars embedded in SiO₂ grown by CVD. Selective growth means the formation of GeSn crystals on Si seeds, while avoiding nucleation on the SiO₂ matrix. On the one hand studies by Niu et al. [54], revealed that selective growth of Ge on nano-patterned Si substrates requires high temperature (≈ 850 °C) and a low deposition rate (≈ 1.0 nm/min). On the other hand, Taoka et al. [63], demonstrated an enhanced incorporation of Sn into Ge at low temperature growth (200 °C) and high deposition rate (≈ 13 nm/min). Hence, the challenge was to overcome the opposing trends of selective growth and incorporation of Sn.

The results presented in this thesis, focus on the influence of the substrate temperature T_s on the selective growth and the Sn incorporation. Therefore, the Ge deposition rate (5.4 nm/min), the deposition time (20 min) and the Sn cell temperature of 1050 °C aiming for 4 at.% have been kept constant for the most samples to gain an optimum for the selective growth and formation of GeSn alloys. The deviation of the optimized growth parameters will be shown exemplary to demonstrate the influence of the deposition time, deposition rate of Ge and the Sn cell temperature on the selectivity and Sn concentration.

Firstly, the crystal morphology of GeSn and the degree of the selective growth depending on T_s was evaluated by SEM micrographs shown in Fig. 4.1. De-

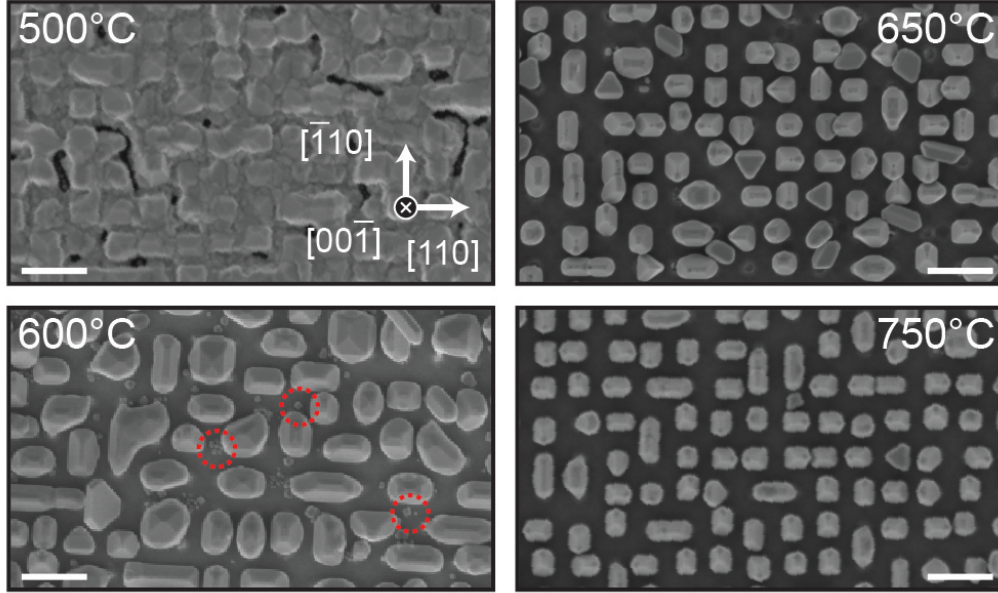


Figure 4.1: SEM micrographs (scale bare 500 nm) after 20 min deposition of Ge (5.4 nm/min) and Sn (1050 °C) at 500 °C, 600 °C, 650 °C and 750 °C. Non-selective GeSn dots on SiO₂ have been labeled exemplarily by dashed red circles [86].

positing at $T_s = 500$ °C yields in a nearly closed layer, while at $T_s \geq 600$ °C nano-islands can be observed as well as small dots on the SiO₂ matrix (indicated by red dashed circles in Fig. 4.1). Increasing T_s to 600 °C, decreases both the coverage despite the same deposition rate in all experiments and the amount of non-selective dots on SiO₂ which are not formed at $T_s = 750$ °C. The reduction of the amount of non-selective islands is in line with the discussion in section 2.3.3, where the density of stable clusters on SiO₂ decreases with increasing T_s . The selective growth is driven by a desorption mechanism, where the arriving adatoms stick on the Si surface (complete condensation regime), while they are desorbing from the SiO₂ matrix (incomplete condensation regime). The independence of the dot density of Ge/SiO₂ from the pitch size investigated by Niu et al. [54], excludes a migration mechanism being responsible for the selective growth.

To grow Ge selectively on Si requires a deposition rate of 1.0 nm/min and

$T_s = 850$ °C, while in this study selective growth is achieved at $T_s = 750$ °C despite the higher growth rate 5.4 nm/min. It seems that in the presence of Sn the Ge adatoms nucleate on Si (while desorbing from SiO_2) at lower temperatures compared to pure Ge, and thus selective growth of GeSn can be realized at low growth temperatures and higher Ge flux. Although no values for E_{des} of Sn/ SiO_2 can be found in literature, Sn adatoms possess a weak interaction with the oxide surface desorbing already at $T_s \approx 580$ °C from SiO_2 [87].

However, the degree of selectivity can not be determined precisely due to coalescence of the islands in all experiments. Reducing the deposition time from 20 to 5 min, offers an easy access to quantify the selectivity. The SEM micrograph of GeSn deposited at $T_s = 600$ °C for 5 min is shown in Fig. 4.2. Without coalescence of the nano-islands it is clearly visible, that

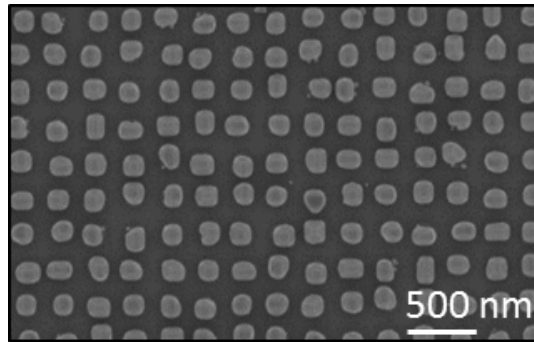


Figure 4.2: SEM micrograph of GeSn nano-dots grown for 5 min at 600 °C with a Ge flux of 5.4 nm/min [86].

only few non-selective GeSn dots can be observed on the SiO_2 matrix. Although depositing at $T_s = 600$ °C does not result in 100 % selective growth of GeSn/Si, the degree of selectivity is in an acceptable range. The impact of the deviation from the selected Ge flux is shown in Fig. 4.3, keeping the other growth parameters constant (deposition time, growth and Sn cell temperature). A deviation from the growth parameters by increasing the Ge flux to 8.5 nm/min results in larger islands due to the higher amount of deposited material and consequently, to coalescence of the islands despite the short deposition time. However, the higher Ge flux results in a lower de-

gree of selectivity compared to the selected growth condition, i.e. a higher amount of non-selective GeSn islands on the SiO₂ can be observed. Evap-

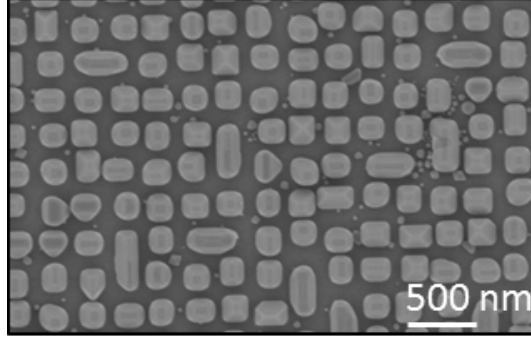


Figure 4.3: SEM micrograph after 5 min deposition with a Ge flux of 8.4 nm/min at 600 °C .

orating Ge with a rate of (5.4 nm/min) together with Sn aiming for 4 at.% Sn in GeSn, requires $T_s \geq 600$ °C for the formation of GeSn nanostructures on Si nano-pillars with a tolerable amount of small GeSn clusters on SiO₂ matrix. As aforementioned little is known about the desorption mechanism of (Ge)Sn. However, studies of Ge on Si(001) by Niu et al [54] have shown, that at $T_s = 750$ °C no stable Ge clusters can be formed on SiO₂. At this deposition conditions, the growth of Ge on the SiO₂ matrix falls in the extreme incomplete condensation regime, in which E_{des} and E_{diff} are very low. To evaluate the amount of incorporated Sn and the presence of Si interdiffusion into the GeSn nano-islands, the larger dots grown at $T_s \geq 600$ °C for 20 min were analyzed by XRD. Fig. 4.4 (a) shows the out-of-plane (left) and in-plane (right) diffraction pattern of the GeSn (004) and (400) reflection, respectively. In all experiments the diffraction peak is observed at lower 2θ angles compared to *bulk* Ge (dashed line). Increasing T_s from 600 to 750 °C increases the 2θ angle from 65.83° to 65.98° in both XRD studies. The island lattice parameter can be determined by the Bragg equation (Eq. 3.9) and is plotted in Fig. 4.4 (b) against T_s . Again, as a reference the lattice parameter of *bulk* Ge is indicated by a black dashed line.

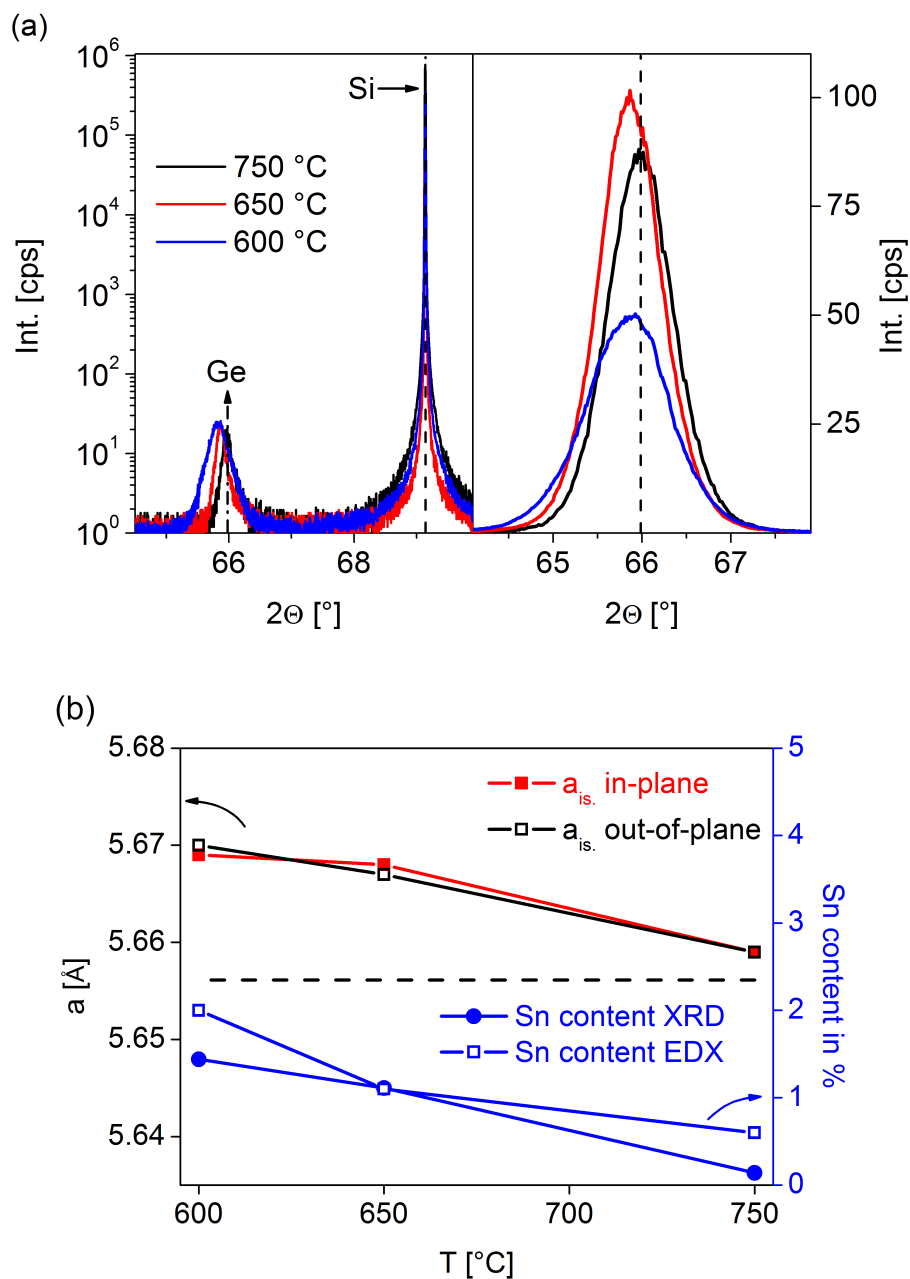


Figure 4.4: (a) Out-of-plane (004) (left) and in-plane (400) (right) diffraction pattern of GeSn nano-islands grown for 20 min at various temperatures. (b) Calculated lattice parameter (black and red squares, left axis) as a function of growth temperature. The lattice parameter of bulk Ge is given as a reference (dashed black line). Sn content of GeSn islands deposited at different temperatures obtained by EDX measurements (blue empty squares, right axis) as well as by XRD using Vegard's law (blue filled circles, right axis) [86].

The lattice parameters obtained from the in- and out-of-plane Bragg diffraction are identical within the measurement error of about $\pm 0.002 \text{ \AA}$. The same in- and out-of-plane lattice parameters indicate that the GeSn nano-islands are not strained, but are fully relaxed. Note, that GeSn layer growth using conventional heteroepitaxy often results in strained layers. Thanks to the NHE approach fully relaxed GeSn nano-dots can be formed. With increasing T_s the lattice parameter is decreasing pointing to the lower incorporation of Sn. The actual Sn concentration in the nanostructures was determined by using Vegard's law (Eq. 3.13) and is plotted as blue graph with filled circles (right axis). A maximum Sn content of about 1.4 at.% was achieved at 600 °C, while almost no Sn ($\ll 1 \text{ at.}\%$) was incorporated in the Ge lattice at 750 °C. Additionally to XRD, EDX measurements have been used to determine the Sn content in the GeSn nanostructures (empty blue squares, right axis). The Sn concentration obtained by XRD and EDX show the same trends. With increasing T_s the Sn content in the GeSn alloy is decreasing. The absolute Sn concentration of both methods differs in the range of the measurement error of 0.5 at.%. Thus both XRD and EDX data confirm a maximum Sn incorporation into Ge of $1.4 \pm 0.5 \text{ at.}\%$ at 600 °C.

Another reason for the decreasing lattice parameter with increasing substrate temperature can be enhanced Si interdiffusion compensating the broadening of lattice by Sn incorporation. Fig. 4.5 shows the STEM images as well as the EDX maps of Ge and Si of the samples grown at 600 °C to 750 °C. At the island/Si interface the region for the Si interdiffusion is highlighted by white frames in Fig. 4.5. It is visible, that the area affected by the Si interdiffusion constitutes only a small fraction of the whole island (approximately 10 %). Hence, the focus of the discussion about the change of the lattice parameter depending on the substrate temperature can be discussed by means of different Sn concentrations only.

To get a profound insight into the crystal properties of the GeSn nano-islands, the growth conditions leading to the highest Sn content were investigated more closely. To compare the influence of a higher Ge flux (8.4 nm/min) on the incorporation of Sn, the nano-islands grown for 5 min

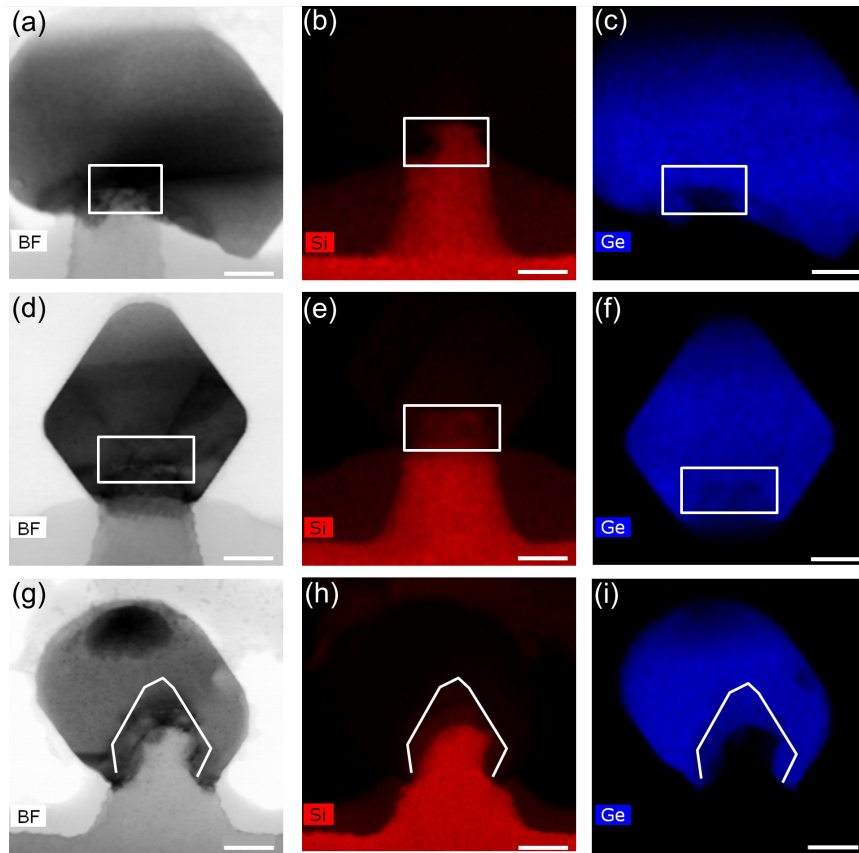


Figure 4.5: (a) STEM BF image, EDX map of (b) Si and (c) Ge after the deposition of GeSn at 600 °C. (d) STEM BF image, EDX map of (e) Si and (f) Ge after the deposition of GeSn at 650 °C. (g) STEM BF image, EDX map of (h) Si and (i) Ge after the deposition of GeSn at 750 °C. The region of Si interdiffusion into the nano-islands is labeled by white frames. The scale bar of all images is 40 nm.

at 600 °C were analyzed further (see Fig. 4.3). Fig. 4.6 depicts in-plane measured $2\theta_\chi - \phi$ scans at different incident angles α_i (as described in section 3.2.1).

In Fig. 4.6 the in-plane (400) diffraction pattern is plotted against the incident angles α_i , giving depth sensitive information about the evolution of the lattice parameter. In Fig. 4.6 (a) the GeSn (400) diffraction peak can be observed at a 2θ value of 65.84° , corresponding to the incorporation of 1.4 ± 0.5 at.% Sn, which is the same Sn content as in case of growth with Ge flux of 5.4 nm/min.

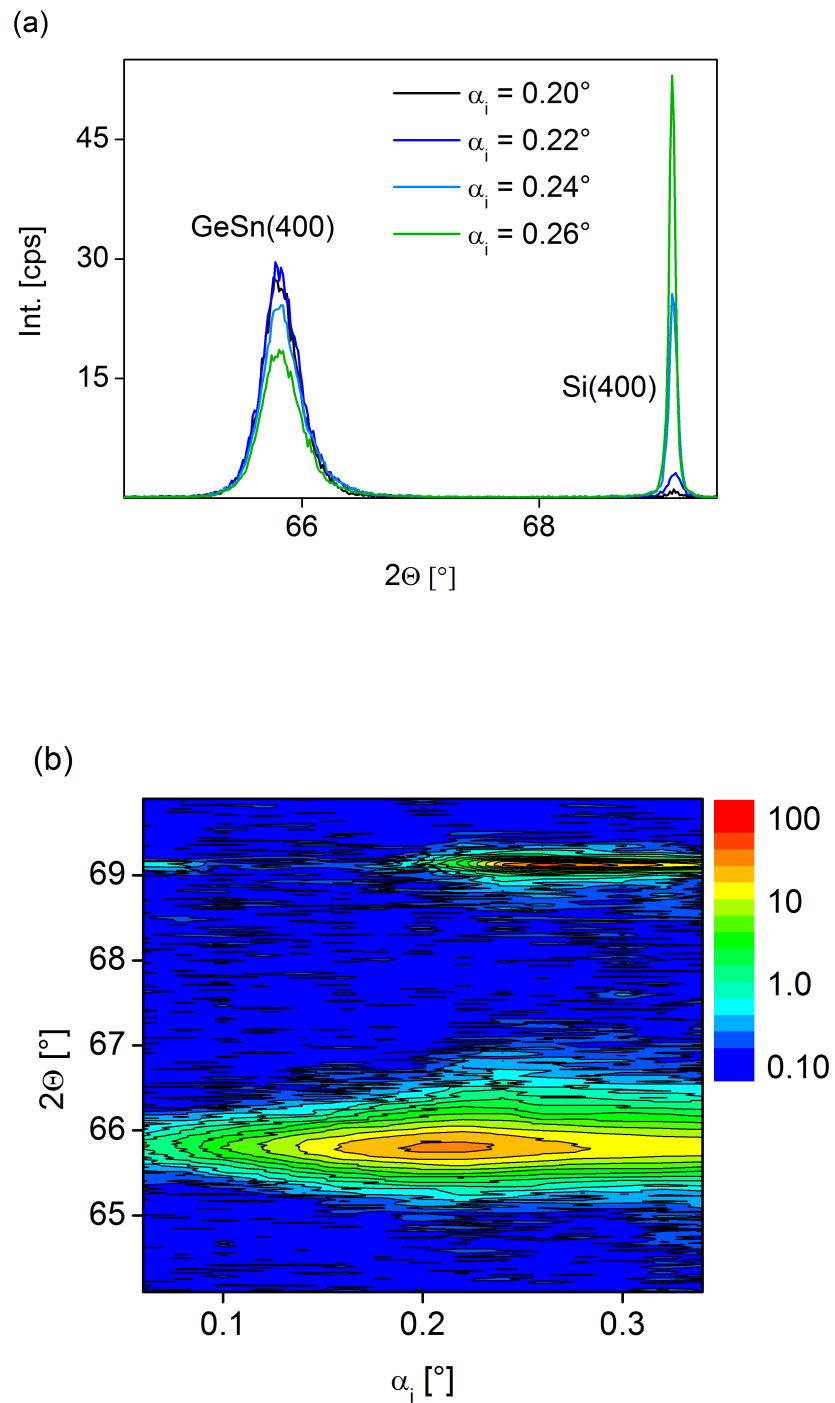


Figure 4.6: Depth sensitive in-plane XRD measurements at various incident angles α_i of GeSn nano-dots grown at 600 °C for 5 min with a Ge flux of 8.4 nm/min. (a) In-plane (400) diffraction pattern at four selected α_i . (b) 2D contour plot of the in-plane (400) reflection of Si and GeSn [86].

Investigations by Taoka et al. [63] suggested an increased Sn concentration caused by an enhanced Ge flux, which was not observed in this study. These results suggest, that in this thesis the increase of the Ge flux was too low to cause a significant reduction of the migration of the Sn atoms. Depositing with a Ge flux of 5.4 nm/min is a good compromise between selective growth and the incorporation of Sn into the Ge lattice.

With increasing α_i the influence of the Si substrate peak is visible because of the higher penetration depth at higher α_i . The FWHM of the Si diffraction signal decreases from 0.1° to 0.05° with increasing α_i . At lower incident angle mainly the top part of the Si nano-pillar is detected, broadening the diffraction signal due to the finite size of Si pillar compared to *bulk* Si substrate dominating at $\alpha_i \geq 0.24^\circ$.

Fig. 4.6 (b) shows the (400) reflection of the Si substrate at $\alpha_i \geq 0.2^\circ$. According to Eq. 3.11 an incident angle of 0.22° corresponds to a penetration depth into Ge of about 3 nm, i.e. according to theory no Si signal can be detected at α_i larger than 0.22° , because the GeSn islands are about 100 nm high. A penetration depth in the range of 100 nm requires an incident angle α_i of about 0.4° using Eq. 3.11. Since, the Si substrate diffraction can be observed at $\alpha_i \ll 0.4^\circ$, the assumption for a smooth planar film is not valid. In case of a surface compromised of nano-dots a linear increase of the penetration depth such as in case for $\alpha_i \gg \theta_c$ has to be assumed which is dominated by the geometry of the X-ray path.

Furthermore, no continuous transition of the intensity from the Si to the GeSn diffraction peak can be observed, i.e. no transition of the lattice parameter from Si to GeSn occurs. These data imply two important aspects of the GeSn growth.

- (i) The presence of the *substrate compliance* effect can not be confirmed and thus, plastic relaxation of the GeSn nano-dots is assumed rather than elastic one. In agreement with the discussion in section 2.3, the required Si seed size for the defect-free growth of GeSn could not be met in the experiment (Si diameter $\ll 40nm$). Nevertheless, the NHE growth is expected to improve the crystal quality by promoting pro-

cesses like gliding out of dislocations from the GeSn nano-islands.

- (ii) No significant interdiffusion of Si into the island can be observed within the detection limit of XRD. NHE growth suppresses the Si interdiffusion caused by the reduced GeSn/Si interface area compared to conventional planar heteroepitaxy. The Si interdiffusion is caused by surface diffusion as suggested in calculations by Georgiou et al. [45]. The interface of the NHE crystals is much smaller compared with the island volume and consequently, the Si interdiffusion becomes negligible small.

Fig. 4.7 shows an in-plane Reciprocal Space Map (RSM) in angular coordinates for better discussion of the twist angle. The (400) diffraction signal is

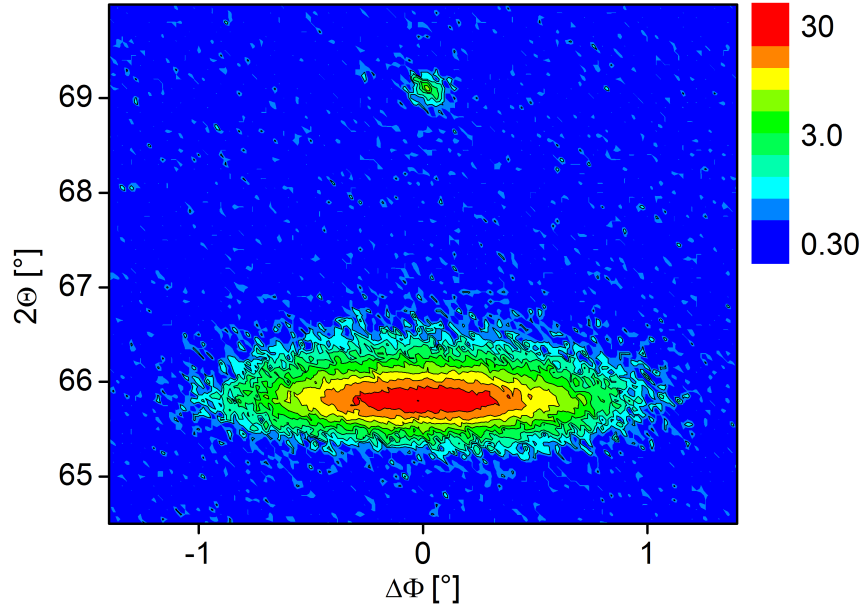


Figure 4.7: In-plane RSM at an incident angle $\alpha_i = 0.22^\circ$ of GeSn nano-islands grown at 600°C for 5 min with a Ge flux of 8.4 nm/min [86].

plotted against $\Delta\Phi$, i.e. the rotation around the sample surface normal. The FWHM of the reflection peak $\beta_{total} = 0.88^\circ$ depends on

- (i) the resolution of the diffractometer which can be estimated from the FWHM of perfect crystalline Si substrate diffraction peak. The FWHM β_{diff} of the Si (400) diffraction is about 0.05° .

- (ii) The broadening of the GeSn (400) diffraction peak because of the finite size of the nano-islands can be determined by Eq. 3.15 taking into account the wavelength of the $CuK_{\alpha 1}$ radiation. With an in-plane measurement the in-plane dimension of the island (width in x-direction) can be assessed. Assuming a diameter of 155 nm of the GeSn nano-islands from the SEM images, the influence of the crystallite results in a $\beta_{is.}$ broadening of about 0.08° .
- (iii) Finally, the FWHM of the diffraction peak depends on the deviation of the in-plane lattice planes, i.e. the twist angle. Assuming a Gaussian contribution of all three components, forming in convolution the measured FWHM of the diffraction peak, the twist angle β_{twist} can be calculated according to

$$\beta_{twist} = \sqrt{(\beta_{total})^2 - (\beta_{diff})^2 - (\beta_{is.})^2} . \quad (4.1)$$

Using Eq. 4.1 a twist angle of the GeSn nano-islands of about 0.87° can be determined.

The discussion above confirms a small contribution of XRD instrument as well as crystal size on the FWHM. Hence, the broadening of the (400) diffraction peak is caused by the deviation of the in-plane lattice planes from the lattice of the Si substrate. The GeSn (400) reflection points to a symmetric mosaicity of the nano-islands with an average twist angle of about 0.87° .

The NHE growth at $600 - 650^\circ\text{C}$ of GeSn results in the successful incorporation of Sn into the Ge lattice above the solubility limit. Despite the high growth temperature, Si interdiffusion from the substrate into the nano-islands was suppressed. However, the formation of a defect rich island/substrate interface is assumed, because no strain partitioning between the Si nano-pillars and the GeSn nanostructures was observed. TEM measurements were performed to characterize the crystallinity of the nano-islands and the substrate/island interface. Fig. 4.8 shows the TEM micrographs of the GeSn nanostructures grown at 600°C for 20 min. The islands'

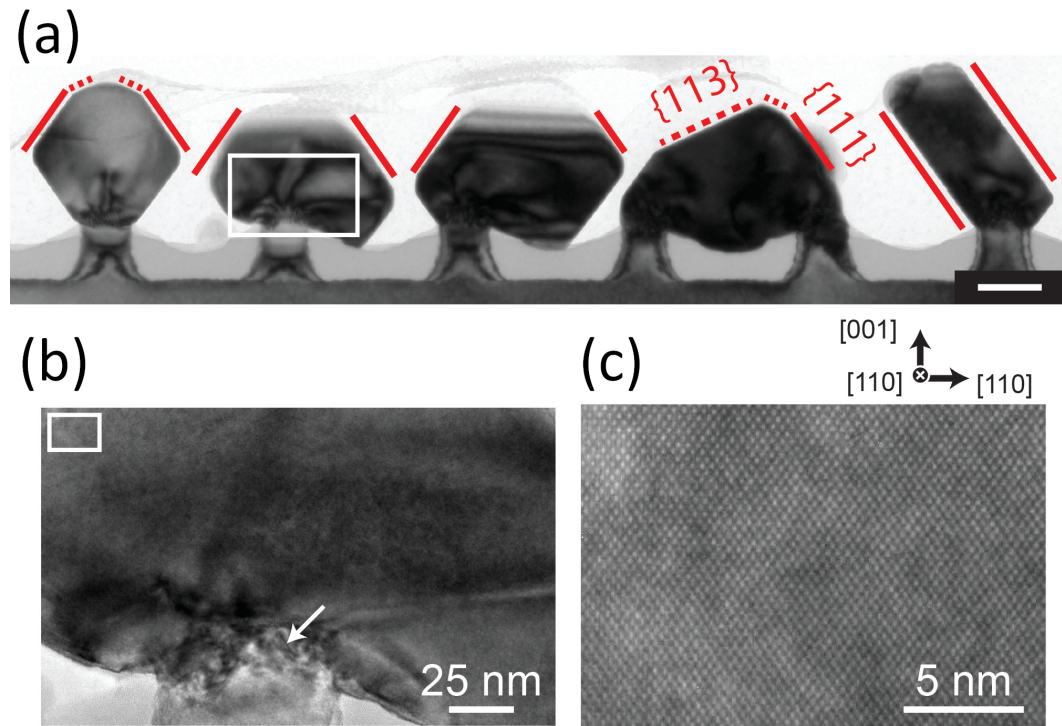


Figure 4.8: TEM micrographs of GeSn nanostructures grown at 600°C for 20 min. Overview of $\{111\}$ (solid red line) and $\{113\}$ (dashed red line) faceted nano-islands (scale bar 100 nm). (b) and (c) Magnified TEM images indicated by white square in (a) and (b) showing (b) dislocations/stacking faults at the island/substrate interface and (c) defect-free island [86].

morphology (Fig. 4.8 (a)) is dominated by $\{111\}$ facet growth (red lines), while only few $\{113\}$ facets on the dot surface can be observed (dashed red line). The preferred formation of $\{111\}$ facets is typically observed in pure Ge nano-islands due to the low surface energy of 1.32 J/m^2 compared with the $\{110\}$, $\{311\}$ and $\{100\}$ facets exhibiting energy values of 1.51 J/m^2 , 1.61 J/m^2 and 1.71 J/m^2 , respectively [88]. Recent Density Functional Theory (DFT) calculations by Hörmann et al. [89] predict for pure Sn surfaces a favored $\{100\}$ facet growth. Since the islands' morphology follows the facet growth of Ge rather than Sn, a homogeneous incorporation of 1.4 at.% Sn into the Ge lattice is assumed, rather than the formation of a pure β -Sn wetting layer on top.

Fig. 4.9 shows the EDX map of the Ge and Sn distribution within the island.

EDX studies reveal a homogeneous distribution of (a) Sn (Fig. 4.9(b)) within

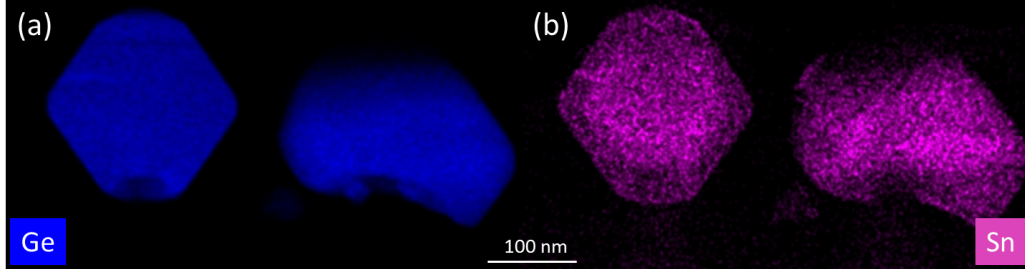


Figure 4.9: EDX map of (a) Ge and (b) Sn in the nanostructures grown at 600°C for 20 min. The scale bar of 100 nm is the same for both maps.

the Ge lattice (Fig. 4.9(a)), as indicated by the islands' morphology which is bound by low energy Ge- $\{111\}$ facets.

In the magnified TEM image of the island (Fig. 4.8 (b)) a defect rich GeSn/Si interface with dislocations and Stacking Faults (SFs) is visible, exemplary highlighted by a white arrow. The defects at the interface confirm the plastic relaxation of the nanostructures as indicated by the XRD results. However, the upper part of the island (Fig. 4.8 (c)) exhibits a high crystal quality – free of dislocations. The contrast changes in Fig. 4.8 (b) can be induced by the introduction of thickness inhomogeneities or strain in the lamella during TEM preparation.

Due to the absence of the *substrate compliance* effect, TDs and MDs are introduced into the nano-island at the early growth stage. The NHE growth however, leads mostly to defect-free GeSn nano-islands exhibiting only MDs at the interface, because the threading arms are gliding out of the nano-dots. Fig. 4.10 shows TEM image of the GeSn nano-islands grown for 20 min at (a) 650 °C and (b) 750 °C. Similar to the findings of the deposition at 600 °C, the GeSn nano-islands deposited at 650 °C and 750 °C are predominantly bound by $\{113\}$ and $\{111\}$ facets. Hence, increasing the growth temperature does not change the islands' morphology.

Note, that TEM analysis enables the characterization in nano-scale, but gives no statistical information about the nanostructures analyzing only few single islands. Nevertheless, the TEM results are confirmed by XRD measurements and the other way around. Thus, both methods give a comprehensive char-

acterization of the GeSn nanostructures.

TEM analysis revealed that the GeSn nano-crystals are bound predominantly by $\{111\}$ facets and are fully plastically relaxed by introduction of dislocation and SFs at the island/substrate interface. Importantly, most part of the islands is defect-free and thus, could be suitable for light emission. To directly compared the PL spectra and to analyze the influence

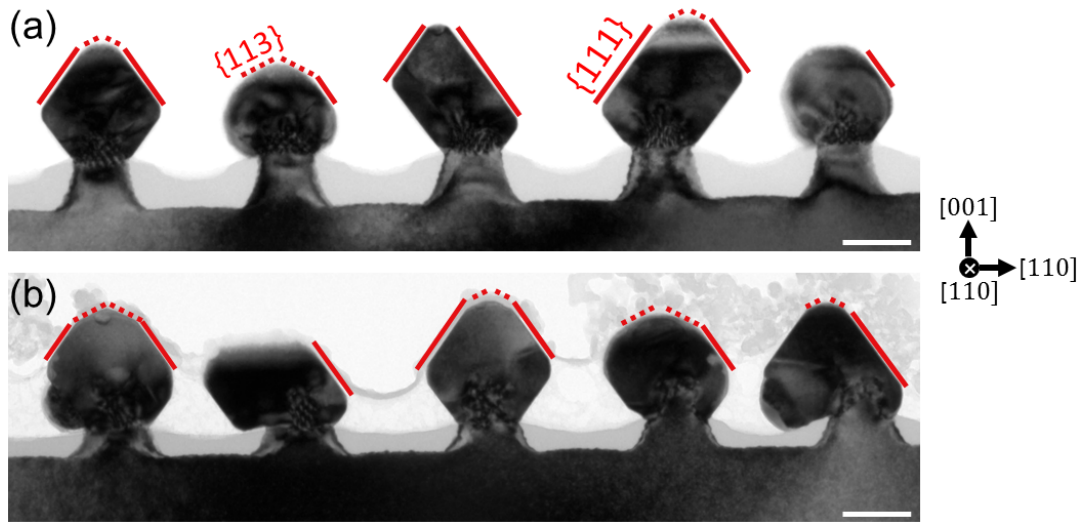


Figure 4.10: TEM micrographs of GeSn nanostructures grown at 650°C and 750°C for 20 min. Overview of $\{111\}$ (solid red line) and $\{113\}$ (dashed red line) faceted nano-islands with a scale bar of 100 nm.

of Sn on the bandgap, pure Ge nanostructures were grown under the same growth conditions (5.4 nm/min, 20 min growth) as the GeSn islands. SEM micrographs of the Ge crystals at the corresponding growth temperatures are shown in Fig. 4.11 The Ge islands grown at various growth temperature form large islands on top of the nano-patterned Si substrate exhibiting a strong coalescence. In line with studies by Niu et al. [54], the chosen growth conditions are in the non-selective regime for Ge growth on nano-patterned Si substrates, requiring growth temperatures of ≥ 850 °C and a deposition rate of about 1 nm/min. Hence, strong coalescence triggered by the high density of non-selective Ge dots on SiO₂ occurs leading to the formation of larger islands compared to GeSn, which desorbs immediately from the SiO₂

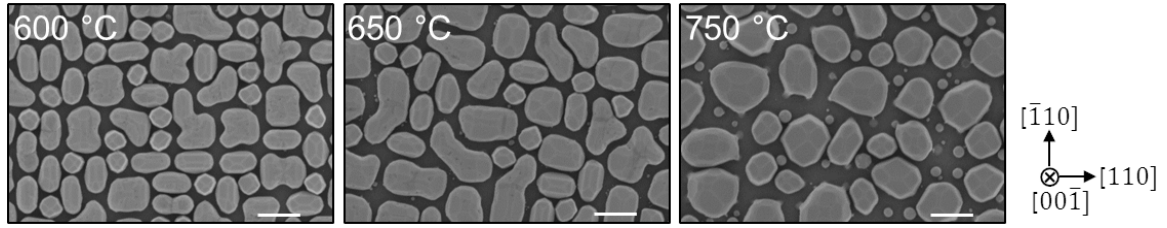


Figure 4.11: SEM micrographs (scale bare 500 nm) after 20 min deposition of Ge at 600 °C, 650 °C and 750 °C.

surface at > 650 °C.

μ -PL measurements were performed at room temperature, to characterize the optoelectronic properties of the Ge and GeSn NHE crystals. Firstly, Ge nano-islands grown at 600 °C for 20 min were characterized by PL and the spectrum shown in Fig. 4.12. At room temperature are clear PL signal of

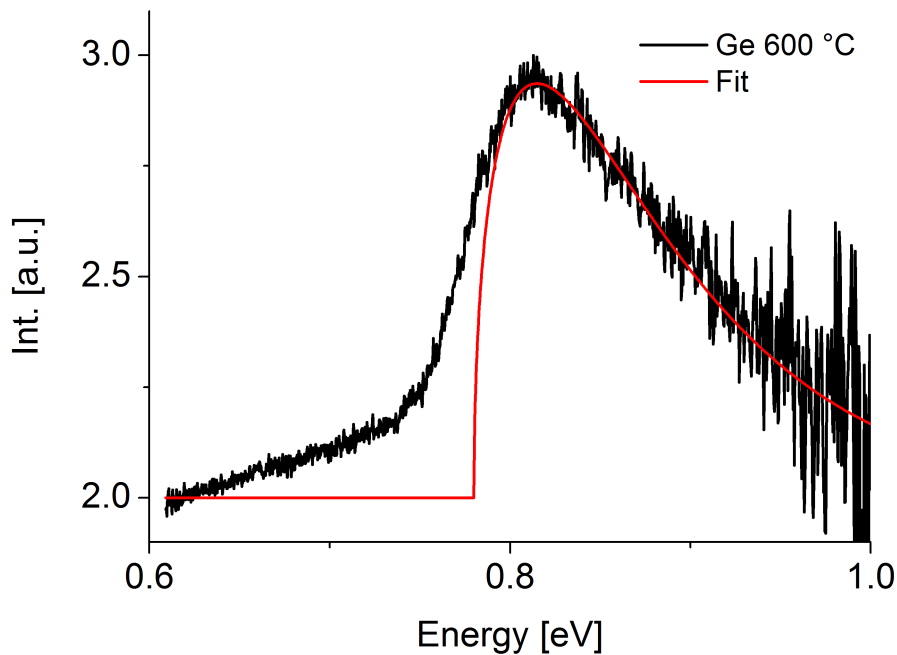


Figure 4.12: PL spectrum of Ge grown at 600 °C for 20 min (black graph). The PL signal is fitted assuming a direct radiative transition (red graph).

the Ge nanostructures can be detected, which is analyzed using Eq. 3.31 to

determine the bandgap energy. The PL measurements and the fit are in well agreement with each other. At low energy the PL peak can not be described by Eq. 3.31, because the PL intensity is determined by assuming a quadratic bandstructure taking into account the approximation of a reduced effective mass (see Eq. 3.3.1). However, usually a broadening of the valence and conduction band can be observed in experiment. Another important aspect is that during the PL measurements, the electrons are excited to higher energy states in the conduction band. Hence, the measured PL spectra differ from an ideal semiconductor with quadratic distribution of the joint density of states.

Nevertheless, using Eq. 3.31 a bandgap energy of 0.78 eV was determined, which is in very good agreement with the expected energy for the direct transition of pure Ge at (0.8 eV) [14]. It is also possible to extract the electron gas temperature, which can be some hundreds of Kelvin higher than the lattice temperature, because laser pumping of the electrons into higher energy levels is increasing the electron gas temperature.

Fig. 4.13 depicts the PL spectrum acquired at room temperature of the GeSn nanostructure deposited at 600 °C for 20 min. Similar to the Ge islands grown under the same growth conditions (600 °C, 20 min deposition time), a PL signal of the GeSn nano-islands can be observed. However, the PL peak shape differs. In case of GeSn two different contributions to the PL signal can be distinguished. The low energy component features a bandgap energy of 0.70 eV, while the higher energy component exhibits a bandgap energy of 0.79 eV. The bandgap energy of the first component is compatible with the $\Gamma_C - \Gamma_V$ transition of fully relaxed GeSn alloy with about 2 at.% Sn [15], which is in good agreement with the Sn content of about 1.5 at.% determined by XRD and EDX. The PL signal of the second component can be attributed to the direct radiative transition of pure Ge [14]. Possible reasons for the presence of Ge within the GeSn sample can be the (1) inhomogeneity of the nanostructures or (2) heating effect of the laser. (1) The characterization of the GeSn samples by both XRD giving an average information of many nano-dots and TEM-EDX analyses gaining the chemical composition of a single nano-island, did not confirm the formation of pure Ge within the

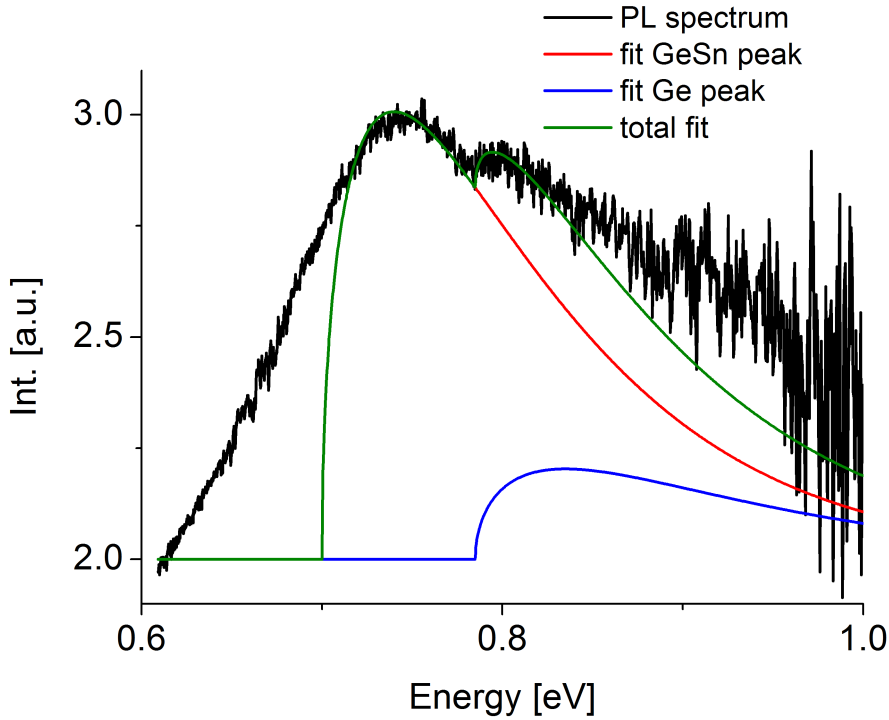


Figure 4.13: PL spectrum of GeSn grown at 600 °C for 20 min (black graph) with a laser power density of about 0.3 MW/cm^2 . The PL signal is fitted considering a direct radiative transition (red graph).

GeSn nanostructure. Hence, the presence of pure Ge within the GeSn nano—crystals is attributed to the heating of the sample surface by the laser during the PL measurements, despite the effort to keep the laser power density as low as possible. However, the laser power density cannot be further reduced, while maintaining a reasonable signal to noise ratio of the GeSn nano—dots.

Interestingly, the PL peak of the GeSn related component exhibits a linear increase of the low energy tail. Similar results have been obtained by Barget et al. [90] investigating highly n—doped Ge heterostructures. The linear rise of the PL peak at the low energy border is caused by the high donor dopant concentration (Phosphorous). Comparing these results with the GeSn study of this work, suggests that the Sn atoms can be treated as donor atoms, causing the observed linear increase of the PL peak at the low energy border.

The low signal to noise ratio around 1.0 eV can be attributed to the cut-off region of the extended InGaAs detector.

Fig. 4.14 shows the PL spectra acquired at room temperature of both the Ge and GeSn nano-islands grown at 600, 650 and 750°C for 20 min.

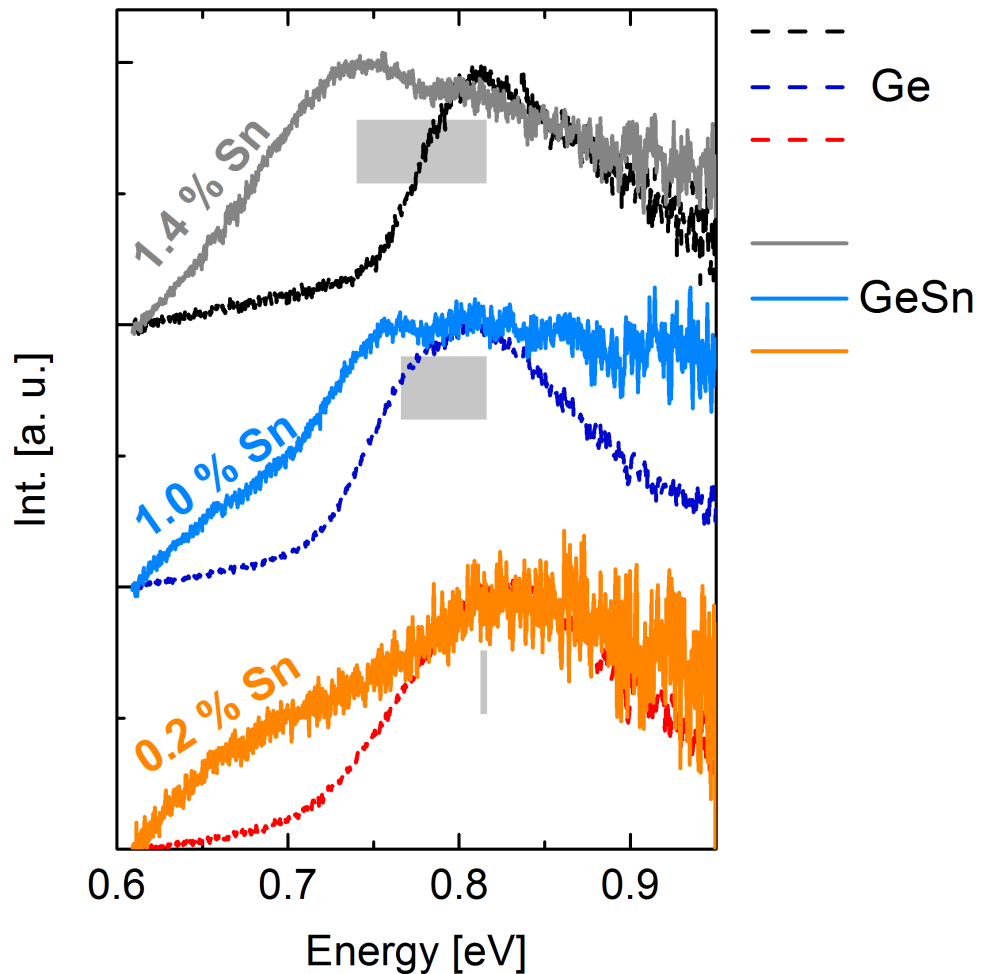


Figure 4.14: PL spectra of Ge (dashed lines) grown at 750°C (red graph), 650°C (blue graph) and 600°C (black graph.) GeSn nano-islands (solid lines) deposited at 750°C (orange graph), 650°C (bright blue graph) and 600°C (gray graph), corresponding to a Sn concentration of 0.2 at.%, 1.0 at.% and 1.4 at.%, respectively. A laser power density of about 0.3 MW/cm^2 is used and the intensity of the GeSn PL spectra is normalized to the maximum PL intensity of the corresponding Ge spectrum. The PL peak shift of GeSn compared to Ge is indicated by gray rectangles [86].

The PL spectra of the GeSn nano-islands (solid graph) are directly compared with those of the Ge nanostructures grown at the same substrate temperature (dashed lines). Since the PL intensity of Ge can not be compared with GeSn, due to the different electron-hole recombination lifetime of both radiative and non-radiative transition, the GeSn PL intensity is normalized to the maximum PL intensity of the Ge PL spectrum grown at same T_s to gain a better comparison of the PL peak position. The PL signal of the Ge reference samples remains relatively stable at all T_s . Using Eq. 3.31 to analyze the PL spectra, as shown exemplary in Fig. 4.12 for the Ge islands grown at 600 °C, a bandgap energy of 0.78 eV at the Γ -point can be extracted for all Ge samples.

The energy of the PL peak maximum of Ge compared to GeSn grown at 750 °C is almost identical. According to Eq. 3.31 the bandgap energy for both samples is about ≈ 0.78 eV characteristic for the direct radiative transition of pure Ge [15]. The determined Sn concentration of about 0.2 at.% is very low and hence, the GeSn sample deposited at 750 °C can be treated as pure Ge. However, the PL peak of the nanostructures grown by the co-evaporation of Ge and Sn features a broadening at the low energy border. The small PL peak at around 0.7 eV can be assigned to the combination of scattering processes due to the presence of defects and a contribution of the indirect transition, which is expected at 0.72 eV for pure Ge [30]. Unfortunately, the TEM characterization of the nano-crystals, cannot determine the exact defect density, because the contrast changes cannot be unambiguously assigned to defects, but are also caused by bending of the lamella during preparation. Hence for a full quantitative analyses of the crystal quality of the different samples, state-of-the-art TEM measurements of the nano-dots are necessary, which were not acquired during this study, but must be implemented in future work to analyze the impact of defects on the optoelectronic properties of the selectively grown GeSn NHE crystals.

In case of the GeSn nano-islands deposited at 650 °C (Fig. 4.14 bright blue graph), two main PL peaks can be observed featuring a bandgap of about 0.79 eV and about 0.72 eV, respectively. The first PL signal is identical with the Ge reference sample and hence, can be assigned to the direct

radiative transition of pure Ge. Although the power density on the sample surface was kept low $PD \approx 0.3 \text{ MW/cm}^2$ to avoid strong heating of the sample causing a degradation of the GeSn islands, a Ge related PL peak can be observed.

The second PL signal exhibiting a bandgap of 0.72 eV can be attributed to the direct transition of GeSn with a Sn content of about 1.5 at.% [15], which is in good agreement with the Sn content determined by XRD (see Fig. 4.4 (a)). The GeSn related PL signal is clearly redshifted in comparison to pure Ge (see gray rectangle), confirming the successful manipulation of the Ge bandgap by the incorporation of Sn.

Beside the Ge and GeSn related PL signals, an additional feature around 0.9 eV can be observed, which can be assumed to originate from the formation of SiGe or SiGeSn alloys. However, no significant Si interdiffusion was detected by both XRD (see Fig. 4.4 (a)) and TEM-EDX (see Fig. 4.5 (e)). Furthermore, this peak exhibits a low signal to noise ratio, peaking near the cut-off regime of the detector and hence, a clear assignment of the peak is not possible. These considerations suggest that the PL feature is a measurement artifact rather than a SiGe or SiGeSn related PL signal.

Finally, the PL peak of the GeSn nano-islands grown at 650 °C exhibits a broadening at the low energy border, which can be attributed to scattering effects caused by defects in the nano-islands.

Similarly to the results of the GeSn nanostructures deposited at 650 °C, the characterization of the GeSn grown at 600 °C (gray graph) confirms two main contributions to the PL signal. As discussed before one PL signal can be assigned to the direct bandgap related to pure Ge at about 0.79 eV, while the PL signal at about 0.7 eV matches very well with the $\Gamma_C - \Gamma_V$ transition of fully relaxed GeSn alloy with a Sn content of 2 at.% [15] and corresponds very well the determined Sn concentration of 1.4 ± 0.5 at.%. The direct bandgap is further reduced compared to GeSn deposited at 650 °C, due to the incorporation of a higher amount of Sn into the Ge lattice (see gray rectangle).

Since in comparable studies of other groups investigating the bandgap of GeSn alloys the energy of the PL peak maximum is used for discussion, Fig. 4.15 shows the comparison of the PL peak energy as a function of Sn

concentration determined by XRD of GeSn islands grown in this study. GeSn

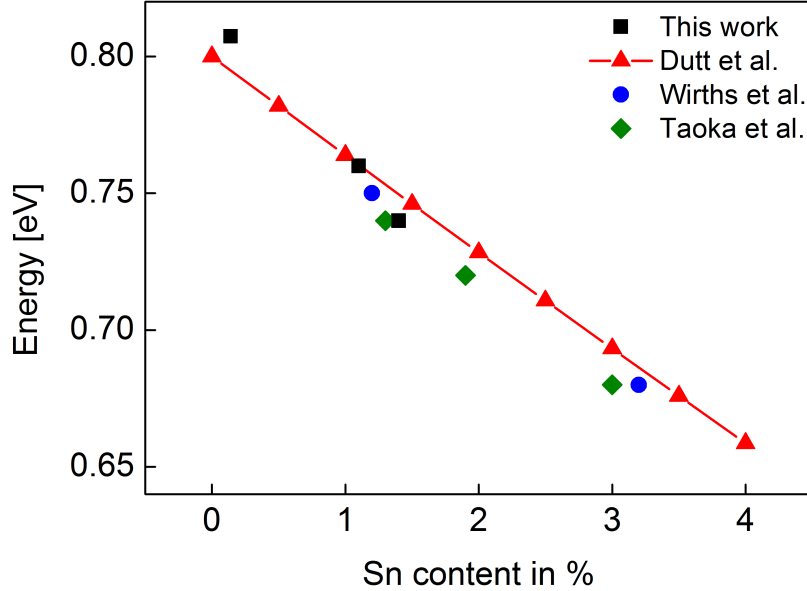


Figure 4.15: Comparison of PL energy of this work (black square) as a function of Sn concentration with literature: Dutt et al. [15] (red triangles), Wirths et al. [30] (green diamonds) and Taoka et al. [63] (blue circles) [86].

films characterized by other groups [30], [63] are also fully relaxed owing to the GeSn deposition on a Ge buffer and hence, are comparable with our NHE crystals. As a reference the calculation of the bandgap energy at room temperature for various Sn concentration is shown (red graph) [15]. The dependence of the PL peak energy on the Sn content obtained in this study aligns very well with both the film growth by other groups and the calculated bandgap energy by Dutt et al. [15]. The PL peak position of the GeSn nano-islands is decreasing from 0.80 eV to 0.73 eV with increasing Sn content. Thus, a shrinkage of $\Gamma_C - \Gamma_V$ of GeSn nanostructures can be achieved by varying the Sn concentration, demonstrating the potential of NHE crystals for future GeSn based optoelectronics devices.

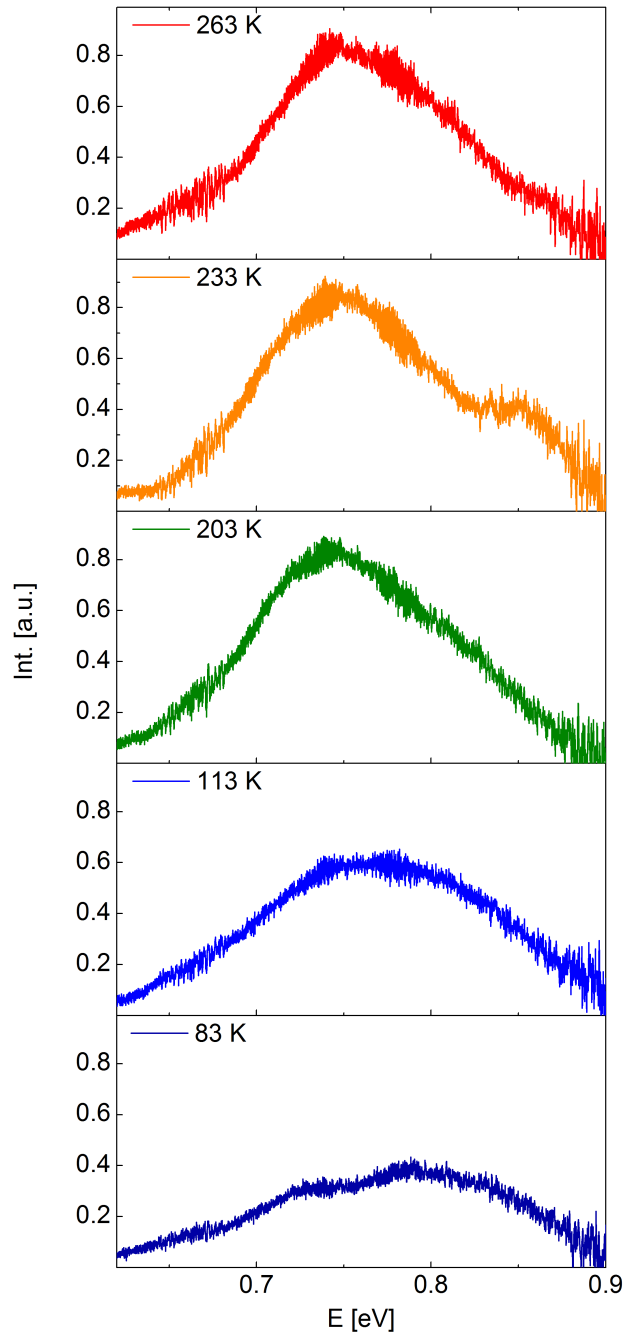


Figure 4.16: PL spectra in the temperature range of 83 K (dark blue) to 263 K (red) of GeSn nano-islands deposited at 600 °C for 20 min with a Ge flux of 5.4 nm/min and a Sn cell temperature of 1050 °C with a laser power density of 0.8 MW/cm^2 .

To further characterize the optoelectronic properties of the GeSn nano-islands, temperature dependent PL spectra of the GeSn dots with the highest Sn content (deposition at 600 °C) were acquired and are shown in Fig. 4.16. To gain a reasonable signal to noise ratio at low temperatures, it was necessary to increase the laser power density to about 0.8 MW/cm^2 . The interpretation of the temperature dependence on the PL peak position is difficult. At 80 K two signals are visible at about 0.80 eV and 0.73 eV, respectively. The peak at higher energy can be assigned to radiative transition at the Γ -point, while the peak at lower energy is attributed to an indirect radiative transition of a GeSn alloy with 1 at.% Sn. According to Eq. 3.32 (section 3.3.1) a bandgap narrowing is expected with increasing temperature. However, a quantitative analysis of the PL peak energy and integrated intensity is not possible, because Eq. 3.31 is only valid for the direct transition and hence, the low energy PL peak attributed to the indirect transition cannot be considered in the fit. Additionally, the generated heat from the laser during the time consuming temperature dependent measurements can cause phase separation of the alloy, when exceeding the eutectic temperature of GeSn. In Fig. 4.14 the formation of pure Ge can be observed already using a lower power density of $\approx 0.3 \text{ MW/cm}^2$ compared to the temperature dependent PL measurements acquiring a power density of $PD \approx 0.8 \text{ MW/cm}^2$. Therefore, it is assumed that PL signal consists of the direct and indirect radiative transition of GeSn as well as Ge, from which the contribution of $L_c - \Gamma_V$ cannot be considered using Eq. 3.31. Therefore, the following discussion will be in a qualitative manner.

In theory, the peak energy of both transitions is expected to feature a redshift with increasing temperature. In case of an indirect semiconductor the integrated PL intensity of the radiative recombination at the Γ point is increasing with increasing lattice temperature, while the PL intensity of the indirect transition is expected to decrease at higher temperatures. At low temperatures the electrons are populated in the L-valley decreasing the probability of radiative transition compared to Γ -valley, while at elevated temperatures the thermal energy is sufficient high to overcome the small energy barrier between the L- and Γ -point enhancing the direct radiative transmission, while

the indirect transition is reduced [27]. Indeed, an increase of the integrated PL intensity of the high energy peak can be observed increasing the lattice temperature, which is in agreement with theory, since the GeSn alloy with about 1.4 at.% Sn ((Fig. 1.4) is still considered as an indirect semiconductor.

Furthermore, PL peak position of the direct transition of GeSn is shifting to lower energy from ≈ 0.80 eV to ≈ 0.73 eV increasing the temperature from 80 K to 203 K, which is in agreement with the Varshni relationship according to Eq. 3.32. In the temperature regime between 203 K and 263 K the PL peak position remains relatively stable, which can be attributed to quantum confinement effect compensating the temperature driven shrinkage of the bandgap [91].

Summary

In summary, it is possible to grow GeSn nano-islands selectively by MBE on Si(001) nano-pillars. The selective growth is triggered by a desorption mechanism, where the impinging atoms immediately re-evaporate from the SiO₂ matrix, while the Ge and Si nucleate on the Si seeds forming stable clusters. A comprehensive characterization by SEM, XRD and TEM revealed a favored {111} facet growth similar to Ge and homogeneous incorporation of 1.4 at.% Sn at 600°C. The nanostructures possess a high crystal quality because defects like dislocations and SFs are trapped at the island/substrate interface. Using the NHE approach results in fully plastically relaxed GeSn nano-dots with negligible Si interdiffusion within the detection limit of XRD. PL measurements of the defect-free islands demonstrated the desired bandgap narrowing by increasing the Sn concentration. Beside the promising results of the selective growth of GeSn/Si at elevated T_s , some aspects can be optimized such as the relatively low Sn concentration or the thermal instability of the GeSn nano-dots, which was observed during PL measurements and caused by the heating of the laser beam.

4.2 Incorporation of Sn

Although the ratio of the Ge–Sn flux during the co-evaporation was selected for the formation of 4 at.% Sn in Ge, only 1.4 at. \pm 0.5% Sn was incorporated in the alloy. Figs. 4.17 (a–c) show a top view SEM image of the GeSn dots grown at 600 – 750°C acquired with an EsB detector to visualize the compositional contrast. On top of the GeSn islands (gray color) additional bright dots can be observed at all growth temperatures. In EsB detection mode heavier atoms appear brighter, indicating the formation of pure Sn.

The crystal morphology of the GeSn nano-islands can be observed in the SEM images (d–f). The islands are bound by several facets, which were identified in Fig. 4.8 and 4.10 as $\{111\}$ and $\{11\bar{3}\}$ surfaces. It can be reasonably assumed that the excess amount of Sn is not incorporated into the Ge lattice and diffuses out of the nanostructures driven by the thermal energy during high temperature growth. In Figs. 4.17 (g–i) it is clearly visible that Sn segregates decorate the nano-facets of the GeSn islands. With increasing the substrate temperature the size of the Sn segregates is decreasing.

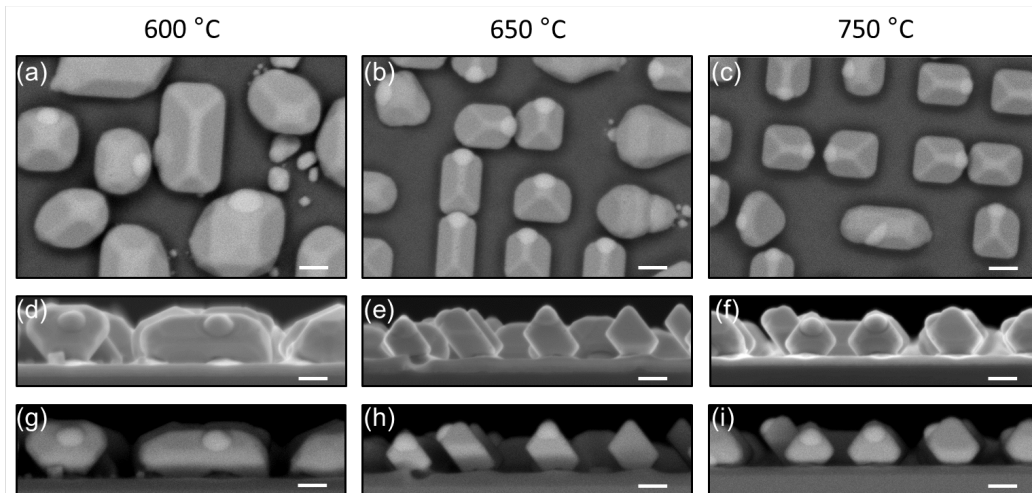


Figure 4.17: SEM micrographs of GeSn nanostructures grown at 600°C, 650°C and 750°C for 20 min. (a–c) Top view of nano-islands recorded with an EsB detector. Cross section image of the GeSn nano-dots using (d–f) an in-lense detector and (g–i) an EsB detector. The scale bar of all SEM images is 100 nm.

The diameter of the Sn *droplets* is about 95 nm, 80 nm and 77 nm at 600 °C, 650 °C and 750 °C, respectively. The reduction of the size of the β -Sn *droplet* implies an enhanced desorption of Sn from Ge at elevated temperatures. Studies of Wang et al. [92] confirm that the desorption of Sn from Ge(001) starts at > 500 °C. Consequently, increasing the growth temperature results in a decreased Sn island on top of the GeSn islands due to the enhanced desorption of Sn compared to lower substrate temperatures.

To confirm the formation of metallic β -Sn segregates and to investigate the impact of the Sn cell temperature on the selectivity and incorporation of Sn, the Sn cell temperature for co-evaporation of Ge and Sn was increased to 1100 °C aiming for 8 at.% Sn maintaining the Ge flux of 5.4 nm/min. Fig. 4.18 (b) shows the crystal morphology and (a,c) compositional contrast of the GeSn islands grown at 600 °C for 20 min with increased Sn cell temperature. The SEM contrast images show large *droplets* between the islands and on top of the nano-dots facets indicated as bright spots in the EsB detection mode. The diameter of the Sn segregates is about 200 nm, i.e. the size of the Sn *droplets* doubles using a Sn cell temperature of 1100 °C compared to 1050 °C (see Fig. 4.17 (a,d,g)).

The enhanced *droplet* formation enables the characterization of the segregates by XRD. Fig. 4.19 (a) shows a wide 2θ scan in specular measurement mode. The (004) diffraction peaks of single crystalline Ge and Si can be observed. The 2θ value of about 65.85° corresponds to a GeSn lattice with the incorporation of about 1.3 at.% Sn, which is the same Sn concentration compared to depositing with a Sn cell temperature of 1050 °C. Consequently, the size of the Sn *droplets* approximately doubles in size due to the increased excess amount of Sn (aiming for 8 at.% instead of 4 at.%), which was not incorporated into the Ge lattice.

Additionally to the Si (004) diffraction peak, a signal at $2\theta = 32.95^\circ$ corresponding to the Si (002) reflection can be detected. It is confirmed in literature [48] that the basis-forbidden Si (002) diffraction signal can be observed due to multiple diffraction.

The remaining signals at 2θ angles of about 30.61° , 31.92° , 43.91° and 44.91° can be assigned to the (002), (101), (022) and (211) diffraction signals of

β -Sn. Hence, the bright spots in Fig. 4.18 can be identified as polycrystalline β -Sn segregates.

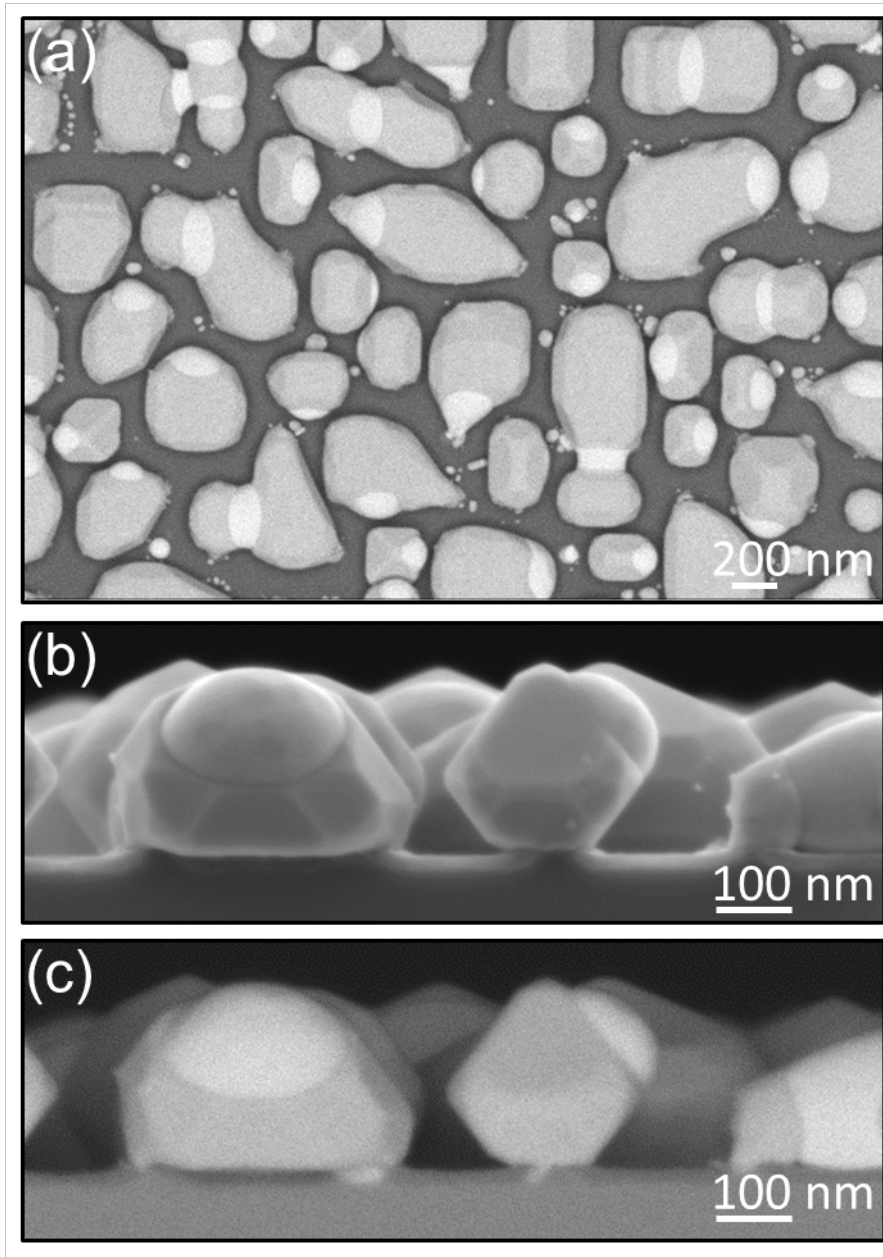


Figure 4.18: SEM micrographs of GeSn nanostructures grown at 600°C for 20 min with a Ge flux of 5.4 nm/min and a Sn cell temperature of 1100°C. (a) Top view of nano-islands recorded with an EsB detector. Cross section image of the GeSn nano-dots using (b) an in-lens detector and (c) an EsB detector.

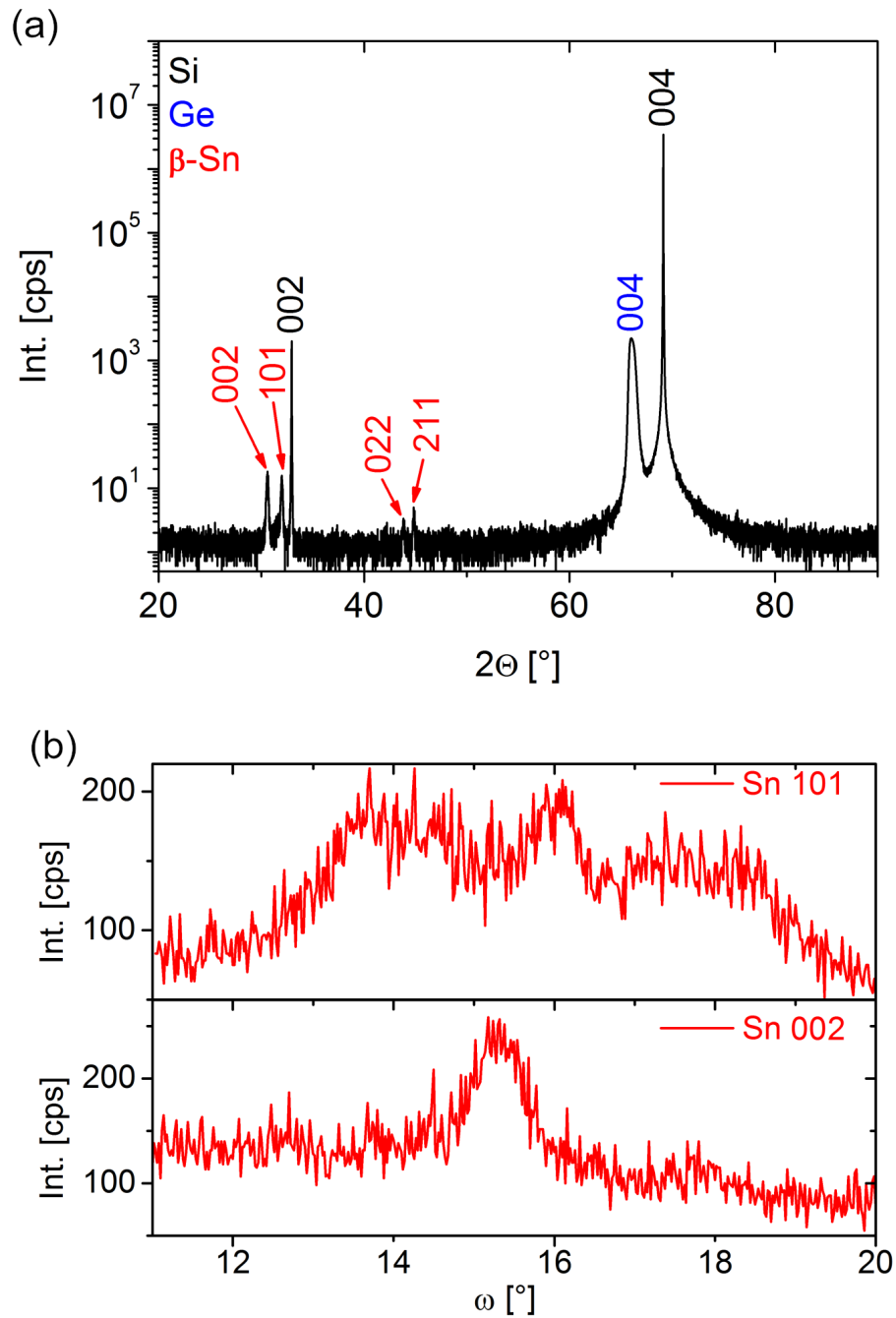


Figure 4.19: Out-of-plane diffraction curves of GeSn nanostructures grown at 600°C for 20 min with a Ge flux of 5.4 nm/min and a Sn cell temperature of 1100°C. (a) Wide 2θ scan and (b) ω scans (rocking curve) at Sn(101) and Sn(002) peak position.

Fig. 4.19 (b) depicts the Ω scans (rocking curves) of the Sn(101) and (002) diffraction signal. A broad distribution of some peaks can be detected in the Ω -range of $12 - 20^\circ$. However, no clear favored orientation of the tilted lattice planes can be observed, pointing towards a strong tilt of the lattice planes in the out-of-plane orientation with no favored tilt angles.

In summary, increasing the Sn cell temperature does not enhance the incorporation of Sn into the Ge lattice, but leads to the formation of large β -Sn segregates outside the GeSn nano-islands, which are polycrystalline and show tilted lattice planes in out-of-plane orientation with no preferred tilt angle.

4.3 Optimization of GeSn NHE growth

To incorporate more Sn into the Ge lattice by suppressing Sn out-diffusion, the islands have been capped by Ge. After 5 min co-evaporation of Ge and Sn at various T_s , the Sn beam has been blocked and the islands were subsequently overgrown by Ge for 5 min maintaining the corresponding T_s . The Ge capping layer should act as a barrier for the Sn atoms to migrate to the islands' surface.

Firstly to compare the crystal morphology between the nano-islands with and without cap, SEM and AFM images of the *as grown* and capped sample deposited at 600°C have been analyzed (Fig. 4.20). Both samples exhibit a low amount of non-selective GeSn dots on the SiO_2 matrix (Fig. 4.20 (a,b)), indicating a high selectivity. Similar to the previous investigations [54], the selective growth is driven by the high desorption rate of the arriving adatoms from the SiO_2 surface, while the Ge and Sn atoms tend to form stable clusters on the Si nano-pillar surface. Note, that in case of the capped islands (Fig. 4.20 (b)), more dots can be observed on the SiO_2 matrix owing to the additional Ge deposition at growth conditions outside the selective regime for pure Ge on Si enhancing coalescence of nano-dots formed on two Si pillars and on the vicinal SiO_2 matrix.

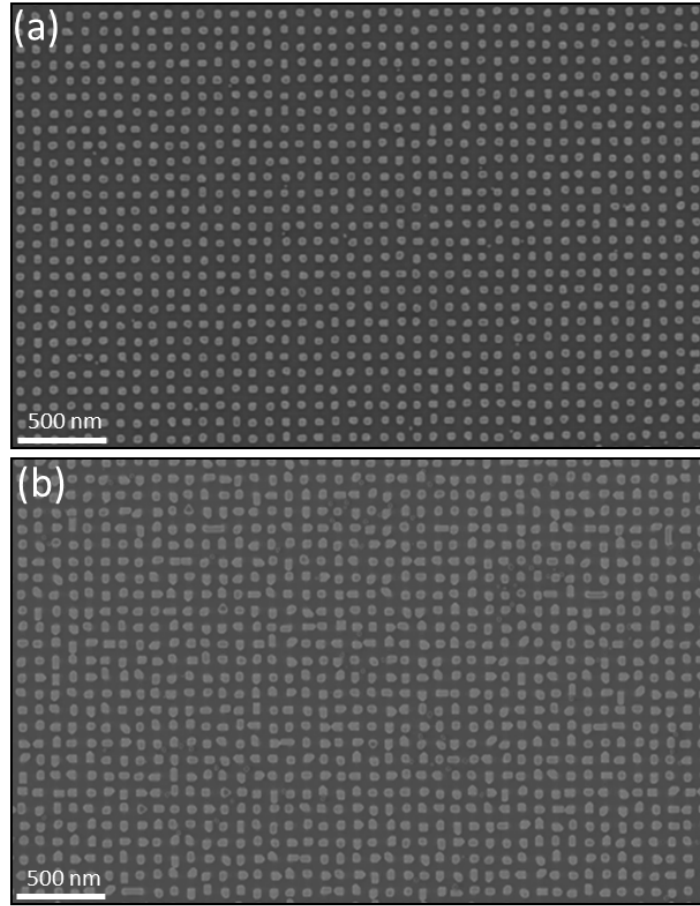


Figure 4.20: SEM micrographs of GeSn nano-dots grown at $T_s = 600$ °C (a) without and (b) with Ge cap [93].

Furthermore, AFM phase images in Fig. 4.21 (a,b) reveal different morphologies for the *as grown* sample compared with the capped one. The *as grown* nano-islands exhibit irregular shaped facets, while the capped nano-dots are pyramidal shaped exhibiting well defined facets. Detailed analyses of the facet orientation shown in the pole figures 4.21 (c) and (d), confirm in case of the *as grown* dots the coexistence of $\{111\}$ and $\{113\}$ facets, while the capped GeSn nanostructures are bounded by $\{111\}$ facets.

Additionally, *droplets* (white dashed circles) can be found on the facets of the *as grown* nanostructures, which can never be observed on top of the capped islands.

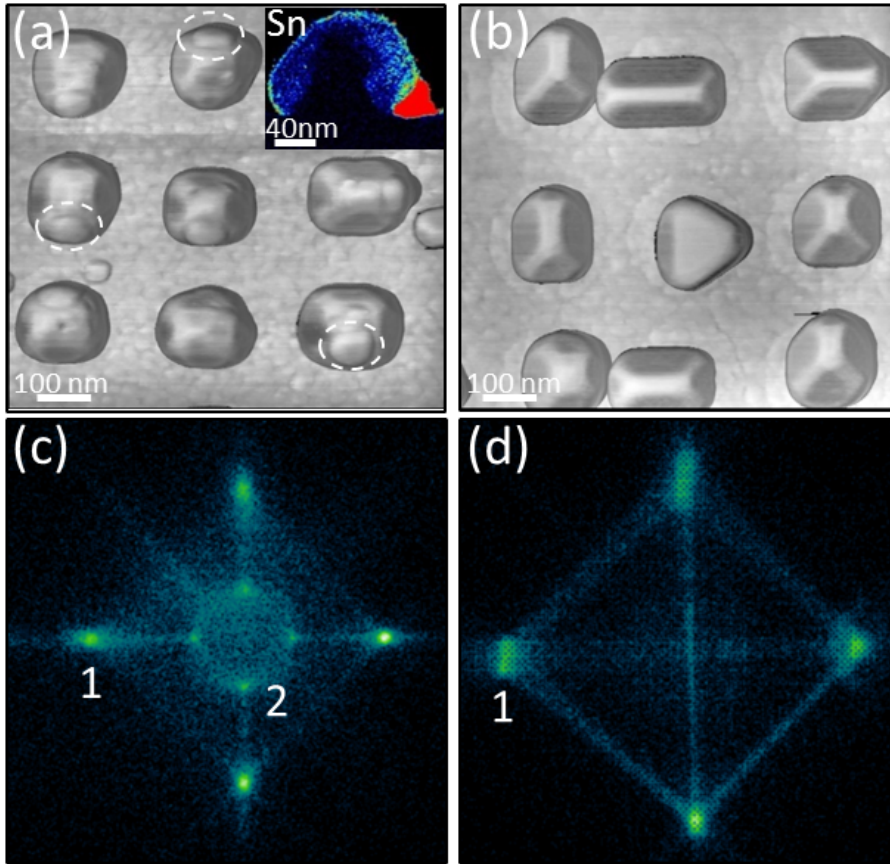


Figure 4.21: (a, b) AFM (phase image) micrographs of GeSn nano-dots grown at $T_s = 600\text{ }^\circ\text{C}$ (a) without and (b) with Ge cap. (a) some Sn segregates are indicated by white dashed circles, the inset displays the Sn distribution within the islands determined by EDX confirming an average Sn concentration of about 1.8 at.%. The different blue shades from dark to bright present a Sn content of 1 to 3 at.%. Pole figures of the facet angle distribution of GeSn nano-islands (c) without and (d) with Ge cap are depicted with the relevant $\{111\}$ and $\{113\}$ facets indicated by (1) and (2), respectively [93].

An EDX map of the Sn distribution (inset Fig. 4.21(a)) revealed that the *droplets* on the nano-facets of the *as grown* sample consists of β -Sn, which diffused out of the GeSn islands. Remarkably, all Sn segregates are located on $\{111\}$ facets. Recently, Groiss and co-workers [61] investigated the thermal behavior of β -Sn *droplets* on $\text{Ge}_{0.9}\text{Sn}_{0.1}$ films at temperatures above the eutectic temperature T_{ec} of the GeSn alloy ($231\text{ }^\circ\text{C}$) [10].

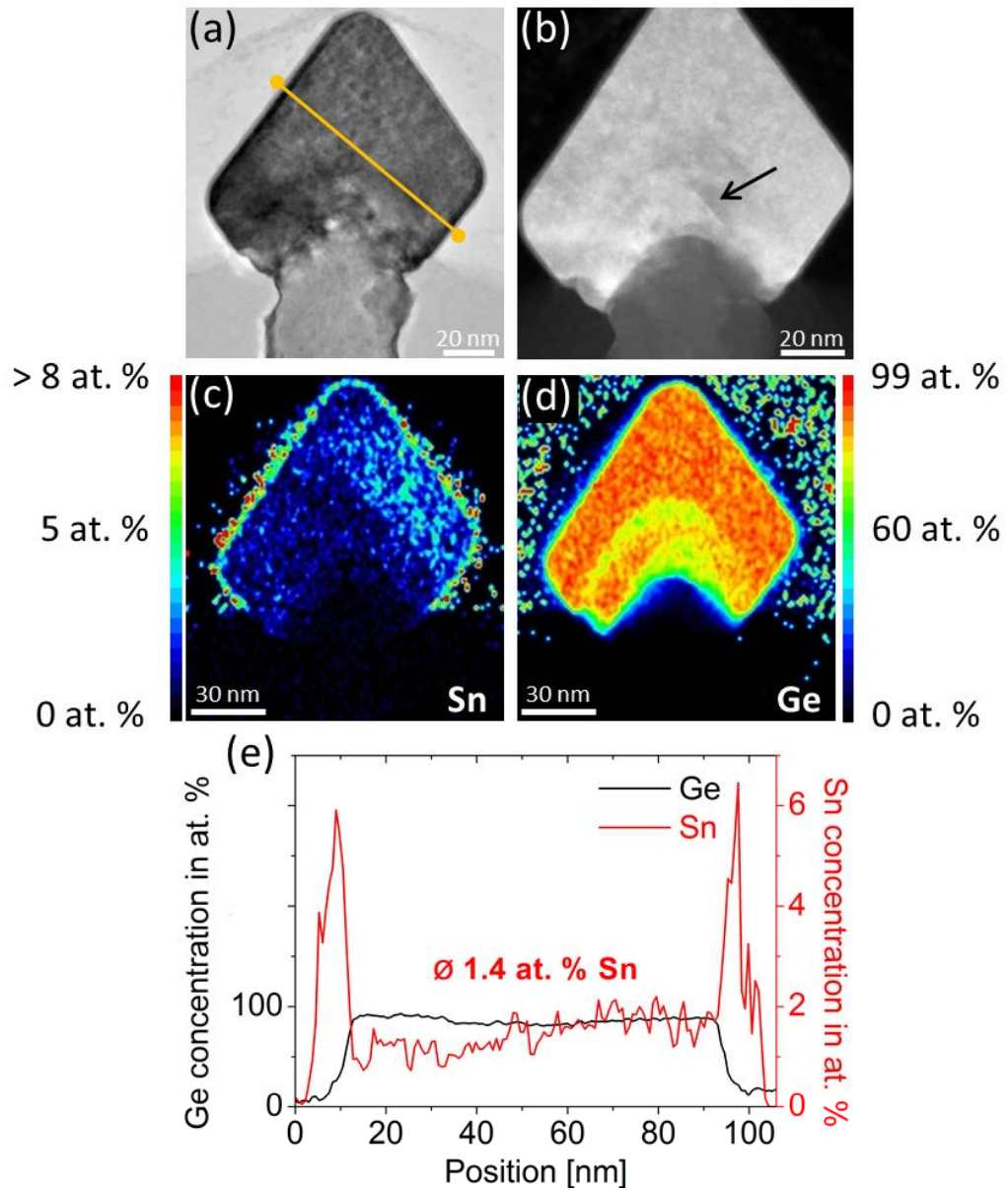


Figure 4.22: (a) TEM and (b) high angle annular dark field STEM image of Ge capped GeSn nano-dots grown at $T_s = 600 \text{ }^\circ\text{C}$. The black arrow shows exemplary interface defects. EDX maps of (c) the Sn content and (d) Ge concentrations are illustrated. Panel (e) depicts the Ge (black graph, left axis) and Sn (red graph, right axis) content across the line scan indicated in panel (a) by an orange line [93].

At $T > T_{ec}$ the Sn segregates are moving on the GeSn film surface, dissolving the underlying GeSn and re-deposit crystalline Ge in their trails. The re-crystallized Ge exhibits a low Sn concentration (< 1 at.%) and is decorated with small Sn *droplets* on $\{111\}$ facets analogously to the observation obtained in this study. Similarly to the studies of Groiss et al. [61], the subsequent overgrowth of GeSn islands with a Ge cap at $T_s > T_{ec}$, successfully dissolves the β -Sn segregates.

Next, the crystallinity and the chemical composition of the capped islands grown at 600°C is analyzed by TEM and EDX illustrated in Fig. 4.22. TEM and STEM images in Fig. 4.22 (a) and (b) reveal a high crystallinity of the capped GeSn island. Similarly to the *as grown* samples investigated before, the direct NHE growth of GeSn on Si leads to few defects near the interface region (indicated by black arrow in Fig. 4.22 (b)) owing to the high lattice mismatch ($> 4.2\%$ [30]).

The EDX map of the Sn concentration (Fig. 4.22 (c)) shows an enrichment of Sn on the island's surface without Sn segregation outside the dots, forming a homogeneous Sn-rich "crust" instead of a *droplet* on the $\{111\}$ nano-facet. The Ge distribution reported in (Fig. 4.22 (d)), confirms the formation of a Sn-rich GeSn alloy wetting the nano-island's surface rather than the existence of a pure Ge cap layer. T_s triggers a strong migration of the Sn atoms through the added Ge cap, forming a Sn rich *crust* on top of the GeSn nanostructures (see sketch in Fig. 4.23). Fig. 4.22 (e) reports the Ge (black graph, left axis) and Sn (red graph, right axis) concentration measured across a line scan (indicated as orange line in Fig. 4.22 (a)). Within the nano-island's "core" an average Sn content of 1.4 ± 0.5 at.% is determined, in agreement with the *as grown* samples deposited at 600°C . The Sn rich *crust* is about 6 nm thin and exhibits a Sn content of $\approx 6 - 7$ at.%.

The sketch in Fig. 4.23 illustrates the assumed growth scenario of the selective MBE growth of GeSn at $T_s > T_{ec}$. During co-evaporation of Ge and Sn, liquid Sn is wetting the GeSn nano-island surface. When cooling down the *as grown* sample, spherical β -Sn *droplets* are formed on the GeSn nano-facets (Fig. 4.23 (a)). The proposed growth strategy is to stop the Sn

evaporation and to continue the deposition of Ge (Fig. 4.23 (b)). The additional Ge atoms from the vapor phase consume the available Sn forming a Sn rich GeSn *crust*. The assumed growth scenario is similar to liquid–vapor deposition. Since the attractive force between GeSn/Ge is stronger than Sn/Ge a wetting *crust* is formed in case of capping the island, while the formation of Sn islands is favored in the case of the *as grown* samples. The influence of T_s

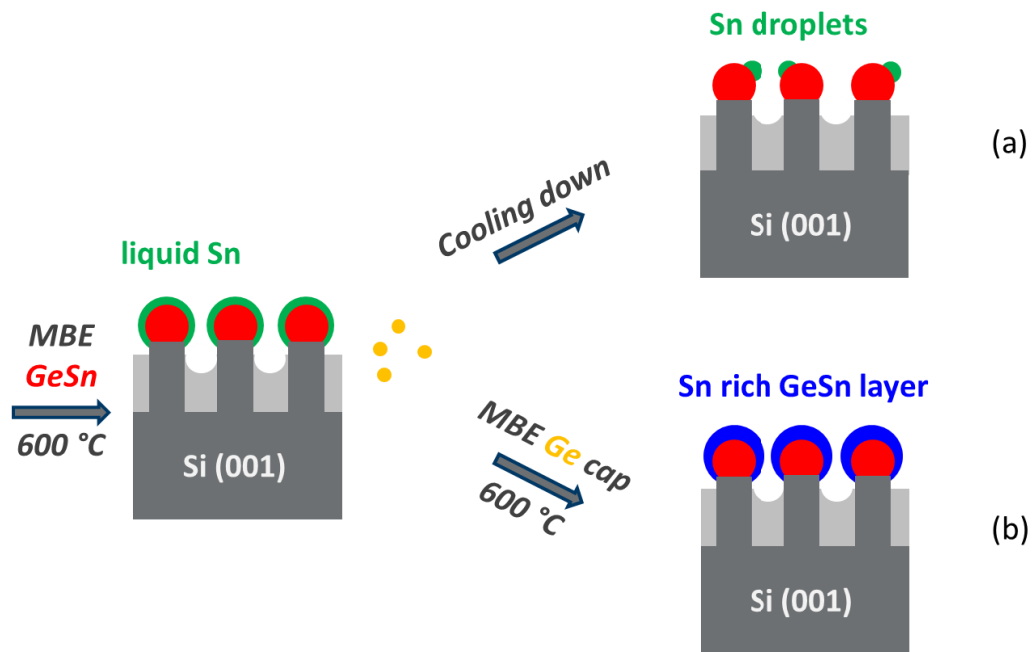


Figure 4.23: Sketch of growth mechanism during Ge and Sn evaporation exhibiting liquid Sn wetting the nanostructures surface. (a) Formation of Sn droplets on top of the islands after cooling down the sample to room temperature. (b) After capping with Ge a Sn rich GeSn alloy can be observed in the outer crust of the GeSn islands.

on capping the GeSn islands is investigated at 650 °C and 750 °C. Fig. 4.24 shows the AFM images analyzing the crystal morphology. In agreement with selective growth theory according to Leonhardt et al. [52], both samples exhibit a high degree of selectivity (Fig. 4.24(a,b)), where the desorption of the adatoms from the SiO₂ surface is enhanced with increasing T_s .

Fig. 4.24 (a) reveals that increasing T_s to 650 °C does not change the crystal morphology compared to the growth and capping at 600 °C. The islands

are pyramidal shaped and bounded by $\{111\}$ nano-facets confirmed by the pole figure plot 4.24 (c) . However, depositing at $T_s^{cap} = 750$ °C leads to a changed island shape. The inset of Fig. 4.24 (b) shows a spherical shaped island which consists of many small facets. The relative surface gradient plot in Fig. 4.24 (d) reveals a blurred facet distribution consisting of a wide range of different angle orientations. These spherical shaped dots on nano-patterned Si substrates were also observed by Niu et al. [54] during high temperature growth of pure Ge islands.

Although deposited at different T_s with or without Ge cap, all nano-islands show similar size and volume exhibiting a diameter of ≈ 180 nm and a dot volume of $\approx 2 \times 10^6$ nm³. The independence from T_s and/or the presence of the cap layer implies no simple lateral growth mechanism increasing the island size by adding a cap layer. These indications of a sophisticated growth mechanism following more complex growth kinetics fit the studies of Groiss et al. [61], where Sn droplets dissolve the underlying GeSn layer re-arrange the layer and re-crystallize Ge (with Sn < 1 at.%) in its trail. Furthermore, Sn acts as a surfactant enhancing the surface mobility of Ge atoms causing a re-arrangement of the Ge cap layer [94].

Consequently, the size and volume of the nano-dots is not simply increased by the addition of a capping layer, but a re-arrangement and re-crystallization of the underlying GeSn is caused by the presence of Sn.

EDX analysis of the Ge and Sn concentration of the capped islands at 650 °C and 750 °C are reported in Fig. 4.25. Similarly to the elemental distribution of the capped islands at $T_s = 600$ °C (see Fig. 4.22), Sn is homogeneously incorporated in the island *core* and enriched on the surface forming a Sn rich GeSn alloy (see Fig. 4.25 (a,b)). The Ge (black graph, left axis) and Sn (red graph, right axis) concentration (orange line in Fig. 4.25(a)) reveal a slightly lower average Sn concentration in the island *core* of 0.8 ± 0.5 at.% compared to the dots capped at $T_s = 600$ °C with a Sn content of ≈ 1.4 at.% (see Fig. 4.22(e)). However, the Sn concentration in the island *crust* is with ≈ 8 at.% almost identical to the Sn rich GeSn layer at $T_s^{cap} = 600$ °C. The outer *crust* is about 3 nm thin, which is half the thickness observed at 600 °C. Similarly to the decreasing size of the Sn *droplets* in case of the *as grown sam-*

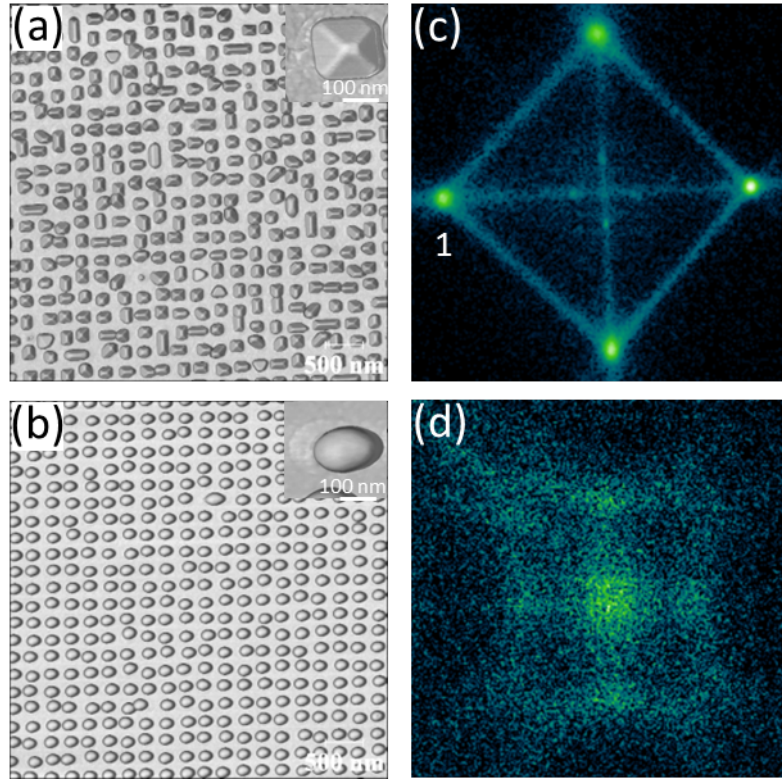


Figure 4.24: AFM phase images of capped GeSn dots deposited at (a) $T_s = 650$ °C and (b) $T_s = 750$ °C, respectively. The insets show magnified islands. Pole figures of the facet orientation of the GeSn nanostructures grown at (c) $T_s = 650$ °C and (d) $T_s = 750$ °C are also displayed. In panel (c) the $\{111\}$ facet is indicated by (1) [93].

ples, the reduction of the Sn rich GeSn layer suggests an enhanced desorption of the segregated Sn before capping the island with increasing temperature. Increasing T_s further to 750 °C leads to the formation of pure Ge. No Sn can be detected neither within the island *core* nor at the surface, similar to the results obtained in the 20 min growth implying that at 750 °C no Sn atoms are incorporated into the Ge lattice. The spherical shaped Ge nano-dots obtained in this study are very similar to the observation of Ge islands by Niu et al. [54] during high temperature growth of Ge on nano-patterned Si wafers.

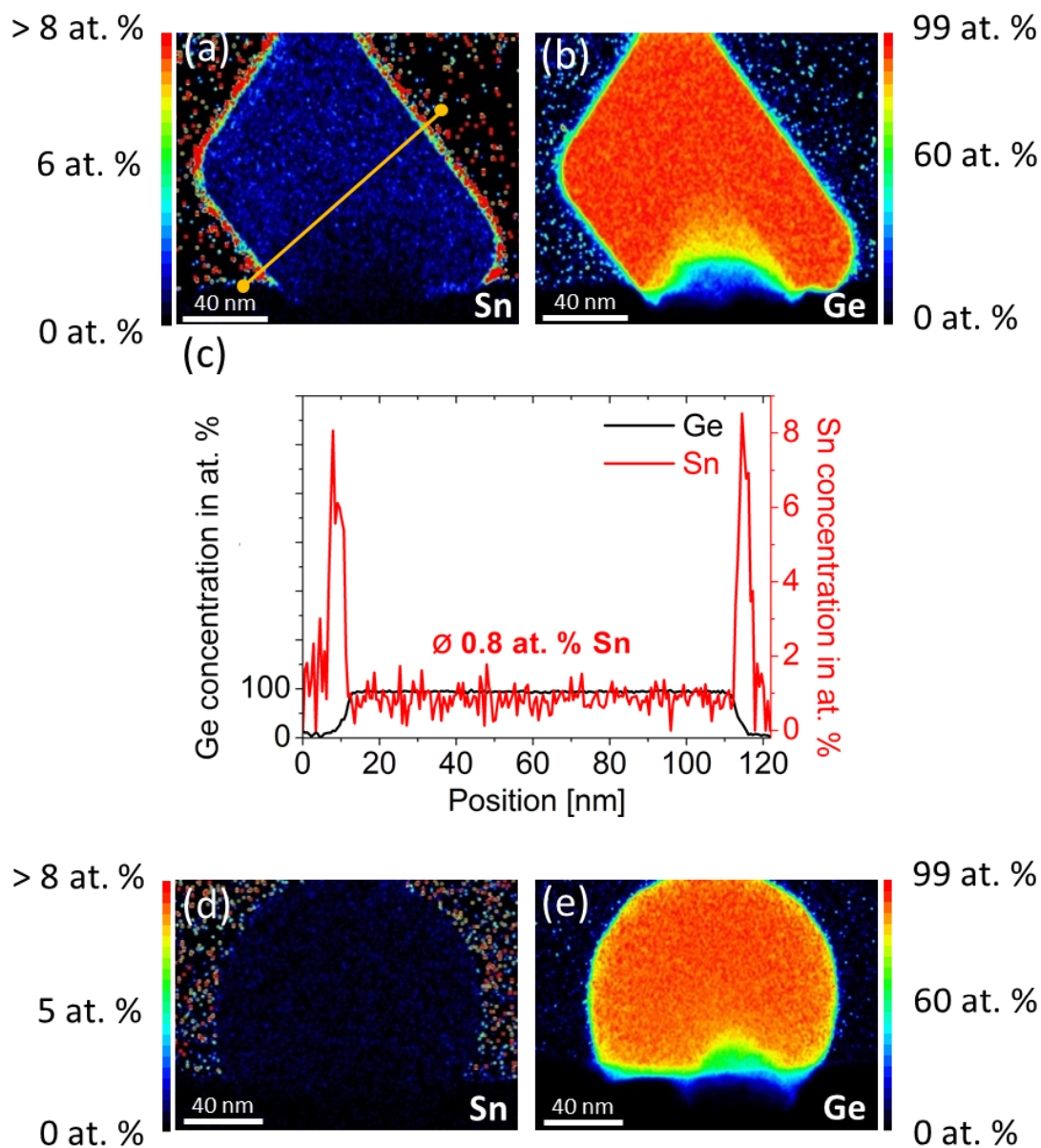


Figure 4.25: EDX maps of the (a) Sn and (b) Ge concentration of the capped GeSn nano-islands grown at $T_s = 650$ °C. Panel (c) displays the Ge (black graph, left axis) and Sn (red graph, right axis) concentration across the line scan indicated by panel (a) (orange line). Panels (d) and (e) depict the EDX maps of the capped GeSn nano-islands grown at $T_s = 750$ °C of the Sn and Ge content, respectively [93].

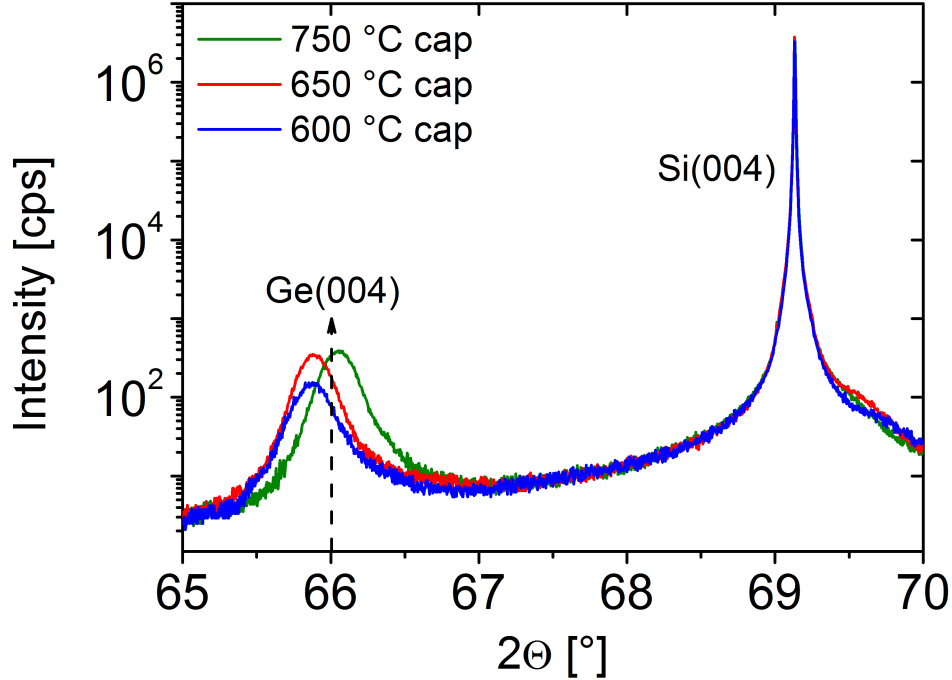


Figure 4.26: Specular (004) diffraction patterns of capped GeSn nano-islands at various T_s . The position of the Ge (004) Bragg reflection is given as a reference (dashed black line) [93].

To verify the results obtained by EDX, further structural analyses by XRD of the capped islands grown at various growth temperatures have been performed which are shown in Fig. 4.26. Since XRD is a *bulk* sensitive characterization method, the ultra thin Sn rich *crust* can not be resolved. However, the specular (004) diffraction pattern of the island *core* can be detected. The 2θ angle of the nano-clusters deposited at 600 °C and 650 °C is shifted towards lower values compared to *bulk* Ge (dashed, black arrow). This 2θ shift is pointing towards an increased lattice parameter due to the incorporation of Sn. The magnitude of the shift is comparable to a concentration of ≈ 1 at.% Sn in the Ge lattice in the island *core* [70]. These findings are in agreement with the Sn content determined for the island *core* by EDX (see Fig. 4.22 (e) and Fig. 4.25 (c)). However, depositing at $T_s = 750$ °C results in a shift to higher 2θ angle, i.e. smaller lattice parameter in respect to *bulk*

Ge. The decreased lattice parameter of the nano-dot *core* implies the inter-diffusion of Si into the nanostructures comparable with ≈ 1 at.% Si.[72].

Finally, the optoelectronic properties of the capped and *as grown* samples are investigated. Fig. 4.27 shows the PL spectra obtained at room temperature with an extended InGaAs detector covering the energy range down to about 0.62 eV (2000 nm). The *as grown* sample deposited at $T_s = 600$ °C for 5 min (black graph) shows no clear PL peak at room temperature, whereas a signal of the corresponding nano-islands grown for 20 min (see Fig. 4.14) can be detected owing to the larger island size causing a higher PL intensity. Comparing the 5 min NHE growth with and without capping, it is visible

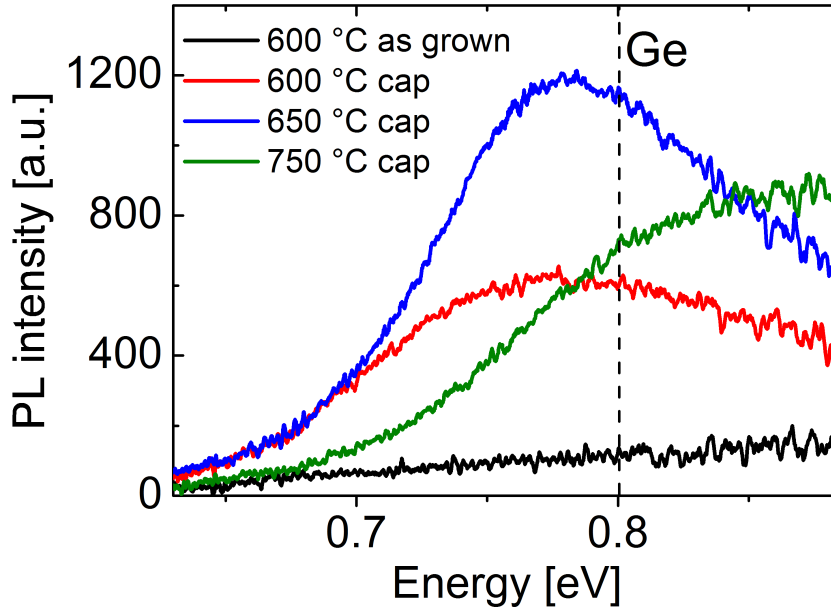


Figure 4.27: PL spectra of *as grown* sample (black) and capped islands at room temperature with a laser power density of 0.6 MW/cm^2 . The PL peak maximum of Ge grown at 600 °C is given as reference (dashed black line) [93].

that all capped samples exhibit a clearly detectable PL peak. The capped GeSn nano-dots deposited at $T_s^{cap} = 600$ °C (red graph) feature a PL signal at ≈ 0.77 eV (1620 nm), which can be unambiguously distinguished from the PL peak position of relaxed Ge (dashed black line) at 0.8 eV (1550 nm). The

red shifted bandgap of ≈ 0.77 eV (1620 nm) in respect to Ge corresponds to the indirect bandgap of relaxed GeSn with a Sn content of ≈ 1 at.% [15]. The determined Sn content is in good agreement with the results obtained by EDX for the island *core* (see Fig. 4.22 (e)). Hence, the direct comparison between the *as grown* and capped islands reveals that the capping layer enhances the radiative recombination efficiency of the nano-dot *core*, due to the addition of the capping layer acting as surface passivation. The island *core* PL feature is assigned to the direct radiative $\Gamma_C - \Gamma_V$ recombination due to negligible self absorption in thin films or nanostructures [90], [95].

The GeSn nano-dots capped at $T_s^{cap} = 650$ °C (blue graph) exhibit an even higher PL intensity and a reduced PL peak width. The enhanced radiative recombination with increased T_s^{cap} implies an improvement of the crystal quality by reducing point defects within the GeSn nanostructures. The PL position is shifted a little bit towards larger bandgap energy compared to the capped islands at $T_s^{cap} = 600$ °C which corresponds well with the slightly lower Sn content determined for the island *core* (see Fig. 4.25 (c)).

The PL signal of the nano-dots capped at 750 °C (green graph) is blue shifted compared to pure Ge. This shift towards larger bandgap energy can be assigned to a broadening of the bandgap, probably owing to Si interdiffusion from the pillar into the nano-islands indicated by XRD results (see Fig. 4.26). In fact, a bandgap of ≈ 0.9 eV (1377 nm) corresponds to the formation of a binary SiGe alloy with the incorporation of ≈ 1 at.% Si which is in very good agreement with the experimental results obtained in this study [96].

The optoelectronic properties of the GeSn nano-dots capped at $T_s^{cap} = 600$ °C were investigated further by temperature dependent PL measurements, reported in Fig. 4.28. The PL spectra were acquired with the same laser power density of about 0.8 MW/cm² as the *as grown* deposited at the same growth conditions. The integrated PL intensity is slightly increased with increasing temperature typically for direct radiative recombination in quasi-direct semiconductors [27]. Furthermore, a redshift of the PL peak with increasing lattice temperature can be observed.

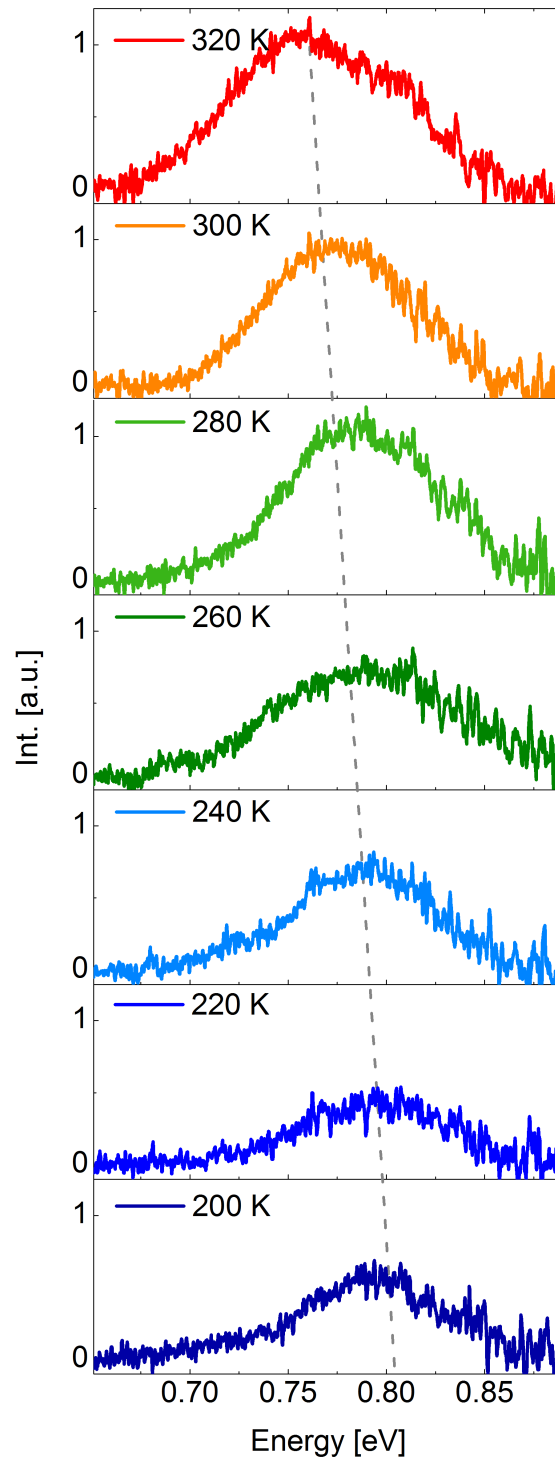


Figure 4.28: PL spectra measured with a laser power density of 0.8 MW/cm^2 in the temperature range from 200 K (dark blue) to 320 K (red) of GeSn nano-islands capped at $T_s = 600 \text{ }^\circ\text{C}$ (red).

The temperature dependent bandgap energy determined by Eq. 3.31 is shown in Fig. 4.29. The direct bandgap energy is fitted by the Varshni relationship according to Eq. 3.32. In the low temperature regime the bandgap

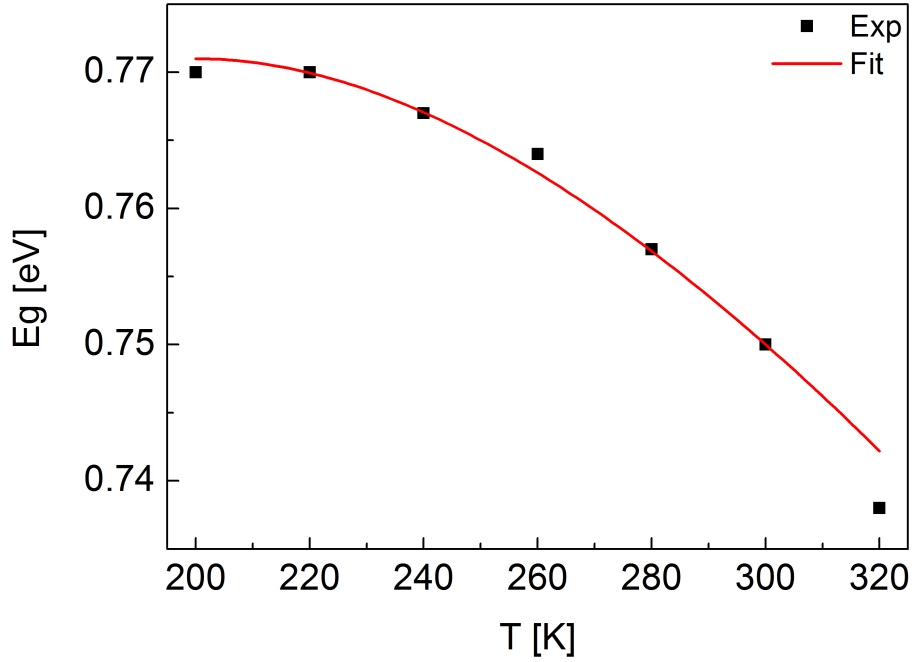


Figure 4.29: Bandgap energy as function of lattice temperature of capped GeSn islands at 600 °C (black squares). The red graph presents the fit according to Varshni relationship of the temperature dependent bandgap energy.

is slightly decreasing. A larger shrinkage of the bandgap can be observed at ≥ 260 K. These findings are in agreement with literature [79], where the shift of the relative position of the conduction and valence band depends on the temperature dependent expansion of the lattice. At low temperatures the thermal expansion coefficient depends in a nonlinear way on the temperature, while at high temperatures the dilatation of lattice depends linearly on temperature, because the impact of the thermal expansion coefficient on the variation of the relative position of the bandgap is limited to a small fraction. At high temperature the shift of the bandgap is mainly caused by temperature dependent lattice–electron interaction. The total shift of the PL signal

is about 0.03 eV increasing the lattice temperature from 200 K to 320 K. The obtained values for $\alpha = 8.5 \times 10^{-4}$ eV/K and $\beta = 305$ K are in the same range as reported in literature for direct bandgap of GeSn alloys [97], [98]. Note, that reasonable PL spectra were acquired even at lattice temperatures above room temperature compared to the *as grown* sample. The capped sample was stable during the time consuming temperature dependent PL measurements and in addition to that the sample was heated to about 45 °C (320 K) without any detectable degradation of the GeSn islands pointing towards a higher thermal stability of the capped sample.

Next, the GeSn islands capped at 650 °C were characterized by temperature dependent PL measurements. It was possible to slightly reduced the laser power density to about 0.6 MW/cm^2 , because the PL signal at room temperature was higher compared to the capped sample at 600°C. The PL spectra of the capped islands at $T_s = 650$ °C are shown in Fig. 4.30 in the temperature range of 80 K to 320 K. Analogously to the nano-islands deposited at $T_s^{cap} = 600$ °C (see Fig. 4.28), a redshift of the PL peak position as well as an increase of the PL intensity can be observed, when increasing the temperature. The temperature dependent bandgap energy determined by Eq. 3.31 is shown in Fig. 4.31. The experimental results of the temperature dependent bandgap energy is fitted by the Varshni relationship according to Eq. 3.32. Again, the trend of the bandgap shift is similar as observed for the GeSn nano-islands capped at 600 °C (see Fig. 4.29). The bandgap is slightly decreasing in temperature regime between 80 K and 200 K, above this temperature the position of the direct bandgap is decreasing faster, typically for an indirect semiconductor [79]. In the investigated temperature regime the shrinkage of the GeSn bandgap is about 0.07 eV. The values for $\alpha = 4.7 \times 10^{-4}$ eV/K and $\beta = 270$ K were obtained which are in good agreement with the values reported in literature for direct bandgap of GeSn alloys [97], [98].

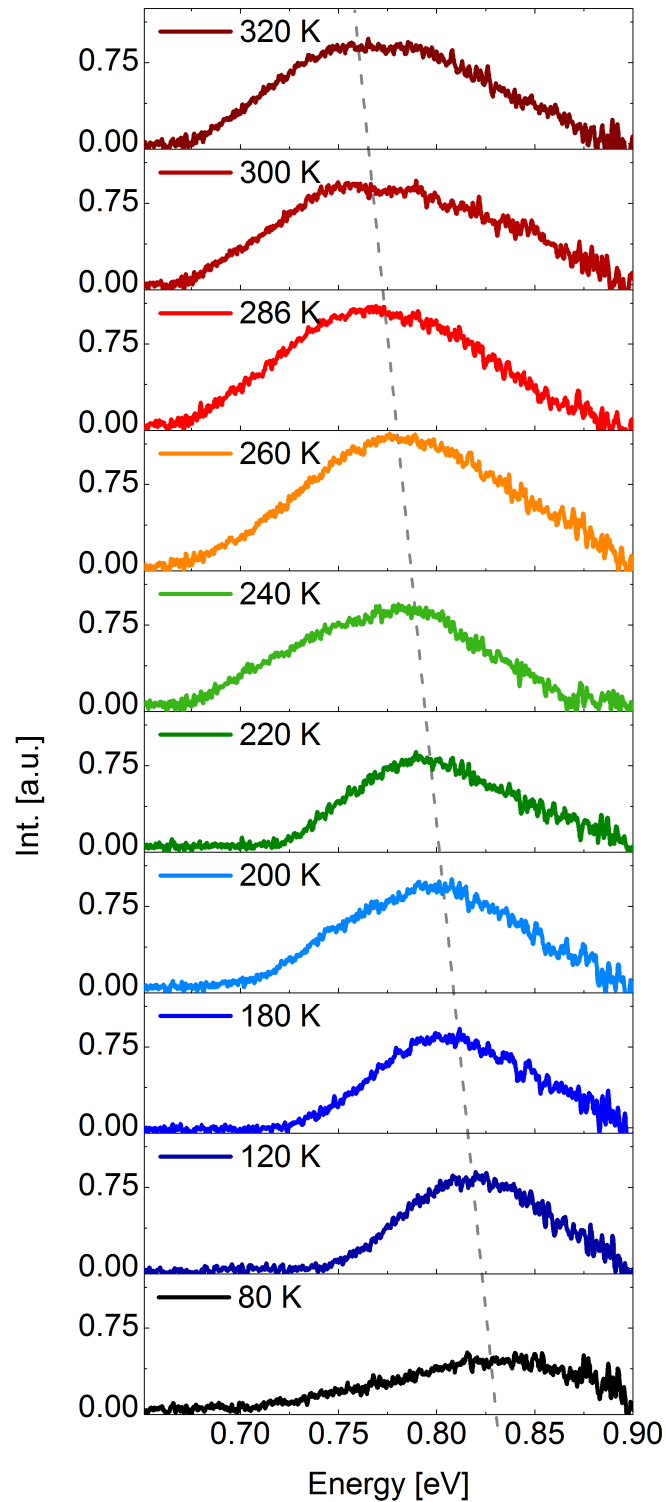


Figure 4.30: PL spectra measured with a laser power density of 0.6 MW/cm^2 in the temperature range from 80 K (black) to 320 K (brown) of GeSn nano-islands capped at $T_s = 650 \text{ }^\circ\text{C}$.

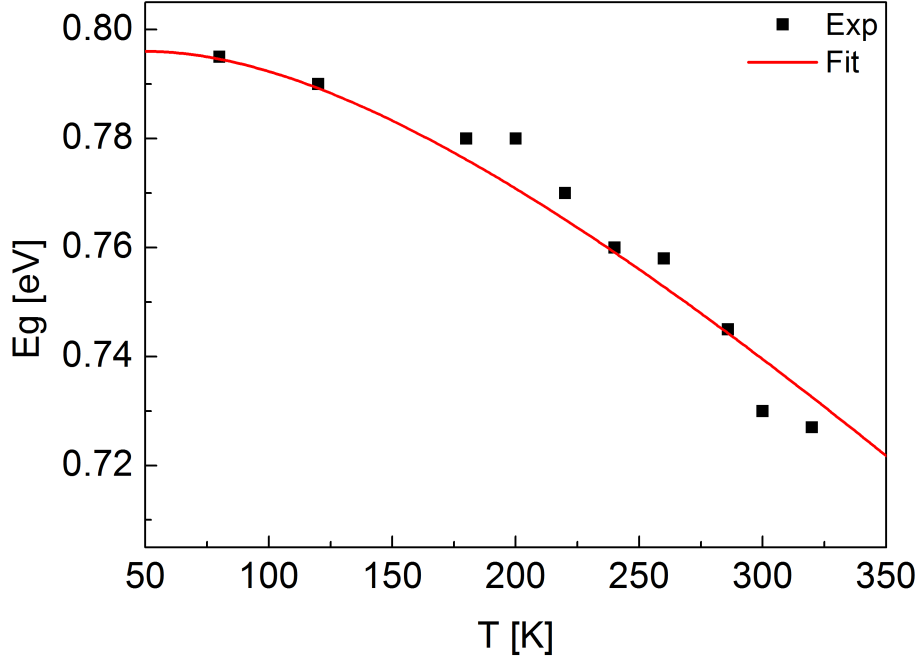


Figure 4.31: Bandgap energy as function of lattice temperature of capped GeSn islands at 650 °C (black squares). The red graph presents the fit according to Varshni relationship of the temperature dependent bandgap energy.

The PL signal of the Sn rich GeSn *crust* is expected to peak at an energy of < 0.59 eV ($2.1 \mu\text{m}$). Thus, further PL measurements of the capped samples at 600 °C and 650 °C were performed by using a PbS detector (see Fig. 4.32) covering the bandgap region down to < 0.35 eV ($3.5 \mu\text{m}$). The laser power density has been increased to $1.7 \text{ MW}/\text{cm}^2$ because of the intensity loss owed to the chopper required for the single channel PbS detector and the lower detector sensitivity compared to the extended InGaAs detector array.

Fig. 4.32 (a) depicts the PL spectra of the *as grown* and the capped samples as well as the Si(001) nano-pillar substrate acquired at 80 K. In line with previous observation of the absence of a Sn rich *crust* in case of the *as grown* nano-islands, no PL signal can be detected, while both capped samples show a PL peak at ≈ 0.545 eV (2275 nm), featuring an enrichment of Sn in the outer dots' *crust*. The observed bandgap is very well compatible with a GeSn

alloy of 7 at.% Sn [15], matching the Sn content determined by EDX for the Sn-rich GeSn *crust* (see Fig. 4.22 (e) and 4.25 (c)). To exclude any influence of the Si nano-pillars, the PL spectrum of the substrate is also shown as dotted magenta graph. A PL peak can be observed at ≈ 0.550 (2260 nm) which is clearly separated from the PL feature of the capped islands. This substrate related PL signal can be attributed to the spectrometer second order of the Si emission. Note, that the higher energy PL peak cannot be observed neither in case of the *as grown* sample nor the capped islands owing to the small penetration depth of the green laser (≈ 10 nm). These findings imply that the PL feature peaking at ≈ 0.545 eV (2275 nm) arises from the Sn rich GeSn alloy formed on top of the capped nano-islands at 600 °C and 650 °C.

Fig. 4.32 (b) reports the dependence of the spectral PL intensity on the lattice temperature for the capped dots deposited at $T_s = 600$ °C. Increasing the lattice temperature results in a decreased PL intensity and broadening of the peak. The PL intensity of a direct bandgap materials is typically increasing with decreasing lattice temperature owing to the suppression of non-radiative recombination processes.

In line with the PL investigations of the capped dots at $T_s = 600$ °C, the incorporation of $\approx 6 - 7$ at.% Sn in the outer *crust* is assigned to a direct semiconductor, while the island *core* is considered to be a quasi-direct semiconductor, typically exhibiting the strongest PL intensity at room temperature, due to the thermal activated electron transfer from the L_C to Γ_C . The PL peak position of the island *crust* shows no shift in the temperature range from 80 K to 300 K. According to literature [79] the bandgap is expected to shrink with increasing lattice temperature due to shift of the relative position of the conduction and valence bands caused by temperature dependent electron-lattice interactions. Thus, another process blue shifting the PL peak, has to take place. Indeed, a blue shift despite increasing the lattice temperature was observed by Wendav et al. [99], investigating ultra-thin Ge/Si quantum wells caused by a thermally activated transfer of the oscillator strength from the indirect to the direct radiative transition.

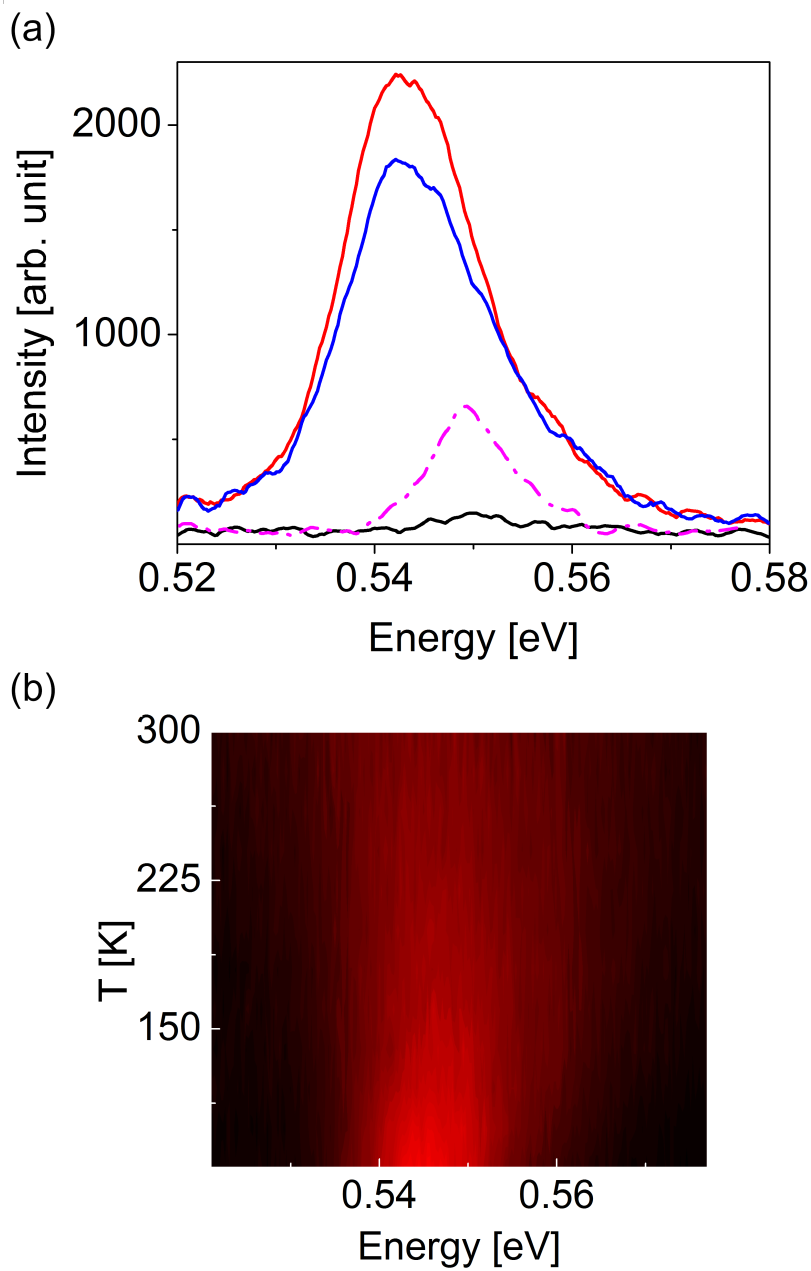


Figure 4.32: (a) 80 K PL spectra of *as grown* sample (black) and capped nano-dots at $T_s = 600^\circ\text{C}$ (red) and $T_s = 650^\circ\text{C}$ (blue). As comparison the PL spectrum of the Si nano-pillar substrate is depicted as dotted magenta line. (b) PL spectral intensity as a function of lattice temperature of capped GeSn nano-structures at $T_s = 600^\circ\text{C}$, where the integrated intensity at each temperature is normalized to unity. All PL spectra are recorded with a laser power density of about 1.7 MW/cm^2 [93].

Fig. 4.33 shows a first theoretical simulation of the bandstructure of the GeSn *core* and *crust*. The calculation support the PL results, predicting the radiative recombination of the confined holes in the GeSn outer *crust* pseudo-morphically grown on the 1 at.% Sn GeSn *core* and electrons in the L_c band indicated by the diagonal arrow in Fig. 4.33. Nevertheless, a comprehensive

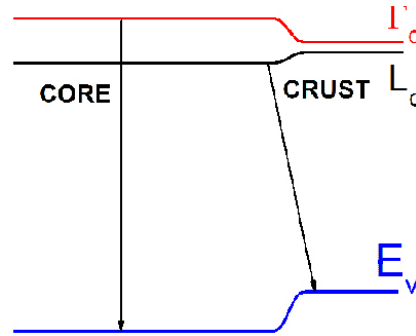


Figure 4.33: Calculation of the bandstructure of relaxed 1 at.% Sn in the island core and strained Sn rich GeSn crust [93].

experimental characterization of the *crust* layer by advanced analyses methods (e.g. atom probe tomography) are necessary to confirm the theoretical calculation.

Summary

In summary, the overgrowth of the GeSn dots with a Ge cap results in well defined pyramidal shaped nanostructures which are bound by the low energy Ge- $\{111\}$ facets [88]. No β -Sn *droplets* can be observed when capping the GeSn nano-islands. Thus, the formation of a Sn *droplet* can be successfully suppressed by depositing a Ge cap, while maintaining a high selectivity.

TEM and EDX analyses of capped sample at $T_s = 600$ °C revealed a high crystal quality of the GeSn nano-dots, only few defects can be found at the GeSn/Si interface. In agreement with the structural characterization of the *as grown* GeSn nanostructures, the island *core* exhibits a Sn concentration of 1.4 ± 0.5 at.%. The high temperature growth causes an enrichment of Sn on the surface. It is very likely, that during growth liquid Sn wets the GeSn

dot surface, which is incorporated into the additional Ge cap layer forming a uniform outer *crust* of a Sn-rich $\text{Ge}_{0.92}\text{Sn}_{0.08}$ alloy.

Increasing T_s to 650 °C results in the formation of pyramidal shaped nano-islands exhibiting a favored {111} facet growth, similar to the deposition and capping at $T_s = 600$ °C. At $T_s^{cap} = 750$ °C spherical shaped dots can be observed built up by many small facets spanning a wide range of facet angle orientations like Ge dots investigated by Niu et al. [54].

At $T_s^{cap} = 650$ °C the GeSn nano-islands exhibit an average Sn content of ≈ 0.8 at.% within the *core* and a Sn rich GeSn *crust* on the surface with a Sn concentration of ≈ 8 at.% similar to the results obtained by capping at 600 °C. However, increasing T_s further to 750 °C results in no incorporation of Sn into the Ge lattice and the desorption of Sn from the surface. In agreement with the NHE growth of pure Ge on nano-patterned Si substrates at elevated temperatures by Niu et al. [54], spherical shaped Ge nano-dots are formed at 750 °C.

Both XRD and EDX results confirmed the incorporation of ≈ 1 at.% Sn into the Ge lattice of the nano-dot *core* at $600 \text{ °C} \leq T_s^{cap} \leq 650 \text{ °C}$. At $T_s = 750$ °C a smaller lattice parameter in respect to *bulk* Ge can be observed, pointing towards Si interdiffusion into the nano-islands.

No clear PL signal of the *as grown* sample (5 min deposition) can be detected, whereas a PL emission can be observed of all capped islands. Thus, the Ge cap seems to improve the optoelectronic properties of the island *core* by acting as a passivation layer decreasing the surface recombination rate. The PL is red shifted in respect to the fundamental bandgap of relaxed Ge and corresponds to the incorporation of 1 at.% Sn [46] which can be assigned to the direct radiative recombination transition from the island *core*. A further enhancement of the optoelectronic properties is achieved by increasing T_s^{cap} to 650 °C, due to the reduction of point defects, i.e. the improvement of the islands' crystal quality. The deposition and capping at 750 °C results in a red shift of the PL peak position, i.e. increase of the bandgap caused by Si interdiffusion. The formation of a SiGe alloy with ≈ 1 at.% Si can be confirmed by both XRD and PL measurements.

PL measurements beyond the energy of 0.6 eV (2000 nm) on the capped nano-islands at 600 °C and 650 °C confirm the enrichment of 7–8 at.% Sn in the outer *crust* of the islands. The observed PL peak at ≈ 0.545 eV (2275 nm) fits very well with the bandgap for 7 at.% Sn in GeSn, which cannot be observed in case of the *as grown* sample, due to the absence of a Sn rich *crust*. Additionally, the influence of the bare nano-pillar Si substrate on the measured PL signal was excluded, since the second order Si peak at ≈ 0.550 eV (2260 nm) is well separated from the *crust* signal and cannot be excited by the green laser after the GeSn deposition, due to the low penetration depth. The relative strong PL peak implies a high crystal quality of the Sn rich GeSn alloy.

Further PL measurements at different lattice temperature of the capped sample at $T_s = 600$ °C, reveal that the temperature driven shrinkage of the bandgap is compensated by a thermally activated transfer of the oscillation strength from the lower energy (indirect) to the higher energy (direct) radiative transitions similar observed in Ge/Si quantum wells [99]. However, these findings have to be confirmed by further systematic studies.

4.4 Photodetection

Sample preparation

To investigate the photodetection ability of Ge and GeSn nanostructures, two sets of samples were fabricated according to the procedure in section 4.1 and listed in Tab. 2.1. The used sample ID in this chapter as well as the island diameter of the samples is summarized in Tab. 4.1.

Table 4.1: Overview of Ge and GeSn samples grown on p- and n-doped Si nano-pillars with various island diameter and the corresponding sample IDs.

Substrate doping	Sample ID	Diameter [nm]	New ID
p	GeSn15star	120	GeSn120
	GeSn15	155	GeSn155
	GeSn18	190	GeSn190
n	GeSn46	140	GeSn140
	Ge25 region 1	200	Ge200
	Ge25 region 2	160	Ge160
	Ge30 region 1	130	Ge130

The sample name ID indicates the type of the nanostructures (Ge or GeSn) and the diameter, e.g. sample *GeSn120* are GeSn nano-islands with a diameter of 120 nm.

The first set of samples consists of GeSn nano-islands with various island diameters that were deposited on p-doped Si nano-pillars with a low Boron (B) concentration of 10^{14} cm^{-3} . This substrate was used for all previous experiments. The second set of samples were grown on n-doped Si nano-pillars with a high Antimon (Sb) concentration of 10^{19} cm^{-3} .

Fig. 4.34 reports the top view SEM images of the GeSn nano-islands deposited on p-doped Si pillars. *GeSn120* and *GeSn180* were already discussed in the previous sections (see Fig. 4.2 and 4.3). All GeSn samples were deposited at 600 °C with a Sn cell temperature of 1050 °C. *GeSn120* (see Fig. 4.34(a)) and *GeSn155* (see Fig. 4.34(b)) were grown with a Ge flux of 5.4 nm/min, whereas for the deposition of *GeSn190* (see Fig. 4.34(c)) a

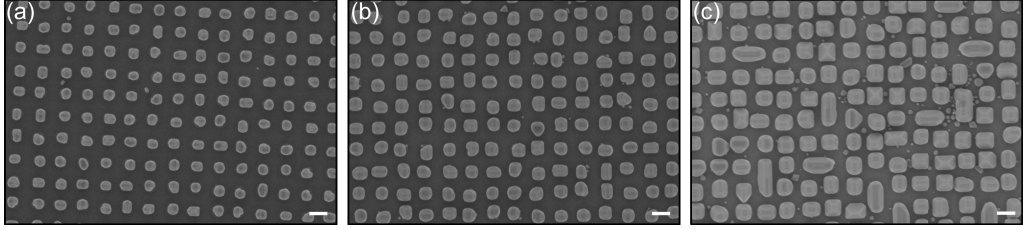


Figure 4.34: SEM micrographs of GeSn nano-dots grown at $T_s = 600$ °C (a) GeSn120, (b) GeSn155 and (c) GeSn190. The scale bar of all images is 200 nm.

Ge flux of 8.4 nm/min was used. All three GeSn islands exhibit an average Sn content of 1.4 ± 0.5 at.%. The island size varies depending on the deposition time.

Fig. 4.35 shows the SEM micrographs of the GeSn and Ge dots deposited on the n-doped Si pillar substrate. *GeSn140* (Fig. 4.35(a)) was grown at

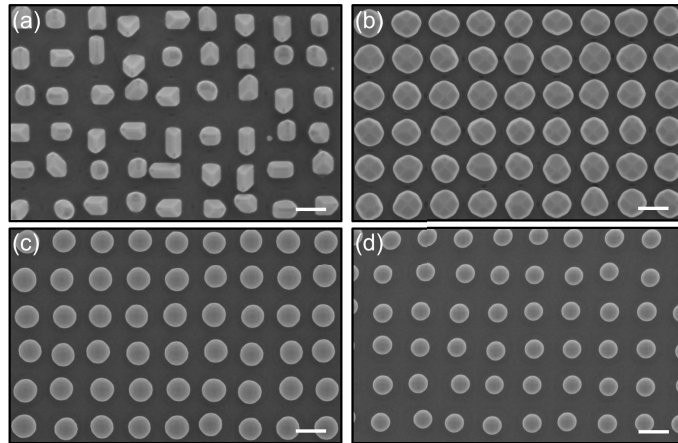


Figure 4.35: SEM micrographs of GeSn nano-dots grown at $T_s = 600$ °C (a) GeSn140, (b) Ge200, (c) Ge160 and (d) Ge130. The scale bar of all images is 200 nm.

600 °C with a Sn cell temperature of 1050 °C and a Ge flux of 5.4 nm/min. All Ge dots (Fig. 4.35 (b–d)) were grown at 850°C with a Ge flux of 1.0 nm/min, using the growth conditions for selective growth of Ge on nano-patterned Si substrates evaluated by Niu et al [54]. By varying the deposition time, the dot diameter was changed. Furthermore, two different sizes of Ge nanostructures were formed during one deposition, due to the inhomogeneous

heat distribution on the sample holder at the edge and at the center. The crystal shape of the Ge crystals exhibit a spherical shape bound by many small facets similar as obtained in the previous Ge islands grown at 750 °C (see Fig. 4.25(b)) as well as in the study of Niu et al [54].

The samples *GeSn140*, *Ge200*, *Ge160* and *Ge130* were fabricated especially for the photodetection measurements and hence, a structural characterization of these samples has not been shown in the previous sections, which will be briefly discussed in the following paragraph.

Fig. 4.36 reports the chemical distribution measured with EDX of sample *GeSn140*. In the STEM BF image (see Fig. 4.36 (a)) no TDs

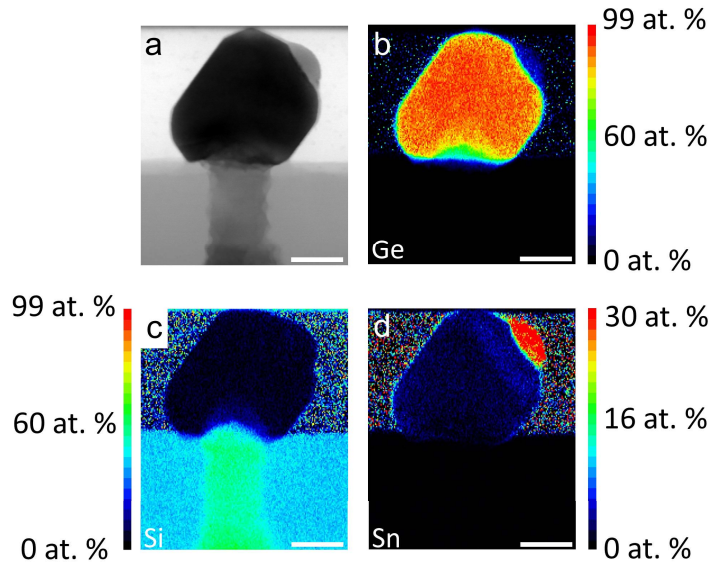


Figure 4.36: GeSn140 grown at $T_s = 600$ °C (a) STEM BF image, EDX map of (b) Ge, (c) Si and (d) Sn concentration. The scale bar of all images is 40 nm.

within the nano-islands can be observed. The chemical distribution of Ge (Fig. 4.36 (b)) and Sn (Fig. 4.36 (d)) confirms the homogeneous incorporation of 1.4 ± 0.5 at.% within the island *core*. On a nano-facet of the GeSn island a Sn *droplet* can be observed similar to the results previously reported for the *as grown* GeSn nanostructures (see section 4.2). Furthermore, the distribution of Si illustrated in Fig. 4.36 (c), is limited to a region between the GeSn/Si interface and 20 nm of the nano-island. Hence, the Si interdif-

fusion is relatively small compared to the whole GeSn island volume, because of the small island/pillar interface.

The chemical analyses of the Ge dots are summarized in Fig. 4.37. Here, one representative sample specimen of each deposition run is analyzed.

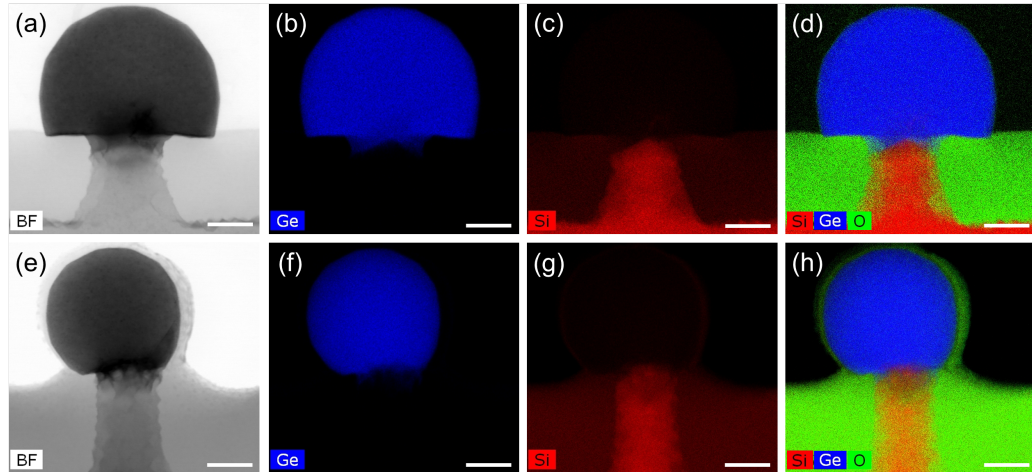


Figure 4.37: (a) STEM BF image, EDX map of (b) Ge, (c) Si and (d) Ge, Si and O distribution after the deposition of Ge200 and Ge160. (e) STEM BF image, EDX map of (f) Ge, (g) Si and (h) Ge, Si and O distribution after the deposition of Ge130. The scale bar of all images is 40 nm.

The STEM BF images in Fig. 4.37 (a,e) clearly demonstrate a high crystal quality of the Ge dots. The EDX map of Ge, Si and O confirm the deposition of Ge on Si nano-pillars surrounded by a SiO₂ matrix. Despite the high growth temperature of 850 °C, a small region of intermixing between Ge and Si can be observed at the island/substrate interface.

All samples summarized in Tab. 4.1 were covered with Al on the top side under an evaporation angle of 30° with respect to the normal of the sample surface to gain the effect of shadowing of the islands. Fig. 4.38 depicts the SEM and the TEM micrographs of the GeSn nanostructures deposited on p-Si substrate after metallization. The GeSn nano-islands are covered with Al and exhibit voids (black) next to the GeSn nanostructures, due to the shadowing effect of the islands. The Al layer thickness of *GeSn155* is about 80 nm and 100 nm in case of *GeSn120* and *GeSn190*, respectively.

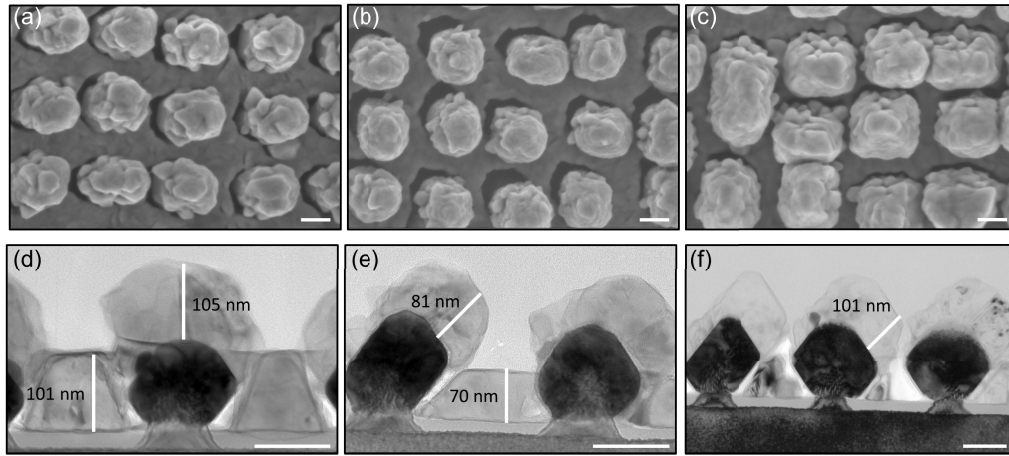


Figure 4.38: SEM top view of (a) GeSn120, (b) GeSn155 and (c) GeSn190 after the evaporation of Al. TEM cross section images of (d) GeSn120, (e) GeSn155 and (f) GeSn190 with the corresponding height of the Al layer. The scale bar of all images is 100 nm.

Fig. 4.39 shows the SEM micrographs of *GeSn140*, *Ge200* and *Ge130*, respectively. All three samples are grown on n-doped Si substrate and are

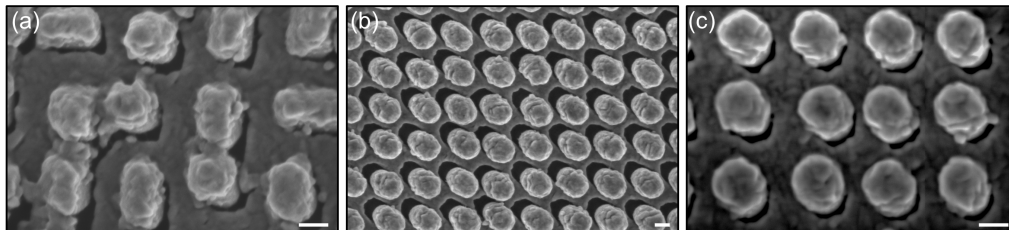


Figure 4.39: SEM top view of (a) GeSn140, (b) Ge200 and (c) Ge130 after the evaporation of Al. The scale bar of all images is 100 nm.

covered by Al exhibiting a void next to the island, which are used to enhance the incoming electromagnetic field by LSPs.

Furthermore to investigate the influence of different void sizes on the photocurrent measurements, sample *Ge160* was cut into two pieces and was covered with Al under two different evaporation angle, namely 30° and 45° in respect to the normal of the sample surface, which are labeled as *Ge160b* and *Ge160a*, respectively. The SEM images of both samples as well as the cross section TEM micrograph of *Ge160b* is depicted in Fig. 4.40. *Ge160a*

is more tilted compared to *Ge160a* during the evaporation of Al. Hence, the shadowing effect of the Ge dots is larger in case of *Ge160a* than for *Ge160b* with the identical island size. Consequently, the voids in case of *Ge160a* are with about 55 nm significantly larger compared with 21 nm large voids of *Ge160b*. The TEM cross section image of *Ge160b* in Fig. 4.39 (c) shows that the Al thickness of the top contact is about 70 nm to 78 nm. Note, that all

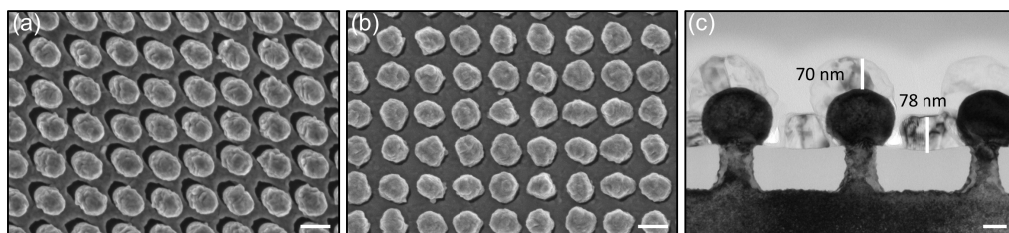


Figure 4.40: SEM top view of (a) *Ge160a* and (b) *Ge160b* after the evaporation of Al. (c) TEM cross section images of *Ge160b* with the corresponding height of the Al layer. The scale bar of the SEM images is 200 nm and of the TEM image 50 nm, respectively.

other samples grown on n-doped Si pillar substrate are contacted with Al in the same process as sample *Ge160b* and hence, the same Al layer thickness is assumed for *Ge130*, *Ge200* and *GeSn140*.

Simulation

To understand the band alignment in the Al-island-substrate-Al layer sequence and the influence of differently doped Si substrates, simulations were performed using the software COMSOL. A one dimensional model was assumed with a 100 nm thick Ge island and 2 μm thick Si substrate. Fig. 4.41 displays the bandstructure for (a) Al-Ge/p-doped Si-Al and (b) Al-Ge/n-doped Si-Al. The bandgap of Ge was set to 0.66 eV and of Si to 1.12 eV, respectively. The aforementioned substrate doping concentrations of 10^{14} cm^{-3} (p-Si) and 10^{19} cm^{-3} (n-Si) were assumed. For the metal-semiconductor interface, a barrier height for Si-Al was adjusted to 0.69 eV [100] and Ge-Al to 0.70 eV [101]. Note, that the previous discussion

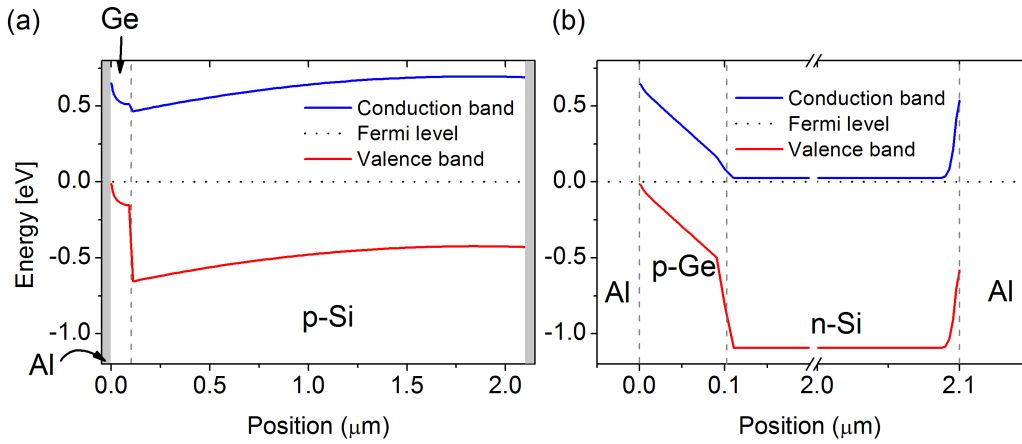


Figure 4.41: Calculated bandstructure of Ge on (a) p-doped and (b) n-doped Si. Both heterojunctions exhibit an Al contact on top and bottom.

about *Metal contacts* in section 3.3.2 neglects anomalies such as interface states. However, it is known that Ge-metal contacts feature the so called *Fermi level E_f pinning*, i.e. E_f of Ge does not change in contact with Al. Different theories attribute the Fermi level pinning to interface states or high defect density [102], [103], [104]. By the incorporation of 1 at.% Sn the bandgap of GeSn is slightly decreased with respect to pure Ge, however a similar behavior as for the Ge-islands is assumed for the GeSn nano-dots. Interestingly, in case of the heavily n-doped substrate a barrier between the Si substrate and the backside Al contact of about 0.5 eV can be observed. The spatial distribution of the electric field caused by the diffusion of the charge carriers is plotted in Fig. 4.42 for both p- and n-Si substrates at 0 V. The electric field in case of p-doped Si substrate (see Fig. 4.42 (a)) exhibits a negative value in the Ge nano-island region. At the backside contact the value of the electric field also drops below zero. Hence, a separation of the charge carriers is expected within both the Ge nanostructure and close to the backside of the p-Si substrate. To clarify the charge carrier diffusion directions, the electron and hole concentrations are shown in Fig. 4.42 (b). The holes diffuse towards the Si-Al backside contact, while the electrons move to the Ge-Al top contact.

In case of the n-doped Si substrate depicted in Fig. 4.42 (c), the spatial

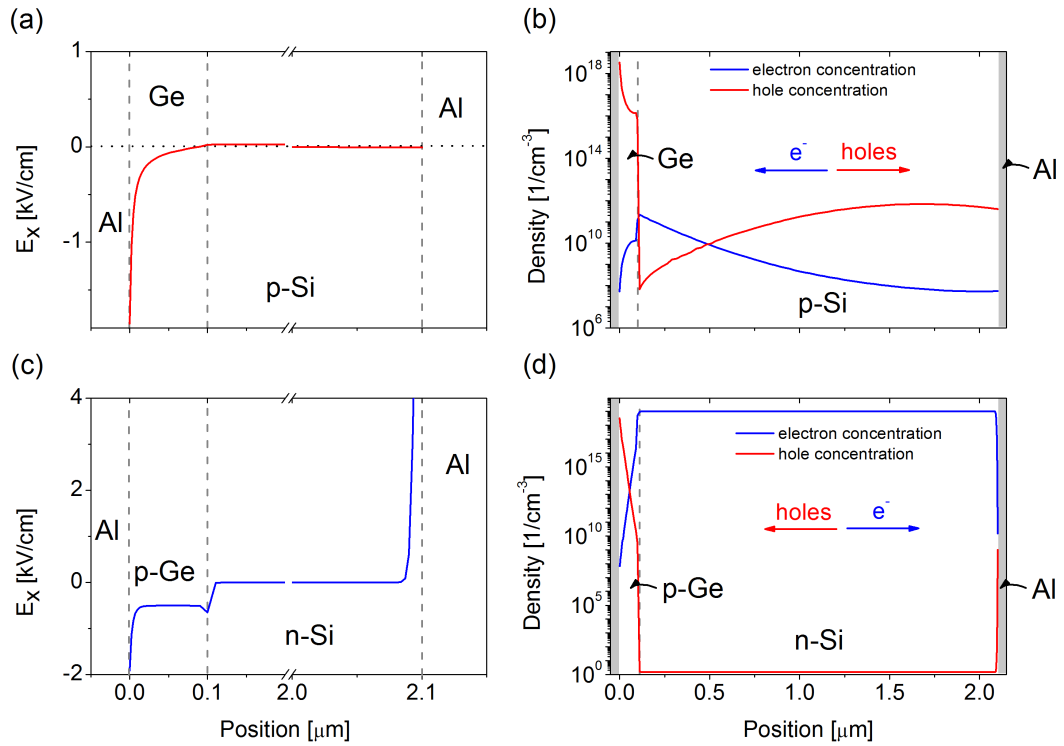


Figure 4.42: Calculated spatial distribution of the electric field in the Al-Ge-Si-Al heterostructure using (a) p- and (c) n-doped Si substrate at 0 V. Distribution of the carrier concentration in the islands deposited on (b) p- and (d) n-doped Si pillars at 0 V.

distribution of the electric field in the Ge nano-island is relatively large compared to the p-doped substrate, i.e. the depletion width is in the same order of magnitude as the diameter of the Ge island. Hence, this configuration of a heterojunction p-Ge/n-Si is not expected to feature a pronounced diode behavior. Analogously to the p-substrate case, the charge carriers are moving in opposite direction, i.e. the diffusion of the electrons can be observed towards the n-Si-Al backside contact and the holes move towards the p-Ge-Al top contact side. Note, that at the backside contact a relatively large increase of the electric field can be observed.

Photocurrent measurements

To measure the photocurrent the samples were glued onto copper plates using conducting silver paste. In the first step I/V curves of each sample were recorded and are displayed in Fig. 4.43. The GeSn nano-islands grown on

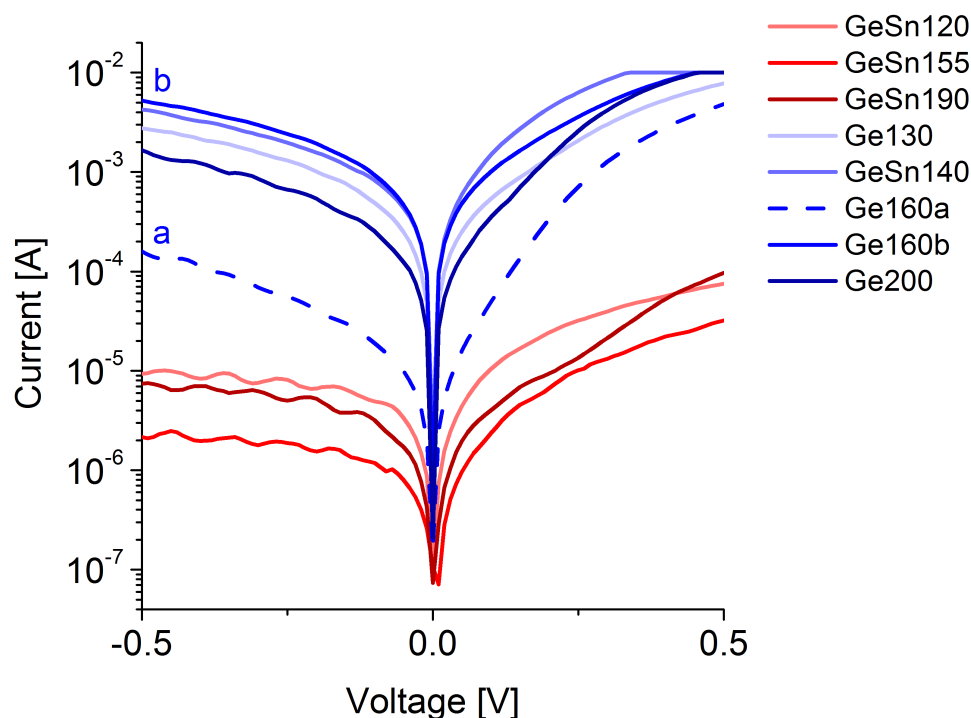


Figure 4.43: I/V curves of all samples grown on p- (red colors) and n-Si substrate (blue colors). The current is measured applying a bias from -0.5 V to +0.5 V.

p-Si substrate are indicated in different shades of red and the I/V curves of the nanostructures deposited on n-Si pillar substrates are shown as different shades of blue. The increasing island size is indicated as darkening of the chosen color.

In case of p-doped Si substrate, the I/V curves feature diode with blocking behavior under reverse bias conditions. In the negative bias regime, the graph exhibits weak oscillation behavior, which can be caused by vibrations and subsequent contact problems during the measurement. The I/V curves

of the island/n-Si show only weak asymmetry, when comparing the positive and negative bias regions, which is in agreement with the previous simulation using COMSOL: The depletion width is as large as the island itself and thus, the diode can not block efficiently the current flow in reverse bias conditions (see Fig. 4.42).

For the p-doped case, it is expected that applying a positive bias at the backside contact (p-Si-Al) will increase the depletion width and result in reverse bias conditions, while applying a negative bias reduces the depletion width and leads to forward bias conditions. To confirm the behavior under reverse bias for the p-Si substrate, again COMSOL was used to simulate the scenario of applying bias to both the top (Ge-Al) and bottom contact (Si-Al). The results of the I/V curve are displayed in Fig. 4.44. Different polarities of the

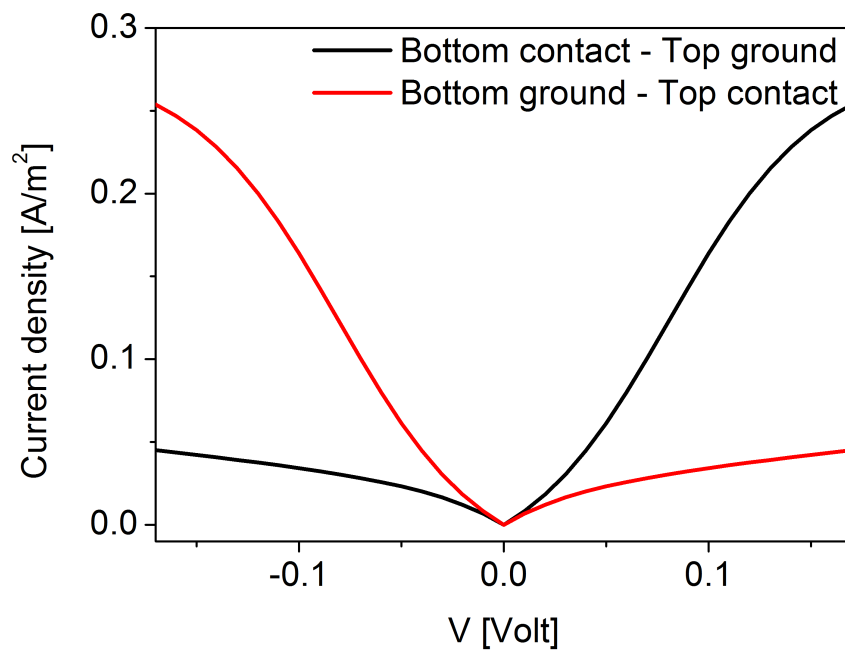


Figure 4.44: Simulated I/V curves of in GeSn/p-doped Si heterojunction. The current density is plotted depending on the applied tension in the range between -0.17 V and +0.17 V for different polarization. Black indicates that the top (GeSn islands) are grounded and the red graph demonstrates the characteristic for a grounded backside contact.

p–n junction were simulated and the resulting current densities depending on the bias in the range between -0.17 V and $+0.17$ V are plotted. When the top side (GeSn nano-islands) is grounded, blocking behavior is observed, while in case the bottom Si–Al side is grounded conducting behavior is detected. These simulations of the polarities of the p–n heterojunction fit to the theoretical predictions for reverse/forward bias conditions and are also in agreement with the experimental results, confirming consistency of our measurement results. To adjust reverse (forward) bias conditions, a bias is applied to the backside (top) contact.

The next step is the illumination of the samples by a glass fiber and the determination of the optical responsivity $R_{opt.}$ according to Eq. 3.45 at 0 V external bias in air at room temperature. When selecting an illumination spot, there are two regions, which can be distinguished. Referring to Fig. 3.13 position 1 is assigned to the region without Al cover, while at position 2 the sample surface is partially covered by a ≈ 100 nm thick Al layer. The reason for choosing these illumination spots will be discussed later.

Fig. 4.45 (a) shows the optical responsivity of all GeSn nano-islands deposited on p-doped Si pillar substrates under illumination at position 2, i.e. with Al partly covering the GeSn nanostructures. All GeSn nano-islands feature an enhanced optical responsivity at about 680 nm independently of the island size. Interestingly, the smallest islands *GeSn120* exhibit the highest $R_{opt.}$ of about 0.1 A/W, which is almost twice the responsivity obtained from *GeSn190* with highest island diameter. At about 1000 nm a second peak can be observed. Here, the responsivity varies strongly with island size. Furthermore, sample *GeSn155* exhibits a third resonance at about 850 nm. Simulation results are shown later in this chapter, which suggest that the additional peaks at > 800 nm are caused by the presence of the Al top layer.

The optical responsivity at position 2 of all GeSn and Ge islands grown on n-Si pillar substrates are illustrated in Fig. 4.45 (b). Both sample *GeSn140* and *Ge160b* show strong intensity fluctuations in the wavelength region between 750 nm and 880 nm, because of the low signal to noise ratio owed to the low sensitivity of the detector. All Ge and GeSn nano-islands show

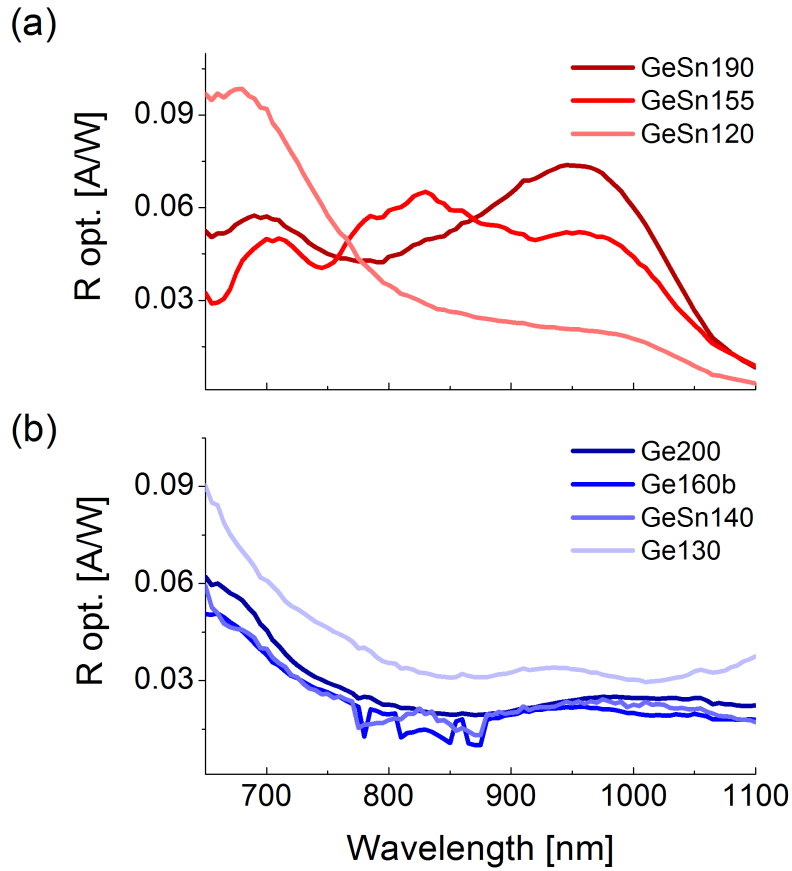


Figure 4.45: Optical responsivity $R_{opt.}$ of Ge and GeSn islands on (a) p-Si substrate (red graphs) and (b) n-Si substrate (blue graphs) at position 2 depending on the wavelength. The increasing island size is indicated as darkening of the color.

an increased optical responsivity at 650 nm, which suggests a signal peak at < 650 nm outside the range of the experimental setup, which is limited to the wavelengths between 650 nm and 2000 nm. Interestingly, the smallest Ge islands, namely *Ge130*, exhibit the largest optical responsivity (up to 0.9 A/W) similar as in case of the nanostructures grown on p-Si substrate. Around 1000 nm a slight increase of the optical responsivity can be observed for all samples. This is not caused by the island size, but can be assigned to the influence of the Al top layer, which will be confirmed later by further simulations. In case of sample *Ge130* this peak is shifted to lower wavelengths to about 950 nm. Note, that both p- and n-doped Si substrates exhibit the

same pitch size of the nano-pillars (230 nm). Hence, an influence of the pillar density on the measurements of the optical responsivity of both sample sets can be excluded. It is interesting to notice that while peak positions for the Ge(Sn) islands on p- and n-doped Si substrates are at comparable wavelengths, the dependence of the peak heights on the islands diameter varies a lot; this will be discussed later on.

Fig. 4.46 (a) depicts a comparison of the measured $R_{opt.}$ of *GeSn120* illuminated at position 1 (without Al nano-antennas) and at position 2 (with Al nano-antennas). The GeSn islands equipped with an Al nano-antenna

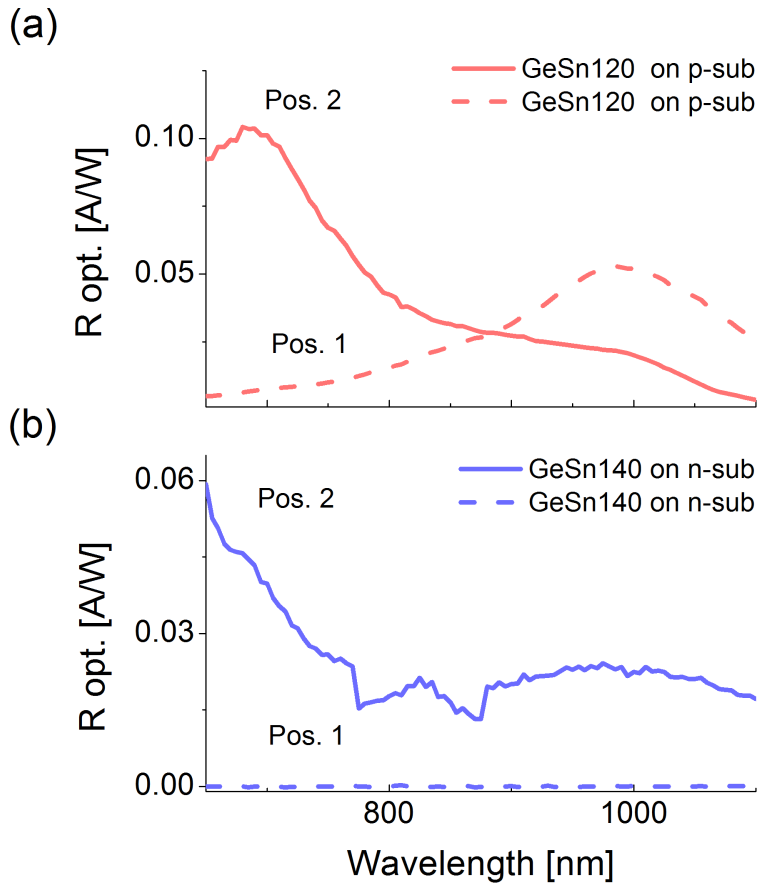


Figure 4.46: Optical responsivity $R_{opt.}$ of (a) GeSn120 on p-Si substrate (red) and (b) GeSn140 on n-Si substrate (blue) at different wavelength. Position 1 (dashed graph) corresponds to region without Al nano-antennas, while at position 2 (solid graph) the GeSn nano-islands are equipped with an Al antenna.

(position 2, solid graph) show a resonance peak at about 680 nm, while in the region without nano-antennas (position 1, dashed graph) an increased optical responsivity can be observed around 1000 nm. If the photocurrent originates exclusively from the Ge(Sn) islands equipped with an Al antenna, a signal of the GeSn nanostructures is only expected under illumination at position 2. The carriers generated in the nano-islands are not expected to contribute to the photocurrent, when illuminating at position 1. Hence, data suggest that the resonance peak at 680 nm at position 2 is attributed to the GeSn nano-islands. The resonance peak at about 1000 nm at position 1 can be assigned to the Si substrate. COMSOL simulations (see Fig.4.42 (a,b)) confirm the existence of an electric field in the p-Si wafer close to the backside contact. Carriers generated in that area of the Si wafer contribute to the photocurrent. The drop in optical responsivity for the wavelength > 1000 nm is a consequence of the bandgap of Si at 1100 nm (1.12 eV), which acts as a cut-off for absorption at higher wavelengths. The drop at lower wavelengths can be explained with an increase in absorption of bulk Si, which prevents the incident light from fully penetrating through the wafer to its backside and hence, no carriers are generated close to backside contact.

The results of the characterization of the optical responsivity of *GeSn140* deposited on highly n-doped Si substrates is shown in Fig. 4.46 (b). At position 1 (dashed graph) no enhanced optical responsivity can be observed in the range between 650 nm and 1100 nm. Therefore, no impact of the Si substrate on the photocurrent was detected. The lack of resonance peak caused by the substrate is in agreement with the simulations using COMSOL as discussed before (see Fig.4.42 (c)): there is a larger electric field within the nano-islands, leading to an increased contribution from carriers generated within the Ge(Sn) islands to the photocurrent compared to the substrate. Furthermore due to the high doping of the Si substrate, an increased free carrier recombination is expected, preventing the incident light from fully penetrating into the Si wafer to the backside. Hence, carrier generation within the Si substrate does not contribute to the photocurrent.

At position 2 (solid graph) the optical responsivity increases at ≤ 650 nm up to 0.06 A/W. Unfortunately, the complete signal was not detected, because

the excitation wavelength is limited to 650 nm. The signal of the optical responsivity shows a sudden drop in intensity at about 780 nm and 880 nm, respectively, which can be interpreted as measurements artifacts: at these wavelengths the detector exhibits the lowest sensitivity and thus, the signal to noise ratio is very low causing the strong drop of the signal. Furthermore, a broad peak at around 1000 nm is detected. Similar to the spectrum of the GeSn nano-islands deposited on p-Si substrate, the enhanced optical responsivity at 1000 nm is not caused by the nano-islands, but by the Al cap layer (discussed later). The reason for the shift of the resonance wavelength at 650 nm in case of the n-doped Si substrate compared to the p-substrate with an enhanced optical responsivity at about 700 nm, requires further investigations. Measurements confirmed however, that using a highly n-doped Si pillar substrate suppresses the influence of the substrate on the photocurrent and hence, the optical responsivity of the GeSn nano-dots can be better characterized.

The dependence of the optical responsivity on the polarization of the incident light was also tested by twisting the fiber and thus, rotating the polarization of the emitted light. Since it is not possible to measure the exact polarization state of the emitted light in the experimental setup, the following characterization allows only a qualitative discussion about the influence of the polarization on the photocurrent. Fig. 4.47 (a) illustrates the measured $R_{opt.}$ at various polarizations of the light. The fiber was rotated to a point, where either the responsivity attained its minimum (GeSn120 Pol min) or its maximum (GeSn120 Pol max). The optical responsivity is significantly influenced by changing the polarization of the light. In fact, it is possible either to maximize $R_{opt.}$ to about 0.10 A/W or to suppress the signal at 680 nm. A previous study by Senanayake et al. [85] investigating the plasmonic enhancement of the coupling of the incoming light, showed that the strong polarization dependence is attributed to the specific properties of the LSPs excited in the nano-antennas. Unfortunately, in this thesis it is only possible to make qualitative statements about the presence or lack of the polarization dependence of the optical responsivity.

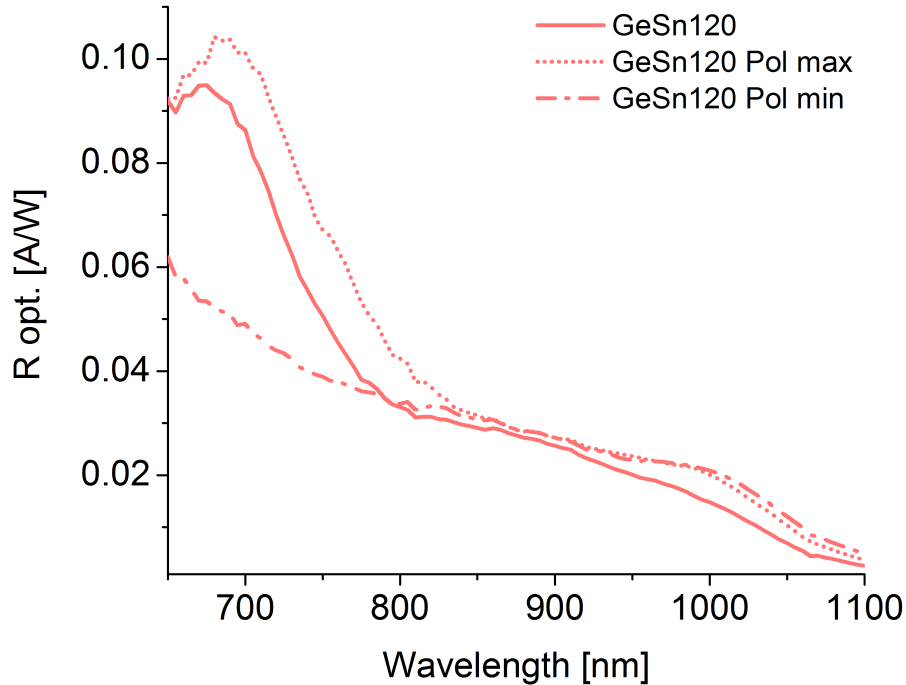


Figure 4.47: Wavelength-dependent optical responsivity $R_{opt.}$ of GeSn120 on p-Si substrate for different polarization at position 2. The resonance peak at 680 nm is maximized (dashed-point graph) or minimized (dotted graph) by changing the polarization of the light by twisting the glass fiber.

Furthermore, the impact of different evaporation angles of Al on the optical responsivity was investigated in case of sample *Ge160* shown in Fig. 4.40. The measured optical responsivity of *Ge160a* and *Ge160b* are compared in Fig. 4.48. In case of *Ge160b* (solid blue graph) Al was evaporated under an angle of 30° with respect to the sample surface, similar to the other samples discussed before. *Ge160a* (dashed blue graph) was covered with Al under an evaporation angle of 45° , resulting larger voids (55 nm) compared to *Ge160b* (21 nm). The trend of the optical responsivity $R_{opt.}$ in both cases is similar: at 650 nm the optical responsivity increases and around 1000 nm a small signal is visible. $R_{opt.}$ of *Ge160b* is with about 0.050 A/W higher compared to $R_{opt.}$ of *Ge160a* exhibiting an optical responsivity of about 0.025 A/W. Hence, the smaller void of 21 nm (*Ge160b*) causes a stronger resonance at

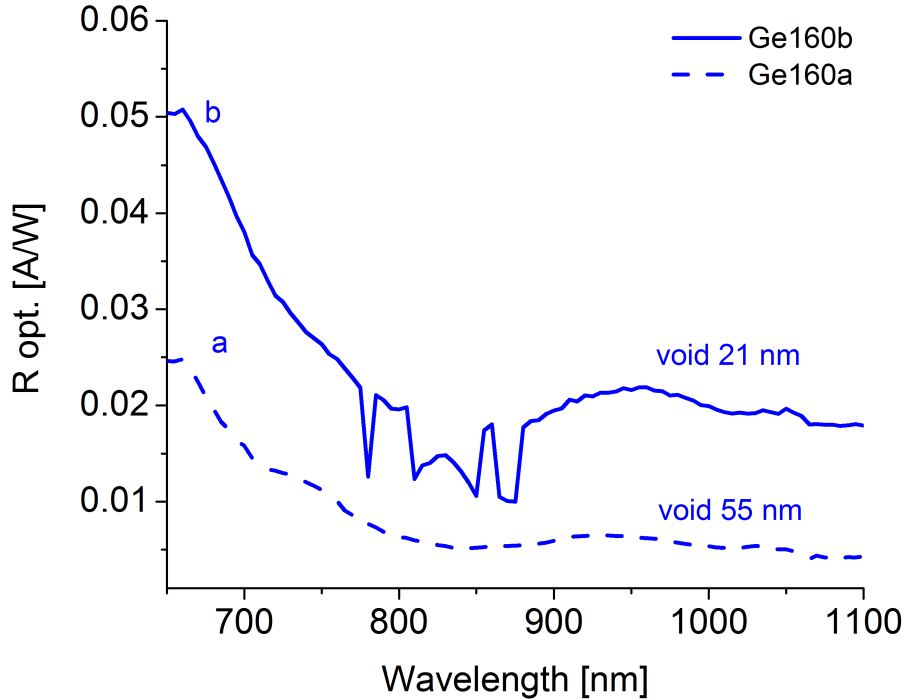


Figure 4.48: Wavelength-dependent optical responsivity $R_{opt.}$ of Ge islands on n-Si substrate under illumination at at position 2. Al was evaporated under an angle of 30° (Ge160b) and 45° (Ge160a), respectively, in respect to the surface normal. Ge160b exhibit about ≈ 21 nm large voids (solid blue graph), while Ge160a features about 55 nm large voids (dashed blue graph).

650 nm compared to a larger void of 55 nm (*Ge160a*). However, the increase of the optical responsivity is not in the range of several orders of magnitude, indicating a weak dependence of the optical responsivity on the void size.

The experimental results demonstrated that it is possible to couple light with a wavelength λ into Ge(Sn) nanostructures, which are much smaller than $\lambda/2$. The measured optical responsivity $R_{opt.}$ of the smallest islands with a diameter of 120 nm and 130 nm, respectively, is with about 0.1 A/W relatively high. As comparison with photodetectors based on *bulk* Ge equipped with disc-shaped Al nano-antennas give a maximum optical responsivity of about 0.2 A/W [105].

Our responsivity spectra show peaks at wavelengths ≈ 650 nm and ≈ 1000 nm. While the qualitative dependence of the responsivity spectra on island diameter is comparable, the dependence of the peak height on island diameter is noticeably different, depending on whether the islands are deposited on p- or n-doped Si substrates. Furthermore, the contribution to the photocurrent originating from the Si substrate cannot be neglected in the case of the p-doped substrate but can be suppressed by switching to a n-doped substrate.

However, a comprehensive study and the support of theoretical simulations are necessary to understand the principle behind the field enhancement. Fig. 4.49 illustrates the components, which can influence the wavelength dependence of the measured optical responsivity. Resonance peaks can orig-

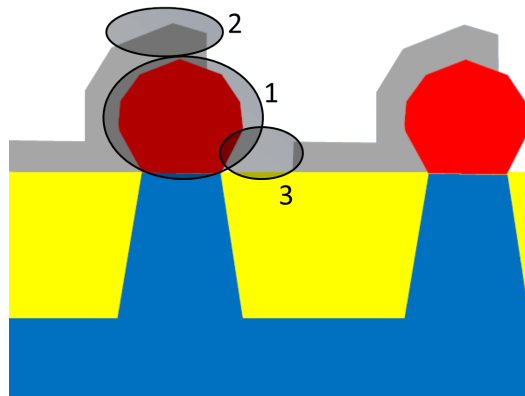


Figure 4.49: Cross section sketch of nanostructures (red) on Si pillar substrate (blue) in an SiO_2 matrix (yellow), which are partly covered with Al (gray). The three parameters which have an impact on the resonance wavelength are labeled by black ellipses: (1) leaky modes of islands, (2) local surface plasmons generated in the Al cap layer and (3) the local surface plasmons excited in the voids in the Al layer.

inate from

- (1) LMRs resonances of the islands
- (2) LSPs resonances generated with in the Al cap
- (3) LSPs resonances originated from voids in the Al adjacent to the islands.

Note that we cannot expect effects from the regular arrangement of the Ge(Sn) dots in a lattice to contribute, since the lattice ordering is imperfect, due to the variation in island size and shape.

(1) LMRs resonances of the islands have been systematically investigated varying the island diameter. No dependence of the optical responsivity on the dots size was observed, which has to be explained by further simulations. (2) LSPs excited in the Al cap will have an impact on the absorption behavior of the nano-islands. Different Al cap layer thicknesses have not been taken into account until now, but will be discussed in the following section based on further calculations. (3) Considering LSPs generated in the voids next to the Ge(Sn), only a slight increase of the optical responsivity was observed changing the size of the voids, which has to be explained.

Simulation of absorption spectra

The theoretical results for the absorption spectra have been obtained by the group of Prof. Bernd Witzigmann from the university of Kassel. Here, the permittivity of GeSn was included into 3d simulations that predict absorption spectra of the GeSn dots [106]. Finite Element Method (FEM) modeling includes several aspects such as the proper choice of the mesh, the correct selection of material properties and their temperature dependence, modeling of the refractive index and proper evaluation of excitation wavelength. Given these parameters as an input, the result obtained is the spatial distribution of the electro-magnetic field that has been evaluated for different geometries and different excitation wavelengths. Combining the electro-magnetic distribution and the plasmonic frequency spectra obtained by the Drude model, the optical absorption of one GeSn dot has been calculated. In the following section these simulations will be compared with our experimental results for the optical responsivity of the Ge(Sn) dots. More details of the simulation method can be found in [107].

Fig. 4.50 compares the experimental results for the optical responsivity of the nano-islands on p- and n-Si substrates with first simulations by the group of

Prof. Witzigmann. Figs. 4.50 (c) and (d) display the calculated absorption for *one* nano-island. Hence, effects from the arrangement of the islands in

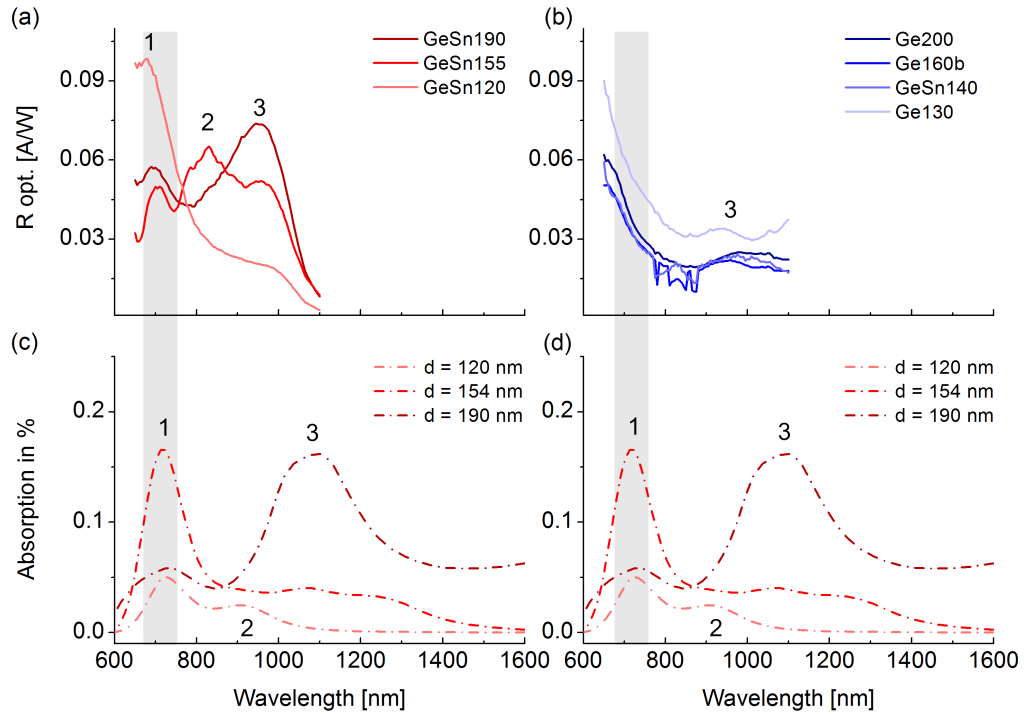


Figure 4.50: Measured optical responsivity of nano-islands grown on (a) p-Si substrate (red) and n-Si substrate (b) (blue), respectively. The darkening of the color indicates increasing island diameter. (c,d) Calculated absorption of GeSn with increasing diameter indicated by darkening red. The Al layer thickness is 100 nm. Characteristic peaks are labeled with numbers from 1 to 3.

an ordered lattice are discounted. However, since the island size and position vary in our samples, lattice effects can be expected to be negligible.

The aim is to investigate the influence of the size of the islands on the light absorption. Fig. 4.50 (a) demonstrates that increasing the diameter of the GeSn nano-islands from 120 nm to 190 nm does not change the wavelength of peak 1 at about 710 nm. Calculations (see Fig. 4.50 (c)) confirm, that the resonance wavelength of the maximum optical responsivity of the GeSn nano-islands remains stable at about 700 nm (peak 1), despite the changing island diameter. The reason for the independence of the resonant wavelength from the island size, is caused by the location of the origin of the excited LSPs.

Further simulations of the distribution of the intensity of the electric field are shown in Fig. 4.51. Simulation results suggest that at this wavelength, a

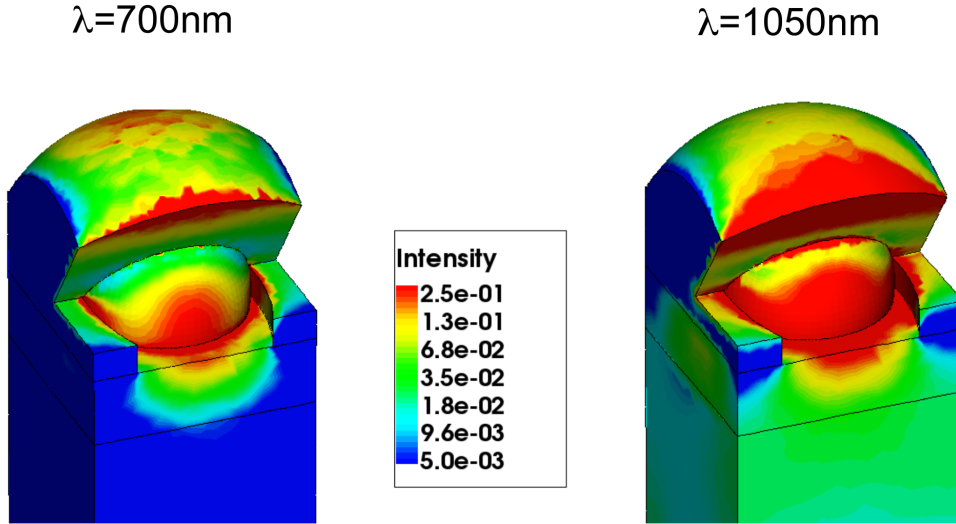


Figure 4.51: Calculated intensity of the electric field in case of GeSn nanostructure with a diameter of 180 nm for the illumination with 700 nm (left) and 1050 nm (right), respectively.

LSPs is generated and located on top of the Al nano-antenna, covering the GeSn island (see Fig. 4.51 (left)). Hence, the resonance wavelength for the excitation of the LSPs on top of the Al shell is not influenced by the island radius. Illuminating at longer wavelengths causes the excitation of LSPs deeper in the Al layer close to the Al-island interface (see Fig. 4.51 (right)). Consequently, the resonance wavelength at 650 nm is not influenced by the void size explaining the missing dependence of the optical responsivity on the void size in Fig. 4.48.

As mentioned before, the resonance wavelength for the islands on n-Si substrates is shifted to smaller wavelength outside the detection limit (< 650 nm) (see Fig. 4.50 (b)) and thus, the experiment results do not show a perfect match with the simulation for the absorption of one nano-dots (see Fig. 4.50 (d)). More investigations are necessary to properly understand this resonance wavelength shift in case of the n-doped substrate.

The simulation results of the polarization dependence of sample *GeSn120*

covered with 100 nm Al are compared with the experimental measurements in Fig. 4.52. These simulations demonstrate, that a change from y- to x-

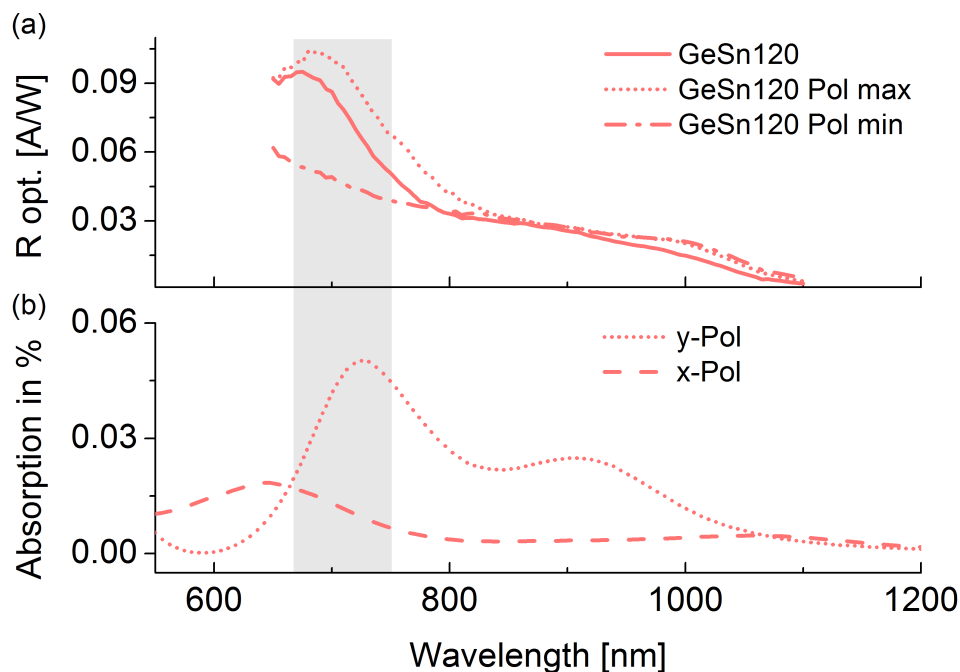


Figure 4.52: (a) Measured optical responsivity $R_{opt.}$ of GeSn120 on p-Si substrate depending on the wavelength for different polarization at position 2. The resonance peak at 680 nm is maximized (dashed-point graph) or minimized (dotted graph) by changing the polarization of the light by twisting the glass fiber. Calculated absorption of GeSn with a diameter of 120 nm covered with a 100 nm thick Al layer for x- (dashed graph) and y-polarization (dotted graph).

polarization causes a reduction of the absorption and a blueshift of the the resonance wavelength below 650 nm. These calculations are in very good agreement with the experimental results obtained for the polarization dependence of *GeSn120* (see Fig. 4.52 (a)), where $R_{opt.}$ is reduced at about 700 nm. Due to the increasing optical responsivity at 650 nm, it can be assumed, that the signal is shifted towards lower wavelengths outside the detection limit, which is confirmed by simulation results shown in Fig. 4.52 (b).

Moreover, additional peaks at at > 800 nm can be observed in both sample sets and are referred to as peak 2 and 3 in Fig. 4.50. To clarify the enhanced optical responsivity at larger wavelengths, further simulations by the

group of Prof. Witzigmann investigate the influence of the Al layer on top of the islands on the light absorption, which are summarized in Fig. 4.53. By varying the Al thickness on top of the GeSn islands, the absorption spec-

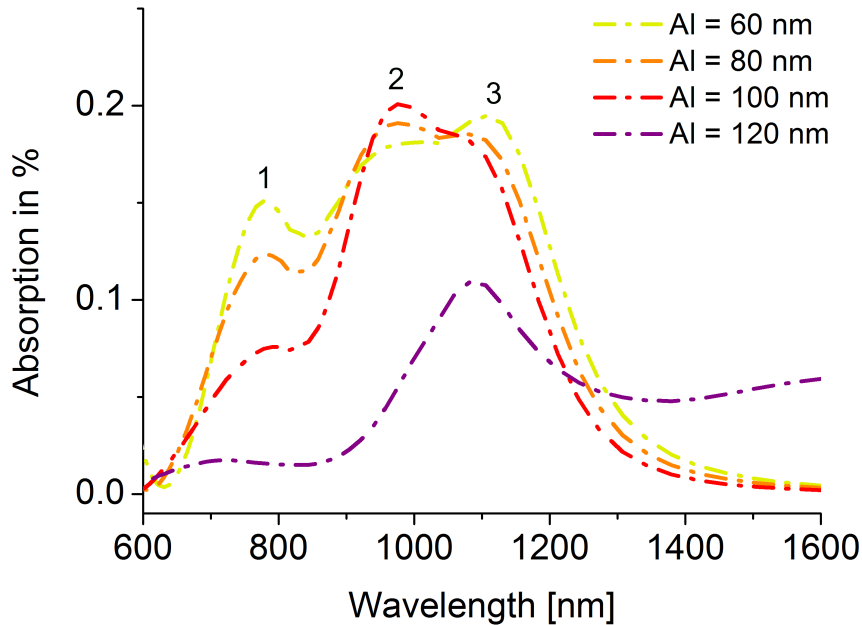


Figure 4.53: Calculated absorption of GeSn with a diameter of 160 nm for different Al thickness. The Al layer thickness is increasing from 60 nm (yellow) to 120 nm (purple). Characteristic peaks are labeled with numbers from 1 to 3.

trum is changed significantly. Peak 1 at about 780 nm is not shifted, but the absorption of the nano-islands decreases, due to the increasing coverage of the Al on top of the GeSn nanostructures. The peak shape as well as peak position at about 1000 nm varies significantly depending on the Al thickness. At Al thicknesses between 60 nm and 100 nm, a double peak at about 975 nm (peak 2) and 1105 nm (peak 3) can be observed with different peak intensities depending on the Al thickness. One single peak at about 1105 nm (peak 3) can be observed when Al is 120 nm thick. Additionally, the absorption spectrum is continuously increasing at > 1300 nm, which is not the case for lower Al thicknesses. These data suggest that the absorption spectrum at wavelength > 800 nm strongly depends on the thickness of the

Al top layer. The calculation of the field distribution in Fig. 4.51 (right) shows that at > 800 nm the plasmons are excited in the Al cap layer at the Al-Ge interface, which can be observed in our study as well (Figs. 4.50 (a,b)). Hence, these plasmons are closer to the islands, causing a larger dependence on the island diameter. Senanyake and co-workers investigated the photoreponse of nano-pillar arrays partly covered with gold [108]. In their case, the enhanced responsivity is caused by both propagating Surface Plasmon Polariton Bloch Waves (SPP-BWs) and LSPs. The SPP-BWs are generated by the periodicity of the self-aligned metal holes. Senanyake and co-workers observed that, the LSPs can be spectrally changed by modification of the antenna geometry such as the gold thickness. In our study, the field enhancement by SPP-BWs is not expected, since the array of the voids is not regularly aligned in shape and geometry across the sample surface. However, a huge influence of the field enhancement on the nature of LSPs is expected, which depends for example on the Al layer thickness.

Finally, the simulation results can be used to motivate the different dependence of responsivity peak height on island size for Ge(Sn) islands deposited on p- and n-doped Si substrates. While the absorption is the same in both cases (as obtained from simulation), the collected photocurrent differs because the efficiency with which carriers generated within the Ge(Sn) can be collected at the contacts depends on the local electric field at the point where the carriers are generated. The electric field distribution within the Ge(Sn) islands, however, is influenced considerably by the Si substrate doping (see Fig. 4.42 (a,c)). As shown in simulations the responsivity peak at ≈ 1000 nm originates from a LSPs resonance mode located at the interface between the Al cap and the Ge(Sn) island surface. This is also the region in which the electric field strength resulting from the metal-semiconductor-metal structure (Fig. 4.42 (a)) is highest for the p-doped substrate, i.e. where the photogenerated carriers are efficiently collected, leading to a strong contribution to the photocurrent. For the n-doped substrate (see Fig. 4.42 (c)), photogenerated carriers are collected throughout the island volume, leading to a relatively lower contribution of those carriers profiting

from additional LSPs resonance field enhancement at the Al-Ge(Sn) interface to the overall photocurrent.

Summary

In summary, it is possible to obtain responsivities up to 0.1 A/W in photodetectors based on Ge(Sn) nanostructures with self-aligned Al nano-antennas, which provide local field, thus boosting the photocurrent. The highest optical responsivity in the range of about 0.1 A/W can be observed for the smallest islands with a diameter of 120 nm and 130 nm, respectively. Although a more comprehensive study and further support of theoretical simulations are necessary to understand the origins of the field enhancement, this study has clearly shown, that (i) the choice of substrate as well as (ii) the specific geometry of the Al nano-antennas are crucial for influencing the resonance wavelength for the plasmonic field enhancement.

(i) By proper doping the influence of the substrate can be suppressed, enabling the photodetection caused by the Ge or GeSn nanostructures.

(ii) By tuning the geometry of the Al, the coupling of the incoming light can be modified.

These first results of the optical optical responsivity of the Ge and GeSn nanostructures are very promising for future photodetectors based on nano-island arrays of group IV semiconductors.

5 | Conclusion and Outlook

In the framework of this thesis, the conditions for the selective growth of GeSn nano-islands on Si(001) nano-pillars have been established. The best compromise between a sufficient degree of selectivity and the incorporation of Sn can be achieved at 600 °C with a deposition rate of 5.4 nm/min and a Sn cell temperature of 1100 °C leading to the incorporation of 1.4 ± 0.5 at.% Sn into the Ge lattice. Varying the growth parameters either the Ge flux or the Sn cell temperature, results neither in higher degree of selectivity nor an increase of the Sn concentration in the nano-dots. Due to the absence of the *substrate compliance* effect caused by the large Si pillar diameter, the GeSn nano-islands are fully plastically relaxed. Dislocations can be found near the island/substrate interface, while the main part of the nanostructures is dislocation-free. Thus, the GeSn nano-crystals exhibit a high crystallinity and negligible Si interdiffusion at $T_s < 750$ °C, using the NHE approach. An improvement of the NHE growth can be the utilization of nano-patterned Si substrates with a reduced Si seed, enabling the effect of *substrate compliance*, leading to the formation of a coherent island/substrate interface. μ -PL measurements confirmed the shrinkage of the direct bandgap energy with increasing Sn concentration, demonstrating the tunability of the bandgap by varying the Sn concentration of the GeSn alloy.

Nevertheless, the *as grown* GeSn islands suffer significant segregation and out-diffusion of Sn atoms, forming β -Sn *droplets* on the low energy {111} nano-facet. Hence, an optimized growth strategy was established to avoid Sn segregation out of the nano-dots and to increase the Sn concentration. The formation of Sn *droplets* was suppressed by a subsequent overgrowth of

the GeSn nanostructures by Ge cap at elevated temperatures $> T_{ec}$. EDX analyses revealed a homogeneous incorporation of Sn up to ≈ 1.4 at.% in the island *core* and a Sn rich GeSn *crust* wetting the dot surface with a Sn concentration of ≈ 7 at.%.

The proposed growth scenario is assumed as follows: During co-evaporation of Ge and Sn, liquid Sn is wetting the GeSn nano-island surface. When cooling down the *as grown* sample, spherical β -Sn *droplets* are formed on the GeSn nano-facets. To avoid the formation of these Sn segregates on top of the islands, the Sn evaporation is blocked after the GeSn growth, while the deposition of Ge continues. The additional Ge atoms from the vapor phase consume the available Sn from the wetting layer forming a Sn rich GeSn *crust*. The assumed growth scenario is similar to liquid-vapor deposition. Since the attractive force between GeSn/Ge is stronger than Sn/Ge a wetting *crust* is formed in case of capping the island, while the formation of Sn islands is favored in the case of the *as grown* samples.

The GeSn *crust* layer enhances the PL spectral intensity of the low Sn content *core*. It can be argued that this outer layer is acting as a surface passivation of the GeSn islands. Interestingly, the Sn rich *crust* is associated with a relative strong PL signal. Unfortunately, state-of-the-art characterization of the Sn rich *crust* were not performed, it is assumed that the GeSn layer on top is not plastically relaxed and thus possesses a very high crystallinity leading to a relative strong radiative emission. Additionally, the PL peak of the *crust* layer show a high thermal stability of the bandgap up to 300 K. The stable bandgap is explained by means of compensation of the temperature driven bandgap shrinkage by a thermally activated transfer of the oscillator strength from the indirect to the direct radiative transition which are almost degenerated at high Sn concentration investigated in this study.

Finally, a proof of concept of a Ge(Sn) based photodetector has been demonstrated. The Ge(Sn) nanostructures were partly covered by Al, coupling the incoming light into the nano-dots by field enhancement, due to the excitation of LSPs. The maximum optical responsivity of 0.1 A/W of the smallest islands with a diameter of 120 nm and 130 nm, respectively, was detected at a wavelength of ≈ 700 nm. Furthermore, it has been shown, that the

specific geometry of the Al nano-antennas as well as the choice of substrate have a significant impact on the resonance wavelength for the plasmonic field enhancement, i.e. by proper doping of the substrate the photocurrent exclusively originates from the NHE crystals. Future studies have to focus on the manipulation of the resonance wavelength, shifting the required wavelength for the photodetection of the Ge(Sn) dots into the telecommunication regime.

In summary, the results achieved in this study demonstrate, that GeSn alloys are a promising material system for the “More than Moore“ trend aiming for GeSn nanostructure based photodetectors for high performance optoelectronic devices. Following aims were accomplished:

- successful selective growth of GeSn at elevated temperatures well exceeding the eutectic temperature of GeSn
- overcoming the growth challenges of GeSn forming high crystal quality GeSn nano-islands
- tuning the bandgap by varying the Sn content
- optimizing the optoelectronic properties of GeSn nano-dots and suppression of Sn segregation out of the islands by formation of a cap and
- demonstrating the ability of the GeSn nanostructures to be used as a photodetector.

However, the targeted detection in the telecommunication regime is not accomplished. The photodetection takes place in the visible/near infrared wavelength. To gain a comprehensive understanding of the interaction of the Al nano-antennas on top of the GeSn nanostructures with the incoming light and to tune the maximum responsivity towards the telecommunication regime, further investigations are necessary. One idea is to change the pitch size of the Si nano-pillars to tune the wavelength of the photodetection of the Ge(Sn) nanostructures.

Scientific visibility

Publication in peer-reviewed journals

- V. Schlykow et al., *Plasmon enhanced Ge(Sn) nano-island photodetectors*, in preparation, (2019).
- V. Schlykow, P. Zaumseil, M. A. Schubert, O. Skibitzki, Y. Yamamoto, W. M. Klesse, Y. Hou, M. Virgilio, M. De Seta, L. Di Gaspare, T. Schroeder and G. Capellini, *Photoluminescence of GeSn nano-heterostructures*, *Nanotechnology* 29, p. 415702 (2018).
- V. Schlykow, W. M. Klesse, G. Niu, N. Taoka, Y. Yamamoto, O. Skibitzki, M. R. Barget, P. Zaumseil, H. von Känel, M. A. Schubert, G. Capellini, and T. Schroeder, *Selective growth of fully relaxed GeSn nano-islands by nanoheteroepitaxy on patterned Si(001)*, *Applied Physics Letters* 109, p. 202102 (2016).
- N. Taoka, G. Capellini, V. Schlykow, M. Montanari, P. Zaumseil, O. Nakatsuka, S. Zaima, and T. Schroeder, *Electrical and optical properties improvement of GeSn layers formed at high temperature under well-controlled Sn migration*, *Materials Science in Semiconductor Processing* 57, p. 48 (2017).
- A. D. Bartolomeo, M. Passacantando, G. Niu, V. Schlykow, G. Lupina, F. Giubileo and T. Schroeder, *Observation of field emission from GeSn nanoparticles epitaxially grown on silicon nanopillar arrays*, *Nanotech-*

nology 27, p. 485707 (2016).

Publication in peer-reviewed proceedings

- V. Schlykow, N. Taoka, M.H. Zoellner, O. Skibitzki, P. Zaumseil, G. Capellini, Y. Yamamoto, T. Schroeder, G. Niu, Proc. International SiGe Technology and Device Meeting (ISTDM 2016), abstr., 92 (2016).
- G. Niu, G. Capellini, G. Lupina, T. Niermann, M. Salvalaglio, A. Marzegalli, M.A. Schubert, P. Zaumseil, H.-M. Krause, O. Skibitzki, V. Schlykow, M. Lehmann, F. Montalenti, Y.-H. Xie, T. Schroeder, Proc. International SiGe Technology and Device Meeting (ISTDM 2016), abstr. 147 (2016).
- N. Taoka, G. Capellini, V. Schlykow, M. Montanari, P. Zaumseil, O. Nakatsuka, S. Zaima, T. Schroeder, Proc. International Symposium on Control of Semiconductor Interfaces (ISCSI 2016) abstr., 96 (2016).

Presentation at conferences

- “Growth and characterization of (Si)GeSn nanostructures“, October 2017, Germany.
- “Selective growth of GeSn nano-islands on patterned Si(001) at high temperature“, March 2017, Germany.
- (24. 26.11.2016): “Selective growth of fully relaxed GeSn nano-islands by nanoheteroepitaxy on patterned Si(001)“, November 2016, Germany.
- “Selective growth of GeSn nano islands with up to 1.4 % Sn on nano-patterned Si(001) wafers“, September 2016, Poland.

- “Selective nano-heteroepitaxial growth of GeSn islands on nano-pillar patterned Si(001)“, June 2016, Japan.
- “Selective formation of nano-GeSn(Si) structures on nano-patterned-Si(001)“, March 2016, Germany.
- “Selective growth of high quality GeSn islands on nano-pillar patterned Si substrates“, November 2015, Germany.

Bibliography

- [1] “Mikroelektronik - trendanalyse bis 2022: Unerwartetes wachstum im letzten jahr.” <https://www.elektroniknet.de/elektronik/halbleiter/unerwartet-starkes-wachstum-im-letzten-jahr-152841.html>. Accessed: 2018-07-02.
- [2] “Internationale daten jugend und medien 2017.” http://www.br-online.de/jugend/izi/deutsch/Internationale_Daten_Jugend_und_Medien.pdf. Accessed: 2017-09-13.
- [3] G. E. Moore, “Cramming more components onto integrated circuits, reprinted from electronics, volume 38, number 8, april 19, 1965, pp.114 ff.,” *IEEE Solid-State Circuits Society Newsletter*, vol. 11, p. 33, 2006.
- [4] “More than moore - white paper.” <http://www.itrs2.net/Links/2010ITRS/IRC-ITRS-MtM-v2%203.pdf>. Accessed: 2014-11-03.
- [5] M. Houssa, *High-k Gate Dielectrics (Series in Materials Science and Engineering)*, vol. 1. CRC-Press, 2003.
- [6] “Itrs roadmap.” <http://www.itrs2.net/>. Accessed: 2017-07-10.
- [7] B. Gil, *III-Nitride Semiconductors and their Modern Devices*, vol. 18. Oxford University Press, 2013.
- [8] H. Morcov, *Handbook of Nitride Semiconductors and Devices*. Wiley-VCH, 2 ed., 2008.

- [9] W. Mehr, J. Dabrowski, J. C. Scheytt, G. Lippert, Y.-H. Xie, M. C. Lemme, M. Ostling, and G. Lupina, "Vertical graphene base transistor," *IEEE Electron Device Letters*, vol. 33, p. 691, 2012.
- [10] R. W. Olesinski and G. J. Abbaschian, "The Ge-Sn (germanium-tin) system," *Journal of Phase Equilibria*, vol. 5, p. 265, 1984.
- [11] R. W. Olesinski and G. J. Abbaschian, "The Si-Sn (silicon-tin) system," *Journal of Phase Equilibria*, vol. 5, p. 273, 1984.
- [12] A. F. Hollemann and E. Wiberg, *Lehrbuch der Anorganischen Chemie*, vol. 102. de Gruyter, 2007.
- [13] Y. Shimura, T. Asano, T. Yamaha, M. Fukuda, W. Takeuchi, O. Nakatsuka, and S. Zaima, "Exafs study of local structure contributing to sn stability in $\text{Si}_y\text{Ge}_{1-y-z}\text{Sn}_z$," *Materials Science in Semiconductor Processing*, vol. 70, p. 133, 2016.
- [14] P. Moontragoon, Z. Ikonić, and P. Harrison, "Band structure calculations of Si-Ge-Sn alloys: achieving direct band gap materials," *Semiconductor Science and Technology*, vol. 22, p. 742, 2007.
- [15] B. Dutt, H. Lin, D. S. Sukhdeo, B. M. Vulovic, S. Gupta, D. Nam, K. C. Saraswat, and J. S. H. Jr., "Theoretical analysis of GeSn alloys as a gain medium for a Si-compatible laser," *IEEE Journal of Selected Topics in Quantum Electronics*, vol. 19, p. 1502706, 2013.
- [16] P. Moontragoon, R. A. Soref, and Z. Ikonić, "The direct and indirect bandgaps of unstrained $\text{Si}_x\text{Ge}_{1-x-y}\text{Sn}_y$ and their photonic device applications," *Journal of Applied Physics*, vol. 112, p. 073106, 2012.
- [17] R. Soref, J. Hendrickson, and J. W. Cleary, "Mid- to long-wavelength infrared plasmonic-photonics using heavily doped n-Ge/Ge and n-GeSn/GeSn heterostructures," *Optics Express*, vol. 20, p. 3814, 2012.

- [18] M. V. Fischetti and S. E. Laux, "Band structure, deformation potentials, and carrier mobility in strained Si, Ge, and SiGe alloys," *Journal of Applied Physics*, vol. 80, p. 2234, 1996.
- [19] S. Wirths, D. Stange, M.-A. Pampillón, A. T. Tiedemann, G. Mussler, A. Fox, U. Breuer, B. Baert, E. San Andrés, N. D. Nguyen, J.-M. Hartmann, Z. Ikonic, S. Mantl, and D. Buca, "High-k gate stacks on low bandgap tensile strained Ge and GeSn alloys for field-effect transistors," *ACS Applied Materials & Interfaces*, vol. 7, p. 62, 2015.
- [20] J. D. Sau and M. L. Cohen, "Possibility of increased mobility in Ge-Sn alloy system," *Phys. Rev. B*, vol. 75, p. 045208, 2007.
- [21] N. von den Driesch, *Epitaxy of group IV Si-Ge-Sn*. PhD thesis, RWTH Aachen university, 2018.
- [22] K. L. Low, Y. Yang, G. Han, W. Fan, and Y.-C. Yeo, "Electronic band structure and effective mass parameters of $\text{Ge}_{1-x}\text{Sn}_x$ alloys," *Journal of Applied Physics*, vol. 112, p. 103715, 2012.
- [23] G. Han, S. Su, C. Zhan, Q. Zhou, Y. Yang, L. Wang, P. Guo, W. Wei, C. P. Wong, Z. X. Shen, B. Cheng, and Y. C. Yeo, "High-mobility germanium-tin (GeSn) p-channel mosfets featuring metallic source/drain and sub-370 °C process modules," in *2011 International Electron Devices Meeting*, p. 16.7.1, 2011.
- [24] S. Gupta, Y. C. Huang, Y. Kim, E. Sanchez, and K. C. Saraswat, "Hole mobility enhancement in compressively strained $\text{Ge}_{0.93}\text{Sn}_{0.07}$ p-mosfets," *IEEE Electron Device Letters*, vol. 34, p. 831, 2013.
- [25] S. Gupta, V. Moroz, L. Smith, Q. Lu, and K. C. Saraswat, "7-nm finfet cmos design enabled by stress engineering using Si, Ge, and Sn," *IEEE Transactions on Electron Devices*, vol. 61, p. 1222, 2014.
- [26] "Si photonics." <http://losnuevosguerreros.org/mod/glossary/view.php?id=1&mode=letter&hook=S&sortkey=&sortorder=&fullsearch=0&page=-1>. Accessed: 2015-03-18.

- [27] S. Wirths, R. Geiger, N. von den Driesch, G. Mussler, T. Stoica, S. Mantl, Z. Ikonic, M. Luysberg, S. Chiussi, J. M. Hartmann, H. Sigg, J. Faist, D. Buca, and D. Grützmacher, “Lasing in direct-bandgap GeSn alloy grown on Si,” *Nature Photonics*, vol. 9, p. 88, 2015.
- [28] G. Niu, G. Capellini, G. Lupina, T. Niermann, M. Salvalaglio, A. Marzegalli, M. A. Schubert, P. Zaumseil, H.-M. Krause, O. Skibitzki, M. Lehmann, F. Montalenti, Y.-H. Xie, and T. Schroeder, “Photodetection in hybrid single-layer graphene/fully coherent germanium island nanostructures selectively grown on silicon nanotip patterns,” *ACS Applied Materials & Interfaces*, vol. 8, p. 2017, 2016.
- [29] V. D’Costa, Y. Fang, J. Mathews, R. Roucka, J. Tolle, J. Menéndez, and J. Kouvetakis, “Sn-alloying as a means of increasing the optical absorption of Ge at the c- and l-telecommunication bands,” *Semiconductor Science and Technology*, vol. 24, p. 115006, 2009.
- [30] S. Wirths, D. Buca, and S. Mantl, “Si–Ge–Sn alloys: From growth to applications,” *Progress in Crystal Growth and Characterization of Materials*, vol. 62, p. 1, 2016.
- [31] S. Zaima, O. Nakatsuka, N. Taoka, M. Kurosawa, W. Takeuchi, and M. Sakashita, “Growth and applications of GeSn-related group-iv semiconductor materials,” *Science and Technology of Advanced Materials*, vol. 16, p. 043502, 2015.
- [32] E. Kasper, “Group iv heteroepitaxy on silicon for photonics,” *Journal of Materials Research*, vol. 31, p. 3639, 2016.
- [33] I. V. Markov, *Crystal growth for beginners: fundamentals of nucleation, crystal growth and epitaxy*. World scientific publishing Co. Pte. Ltd., 1995.
- [34] J. E. Prieto and I. Markov, “Thermodynamic driving force of formation of coherent three-dimensional islands in stranski-krastanov growth,” *Phys. Rev. B*, vol. 66, p. 073408, 2002.

- [35] P. Lyman, S. Thevuthasan, and L. Seiberling, "Low temperature pseudomorphic growth of Ge on Si (100)-(2×1)," *Journal of crystal growth*, vol. 113, p. 45, 1991.
- [36] J. Matthews and A. Blakeslee, "Defects in epitaxial multilayers: I. misfit dislocations," *Journal of Crystal Growth*, vol. 27, p. 118, 1974.
- [37] D. B. Holt and B. G. Yacobi, *Extended defects in semiconductors: electronic properties, device effects and structures*. Cambridge University Press, 2007.
- [38] J. Hornstra, "Dislocations in the diamond lattice," *Journal of Physics and Chemistry of Solids*, vol. 5, p. 129, 1958.
- [39] D. Zubia and S. Hersee, "Nanoheteroepitaxy: The application of nanostructuring and substrate compliance to the heteroepitaxy of mismatched semiconductor materials," *Journal of Applied Physics*, vol. 85, p. 6492, 1999.
- [40] D. B. Holt and B. G. Yacobi, *Extended Defects in Semiconductors*. Cambridge University Press, 2007.
- [41] L. Jiang, C. Xu, J. D. Gallagher, R. Favaro, T. Aoki, J. Menéndez, and J. Kouvetakis, "Development of light emitting group iv ternary alloys on si platforms for long wavelength optoelectronic applications," *Chemistry of Materials*, vol. 26, p. 2522, 2014.
- [42] T. Asano, N. Taoka, O. Nakatsuka, and S. Zaima, "Formation of high-quality Ge_{1-x}Sn_x layer on Ge(110) substrate with strain-induced confinement of stacking faults at Ge_{1-x}Sn_x/Ge interfaces," *Applied Physics Express*, vol. 7, p. 061301, 2014.
- [43] S. Luryi and E. Suhir, "New approach to the high quality epitaxial growth of lattice-mismatched materials," *Applied Physics Letters*, vol. 49, p. 140, 1986.

- [44] “Heteroepitaxial growth of Ge on compliant strained nano-structured Si lines and dots on (001) silicon on insulator substrate,” *Thin Solid Films*, vol. 557, p. 50, 2014.
- [45] C. Georgiou, T. Leontiou, and P. C. Kelires, “Shaping the composition profiles in heteroepitaxial quantum dots: Interplay of thermodynamic and kinetic effects,” *AIP Advances*, vol. 4, p. 077135, 2014.
- [46] J. Bauer, Y. Yamamoto, P. Zaumseil, O. Fursenko, K. Schulz, G. Kozłowski, M. Schubert, T. Schroeder, and B. Tillack, “Nanostructured silicon for ge nanoheteroepitaxy,” *Microelectronic Engineering*, vol. 97, p. 169, 2012.
- [47] P. Zaumseil, Y. Yamamoto, J. Bauer, M. A. Schubert, J. Matejova, G. Kozłowski, T. Schroeder, and B. Tillack, “Preparation and characterization of Ge epitaxially grown on nano-structured periodic Si pillars and bars on Si(001) substrate,” *Thin Solid Films*, vol. 520, p. 3240, 2012.
- [48] P. Zaumseil, “High-resolution characterization of the forbidden Si 200 and Si 222 reflections,” *Journal of Applied Crystallography*, vol. 48, p. 528, 2015.
- [49] P. Zaumseil, Y. Yamamoto, A. Bauer, M. A. Schubert, and T. Schroeder, “X-ray characterization of Ge epitaxially grown on nanostructured Si(001) wafers,” *Journal of Applied Physics*, vol. 109, p. 023511, 2011.
- [50] J. Venables, G. Spiller, and M. Hanbucken, “Nucleation and growth of thin films,” *Reports on Progress in Physics*, vol. 47, p. 399, 1984.
- [51] F. Cheynis, F. Leroy, T. Passanante, and P. Müller, “Agglomeration dynamics of germanium islands on a silicon oxide substrate: A grazing incidence small-angle x-ray scattering study,” *Applied Physics Letters*, vol. 102, p. 161603, 2013.

- [52] D. Leonhardt and S. M. Han, “Energetics of Ge nucleation on SiO₂ and implications for selective epitaxial growth,” *Surface Science*, vol. 603, p. 2624, 2009.
- [53] Q. Li, J. L. Krauss, S. Hersee, and S. M. Han, “Probing interactions of Ge with chemical and thermal SiO₂ to understand selective growth of Ge on Si during molecular beam epitaxy,” *The Journal of Physical Chemistry C*, vol. 111, p. 779, 2007.
- [54] G. Niu, G. Capellini, M. A. Schubert, T. Niermann, P. Zaumseil, J. Katzer, H.-M. Krause, O. Skibitzki, M. Lehmann, Y.-H. Xie, H. von Känel, and T. Schroeder, “Dislocation-free Ge nano-crystals via pattern independent selective Ge heteroepitaxy on Si nano-tip wafers,” *Scientific reports*, vol. 6, p. 22709, 2016.
- [55] C. Edelmann, *Vakuumphysik*. Spektrum Akademischer Verlag, 1988.
- [56] D. Zubia and S. Hersee, “Nanoheteroepitaxy: The application of nanostructuring and substrate compliance to the heteroepitaxy of mismatched semiconductor materials,” *Journal of applied physics*, vol. 85, p. 6492, 1999.
- [57] V. K. Yang, M. Groenert, C. W. Leitz, A. J. Pitera, M. T. Currie, and E. A. Fitzgerald, “Crack formation in GaAs heteroepitaxial films on Si and SiGe virtual substrates,” *Journal of Applied Physics*, vol. 93, p. 3859, 2003.
- [58] D. R. Lide, *CRC Handbook of Chemistry and Physics*. CRC Press, 2003.
- [59] M. Friesel, U. Södervall, and W. Gust, “Diffusion of tin in germanium studied by secondary ion mass spectrometry,” *Journal of Applied Physics*, vol. 78, p. 5351, 1995.
- [60] É. V. Dobrokhotov, “Diffusion in dislocation germanium and the model of a liquid dislocation core,” *Physics of the Solid State*, vol. 47, p. 2257, 2005.

- [61] H. Groiss, M. Glaser, M. Schatzl, M. Brehm, D. Gerthsen, D. Roth, P. Bauer, and F. Schäffler, “Free-running Sn precipitates: an efficient phase separation mechanism for metastable GeSn epilayers,” *Scientific Reports*, vol. 7, 2017.
- [62] J. Xie, A. V. Chizmeshya, J. Tolle, V. R. D’Costa, J. Menendez, and J. Kouvetakis, “Synthesis, stability range, and fundamental properties of Si-Ge-Sn semiconductors grown directly on Si (100) and Ge (100) platforms,” *Chemistry of Materials*, vol. 22, p. 3779, 2010.
- [63] N. Taoka, G. Capellini, N. von den Driesch, D. Buca, P. Zaumseil, M. A. Schubert, W. M. Klesse, M. Montanari, and T. Schroeder, “Sn migration control at high temperature due to high deposition speed for forming high-quality GeSn layer,” *Applied Physics Express*, vol. 9, p. 031201, 2016.
- [64] O. Skibitzki, I. Prieto, R. Kozak, G. Capellini, P. Peter Zaumseil, Y. Arroyo Rojas Dasilva, M. D. Rossell, R. Erni, H. von Känel, and T. Schroeder, “Structural and optical characterization of GaAs nanocrystals selectively grown on Si nano-tips by MOVPE,” *Nanotechnology*, vol. 28, p. 135301, 2017.
- [65] B. Voigtländer, *Scanning Probe Microscopy: Atomic Force Microscopy and Scanning Tunneling Microscopy*. Springer Berlin Heidelberg, 2015.
- [66] “Bruker afm probes.” <https://www.brukerafmprobes.com/p-3398-tesp-ss.aspx>. Accessed: 2018-06-10.
- [67] B. E. Warren, *X-ray diffraction*. Dover Publications, 1990.
- [68] B. D. Cullity, *Elements of X-Ray Diffraction*. Addison-Wesley Publishing Company, 1967.
- [69] S. Kobayashi, “X-ray thin-film measurement techniques,” *The Rigaku Journal*, vol. 26, p. 3, 2010.

- [70] M. Bauer, J. Taraci, J. Tolle, A. V. G. Chizmeshya, S. Zollner, D. J. Smith, J. Menendez, C. Hu, and J. Kouvetakis, "Ge-Sn semiconductors for band-gap and lattice engineering," *Applied Physics Letters*, vol. 81, p. 2992, 2002.
- [71] C. Xu, C. L. Senaratne, R. J. Culbertson, J. Kouvetakis, and J. Menéndez, "Deviations from Vegard's law in semiconductor thin films measured with x-ray diffraction and Rutherford backscattering: The $\text{Ge}_{1-y}\text{Sn}_y$ and $\text{Ge}_{1-x}\text{Si}_x$ cases," *Journal of Applied Physics*, vol. 122, p. 125702, 2017.
- [72] J. P. Dismukes, L. Ekstrom, and R. J. Paff, "Lattice parameter and density in Germanium-Silicon alloys," *The Journal of Physical Chemistry*, vol. 68, p. 3021, 1964.
- [73] D. B. Williams and C. B. Carter, *Transmission Electron Microscopy: A Text book for Materials Science*. Springer, 2009.
- [74] D. A. Neamen, *Semiconductor Physics And Devices*. McGraw-Hill, 2011.
- [75] L. Ding, A. E.-J. Lim, J. T.-Y. Liow, M. Yu, and G.-Q. Lo, "Dependences of photoluminescence from p-implanted epitaxial Ge," *Optics express*, vol. 20, p. 8228, 2012.
- [76] S. M. Sze and K. K. Ng, *Physics of Semiconductor Devices*. Wiley, 2006.
- [77] H. Bebb and E. Williams, *Semiconductor and Semimetals: Photoluminescence I*. Elsevier, 1972.
- [78] R. K. Willardson and A. C. Beer, *Semiconductors and semimetals*, vol. 9. Academic press, 1972.
- [79] Y. Varshni, "Temperature dependence of the energy gap in semiconductors," *Physica*, vol. 34, p. 149, 1967.

- [80] “Filmetrics.” <https://www.filmetrics.com/reflectance-calculator?wmin=500&wmax=1100&wstep=1&angle=0&pol=s&units=nm&mmat=Air&smat=Ge&sptype=a>. Accessed: 2018-12-10.
- [81] C. Schulte-Braucks, E. Hofmann, S. Glass, N. von den Driesch, G. Musler, U. Breuer, J.-M. Hartmann, P. Zaumseil, T. Schröder, Q.-T. Zhao, S. Mantl, and D. Buca, “Schottky barrier tuning via dopant segregation in NiGeSn-GeSn contacts,” *Journal of Applied Physics*, vol. 121, p. 205705, 2017.
- [82] K. Hoffmann, *Systemintegration: vom Transistor zur großintegrierten Schaltung*. Walter de Gruyter, 2012.
- [83] Y. Yu and L. Cao, “Coupled leaky mode theory for light absorption in 2d, 1d, and 0d semiconductor nanostructures,” *Optics Express*, vol. 20, p. 13847, 2012.
- [84] L. Cao, *optical Resonances of Semiconductor Nanowires*. PhD thesis, Stanford university, 2010.
- [85] P. Senanayake, C.-H. Hung, J. Shapiro, A. Lin, B. Liang, B. S. Williams, and D. L. Huffaker, “Surface plasmon-enhanced nanopillar photodetectors,” *Nano Letters*, vol. 11, p. 5279, 2011.
- [86] V. Schlykow, W. Klesse, G. Niu, N. Taoka, Y. Yamamoto, O. Skibitzki, M. Barget, P. Zaumseil, H. von Känel, M. Schubert, *et al.*, “Selective growth of fully relaxed GeSn nano-islands by nanoheteroepitaxy on patterned Si(001),” *Applied Physics Letters*, vol. 109, p. 202102, 2016.
- [87] P. Chen, M. Colaianni, J. Yates, and M. Arbab, “Thermal properties of the Sn/SiO₂ interface as studied by surface spectroscopies,”
- [88] A. A. Stekolnikov and F. Bechstedt, “Shape of free and constrained group-iv crystallites: Influence of surface energies,” *Physical Review B*, vol. 72, p. 125326, 2005.

- [89] N. G. Hörmann, A. Gross, and P. Kaghazchi, “Semiconductor–metal transition induced by nanoscale stabilization,” *Physical Chemistry Chemical Physics*, vol. 17, p. 5569, 2015.
- [90] M. R. Barget, M. Virgilio, G. Capellini, Y. Yamamoto, and T. Schroeder, “The impact of donors on recombination mechanisms in heavily doped Ge/Si layers,” *Journal of Applied Physics*, vol. 121, p. 245701, 2017.
- [91] D. Stange, N. von den Driesch, T. Zabel, F. Armand-Pilon, D. Rainko, B. Marzban, P. Zaumseil, J.-M. Hartmann, Z. Ikonic, G. Capellini, S. Mantl, H. Sigg, J. Witzens, D. GrÄijtmacher, and D. Buca, “GeSn/SiGeSn heterostructure and multi quantum well lasers,” *ACS Photonics*, vol. 5, p. 4628, 2018.
- [92] W. Wang, L. Li, Q. Zhou, J. Pan, Z. Zhang, E. S. Tok, and Y.-C. Yeo, “Tin surface segregation, desorption, and island formation during post-growth annealing of strained epitaxial Ge_{1-x}Sn_x layer on Ge(001) substrate,” *Applied Surface Science*, vol. 321, p. 240, 2014.
- [93] V. Schlykow, P. Zaumseil, M. A. Schubert, O. Skibitzki, Y. Yamamoto, W. M. Klesse, Y. Hou, M. Virgilio, M. D. Seta, L. D. Gaspare, T. Schroeder, and G. Capellini, “Photoluminescence from GeSn nano-heterostructures,” *Nanotechnology*, vol. 29, p. 415702, 2018.
- [94] X. Lin, Z. Liliental-Weber, J. Washburn, E. Weber, A. Sasaki, A. Wakahara, and T. Hasegawa, “Sn submonolayer-mediated Ge heteroepitaxy on Si (001),” *Physical Review B*, vol. 52, p. 16581, 1995.
- [95] G. Grzybowski, R. Roucka, J. Mathews, L. Jiang, R. T. Beeler, J. Kouvetakis, and J. Menéndez, “Direct versus indirect optical recombination in Ge films grown on Si substrates,” *Phys. Rev. B*, vol. 84, p. 205307, 2011.
- [96] J. Weber and M. I. Alonso, “Near-band-gap photoluminescence of Si-Ge alloys,” *Phys. Rev. B*, vol. 40, p. 5683, 1989.

- [97] Y. Zhou, W. Dou, W. Du, T. Pham, S. A. Ghetmiri, S. Al-Kabi, A. Mosleh, M. Alher, J. Margetis, J. Tolle, G. Sun, R. Soref, B. Li, M. Mortazavi, H. Naseem, and S.-Q. Yu, "Systematic study of GeSn heterostructure-based light-emitting diodes towards mid-infrared applications," *Journal of Applied Physics*, vol. 120, p. 023102, 2016.
- [98] S. A. Ghetmiri, W. Du, B. R. Conley, A. Mosleh, A. Nazzal, G. Sun, R. A. Soref, J. Margetis, J. Tolle, H. A. Naseem, and S.-Q. Yu, "Shortwave-infrared photoluminescence from $\text{Ge}_{1-x}\text{Sn}_x$ thin films on silicon," *Journal of Vacuum Science & Technology B*, vol. 32, p. 060601, 2014.
- [99] T. Wendav, I. A. Fischer, M. Virgilio, G. Capellini, F. Oliveira, M. F. Cerqueira, A. Benedetti, S. Chiussi, P. Zaumseil, B. Schwartz, K. Busch, and J. Schulze, "Photoluminescence from ultrathin Ge-rich multiple quantum wells observed up to room temperature: Experiments and modeling," *Phys. Rev. B*, vol. 94, p. 245304, 2016.
- [100] A. Yu and C. Mead, "Characteristics of aluminum-silicon schottky barrier diode," *Solid-State Electronics*, vol. 13, p. 97, 1970.
- [101] R. Lieten, V. Afanas'ev, N. Thoan, S. Degroote, W. Walukiewicz, and G. Borghs, "Mechanisms of schottky barrier control on n-type germanium using Ge_3Sn_4 interlayers," *Journal of The Electrochemical Society*, vol. 158, p. H358, 2011.
- [102] D. R. Gajula, P. Baine, M. Modreanu, P. Hurley, B. Armstrong, and D. McNeill, "Fermi level de-pinning of aluminium contacts to n-type germanium using thin atomic layer deposited layers," *Applied Physics Letters*, vol. 104, p. 012102, 2014.
- [103] T. Nishimura, K. Kita, and A. Toriumi, "Evidence for strong fermi-level pinning due to metal-induced gap states at metal/germanium interface," *Applied Physics Letters*, vol. 91, p. 123123, 2007.

- [104] A. Dimoulas, P. Tsipas, A. Sotiropoulos, and E. K. Evangelou, “Fermi-level pinning and charge neutrality level in germanium,” *Applied Physics Letters*, vol. 89, p. 252110, 2006.
- [105] I. A. Fischer, L. Augel, T. Kropp, S. Jitpakdeebodin, N. Franz, F. Oliveira, E. Rolseth, T. Maß, T. Taubner, and J. Schulze, “Ge-on-si pin-photodetectors with al nanoantennas: The effect of nanoantenna size on light scattering into waveguide modes,” *Applied Physics Letters*, vol. 108, p. 071108, 2016.
- [106] V. R. D’Costa, W. Wang, and Y.-C. Yeo, “Near-bandgap optical properties of pseudomorphic gesn alloys grown by molecular beam epitaxy,” *Journal of Applied Physics*, vol. 120, p. 063104, 2016.
- [107] M. S. Mocigemba, “Optical responsivity of $\text{Ge}_{1-x}\text{Sn}_x$ plasmonic photodetectors,” bachelor’s thesis, University Kassel, 2018.
- [108] P. Senanayake, C.-H. Hung, J. Shapiro, A. Scofield, A. Lin, B. S. Williams, and D. L. Huffaker, “3d nanopillar optical antenna photodetectors,” *Opt. Express*, vol. 20, p. 25489, 2012.

